Karlsruhe Institute of Technology

Topological phases in systems with coexisting density waves and superconductivity

Topologische Phasen in Systemen mit koexistierenden Dichtewellen und Supraleitung

Diploma Thesis by

Daniel Mendler

At the Department of Physics
Institut für Theoretische Festkörperphysik

Reviewer:	Prof. Dr. Gerd Schön
Second reviewer:	Prof. Dr. Alexander Shnirman
Advisor:	Dr. Panagiotis Kotetes

Duration: 01 March 2012 – 28 March 2013

Ich versichere wahrheitsgemäß, die Arbeit selbstständig angefertigt, alle benutzten Hilfsmittel vollständig und genau angegeben und alles kenntlich gemacht zu haben, was aus Arbeiten anderer unverändert oder mit Abänderungen entnommen wurde.

Karlsruhe, den 28.03.2013

.....

Daniel Mendler

Deutsche Zusammenfassung

Diese Diplomarbeit beschäftigt sich mit topologischen Phasen in Systemen mit koexistierenden Dichtewellen und Supraleitung. Die Existenz von verschiedenen Phasen von Materie und die entsprechenden Phasenübergänge spielen eine fundamentale Rolle in der Physik. Die Phasen fest, flüssig und gasförmig sind allgemein bekannt. Bei genauerer Betrachtung fällt jedoch auf, dass in der Natur eine reichhaltige Vielfalt an Phasen in unterschiedlichsten Systemen auftritt. In der Theorie der kondensierten Materie wären zum Beispiel die (Anti-)Ferromagnetische Phase, Dichtewellen und Supraleitung zu nennen. Die Beschreibung von Phasenübergängen geht immer mit der spontanen Symmetriebrechung von kontinuierlichen Symmetrien einher. Beim Ferromagnetismus ist es die Rotationssymmetrie des Systems, die gebrochen wird, bei der Supraleitung die U(1) Eichsymmetrie. Abhängig von den phänomenologischen Eigenschaften des zu beschreibenden Systems definiert man Ordnungsparameter, die den Phasen des Systems entsprechen. Ausgehend von einem mikroskopischen Modell, wie dem erweiterten Hubbard-Modell

$$\mathcal{H} = \underbrace{-\sum_{i\neq j,\sigma} t_{ij} c^\dagger_{i\sigma} c_{j\sigma}}_{\text{Hopping-Term}} + \underbrace{U \sum_i n_{i\uparrow} n_{i\downarrow}}_{\text{Gitterplatz-Abstoßung}} + \underbrace{\sum_{i\neq j} V_{ij} n_i n_j}_{\text{Coloumb-Wechselwirkung}} + \underbrace{\sum_{i\neq j} J_{ij} \boldsymbol{S}_i \cdot \boldsymbol{S}_j}_{\text{Magnetische Wechselwirkung}} \tag{1}$$

mit den Teilchenzahloperatoren $n_{i\sigma}$ und den Erzeugungs- und Vernichtungsoperatoren $c^\dagger_{i\sigma}$ und $c_{i\sigma}$. t_{ij} entspricht einem verallgemeinerten kinetischen Term und U, V_{ij} und J_{ij} sind Kopplungsstärken. Aus den Wechselwirkungstermen kann man unterschiedliche Ordnungsparameter durch Entkoppeln der Wechselwirkungen mittels Mean-Field-Theorie gewinnen. Die passenden Ordnungsparameter müssen je nach Phänomenologie des Systems gewählt werden. Allerdings ist es möglich, theoretische Aussagen über die Ordnungsparameter zu treffen. Ein wichtiges Hilfsmittel sind diskrete Transformationen, wie die Rauminversion (oder Parität in 3D) $\mathcal{I}$, die Zeitumkehr $\mathcal{T}$, Ladungsumkehr $\mathcal{C}$ oder Punktgruppensymmetrien. Mittels dieser diskreten Transformationen können Ordnungsparameter klassifiziert werden. Ordnungsparameter bzw. die entsprechenden Terme im Hamiltonoperator können invariant unter den gegebenen Transformationen sein. In diesem Fall bezeichnet man die entsprechenden Transformationen als Symmetrien des Systems. In dieser Arbeit wenden wir die Klassifikationsmethoden auf Ordnungsparameter für Systeme mit Dichtewellen und Supraleitung an. Zuerst konzentrieren wir uns auf spezielle stark anisotrope Systeme mit einem kinetischen Term der folgenden Form im Hamiltonoperator

$$\mathcal{H}_{\text{kin}} = \sum_{\boldsymbol{k},\sigma,\sigma'} t_z \cos k_z c^\dagger_{\boldsymbol{k}\sigma} c_{\boldsymbol{k}\sigma'} + \sum_{\boldsymbol{k},\sigma,\sigma'} t(\cos k_x + \cos k_y) c^\dagger_{\boldsymbol{k}\sigma} c_{\boldsymbol{k}\sigma'} . \tag{2}$$

Der kinetische Term im Hamiltonoperator führt bei halber Füllung zu einer rechteckigen Fermifläche. In diesem Fall kann ein kommensurabler Wellenvektor $\boldsymbol{Q}$ gefunden werden, der die beiden Seiten der Fermifläche verbindet (siehe Abbildung 1). Das System kann dann eine Tendenz zur Bildung von Dichtewellen aufweisen, wobei eine physikalisch messbare Größe im Raum moduliert wird. Beispielsweise gibt es Ladungs- oder Spindichtewellen. Für die unterschiedlichen Dichtewellen kann man Ordnungsparameter aufstellen, die wir in dieser Arbeit klassifizieren. Die starke Anisotropie in z-Richung setzen wir voraus $t_z \ll t$. Wir betrachten die Punktgruppe D_{4h}, die zur Beschreibung der Rotationssymmetrie von rechtwinkligen quasi-2D-Systemen geeignet ist. Abbildung 2 zeigt die Spiegelebenen und Rotationsachsen der Punktgruppe. Für die Punktgruppe untersuchen wir im Detail einen Symmetriebrechungsmechanismus,

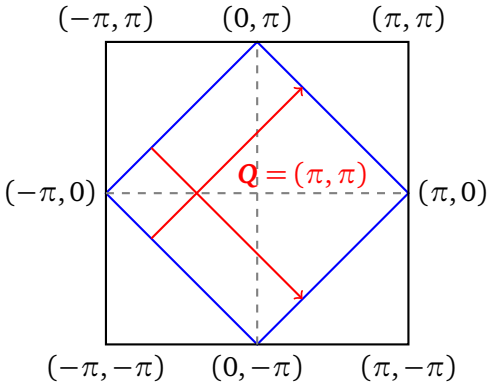

Abbildung 1: Brillouin-Zone für den kinetischen Term $\cos k_x + \cos k_y = 0$ in Blau. Bei halber Füllung liegt perfektes Nesting vor. Der kommensurable Vektor $\boldsymbol{Q} = (\pi, \pi)$ verbindet die Seiten der Fermifläche.

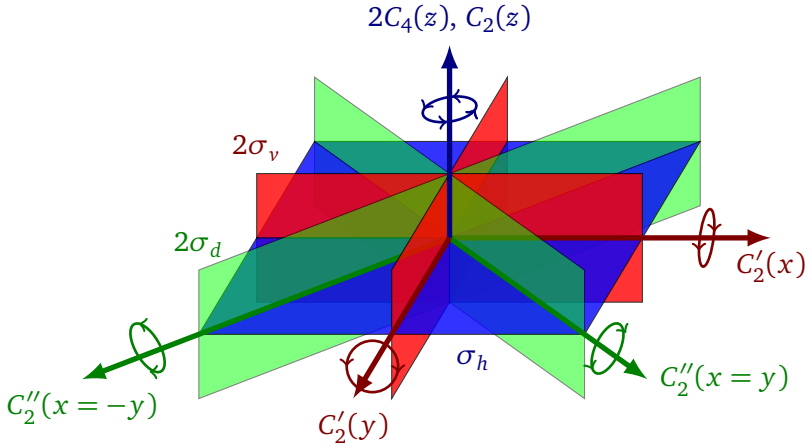

Abbildung 2: Spiegelebenen und Rotationsachsen der dihedralen Punktgruppe D_{4h}.

der darauf beruht, dass unterschiedliche Darstellungen der Punktgruppe im Hamiltonoperator auftreten.

Ein anderer Aspekt, der in dieser Diplomarbeit beleuchtet wird, ist die Existenz von topologischen Phasen. Diese haben die Besonderheit, dass sie nicht durch Symmetriebrechung und einen Ordnungsparameter, sondern durch eine topologische Invariante beschrieben werden. Eine bekannte topologische Invariante, die in dieser Arbeit diskutiert wird, ist die TKNN oder erste Chern-Zahl

$$C_1 = \frac{1}{4\pi} \int_{\mathrm{BZ}} dk_x\, dk_y\, \hat{\boldsymbol{g}} \cdot \left(\frac{\partial \hat{\boldsymbol{g}}}{\partial k_x} \times \frac{\partial \hat{\boldsymbol{g}}}{\partial k_y} \right) \tag{3}$$

die für einen Hamiltonoperator der folgenden Form definiert ist

$$\widehat{\mathcal{H}}(\boldsymbol{k}) = \epsilon(\boldsymbol{k}) + \boldsymbol{g}(\boldsymbol{k}) \cdot \boldsymbol{\sigma}\,. \tag{4}$$

Die „topologische Konfiguration" des Systems ist durch das Vektorfeld $\boldsymbol{g}(\boldsymbol{k})$ bestimmt. $\boldsymbol{\sigma} = (\sigma_x, \sigma_y, \sigma_z)$ ist ein Vektor von Pauli-Matrizen. Der Wert des Integrals – die erste Chern-Zahl – nimmt nur ganzzahlige Werte an. Topologische Phasenänderungen des Systems werden durch Änderung der Zahl beschrieben. Das berühmteste physikalische System, das mittels der Chern-Zahl beschrieben werden kann, ist der Interger-Quanten-Hall-Effekt, bei dem die Leitfähigkeit in der Ebene quantisiert ist. Wir betrachten im Detail allerdings den Quanten-Spin-Hall-Effekt, bei dem Hamiltonoperators der obigen Form auftreten.

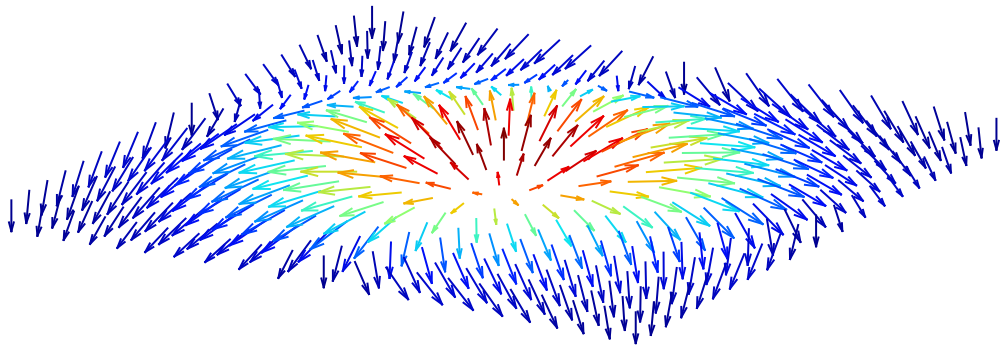

Abbildung 3: Skyrmion des anomalen Quanten-Hall-Effekts

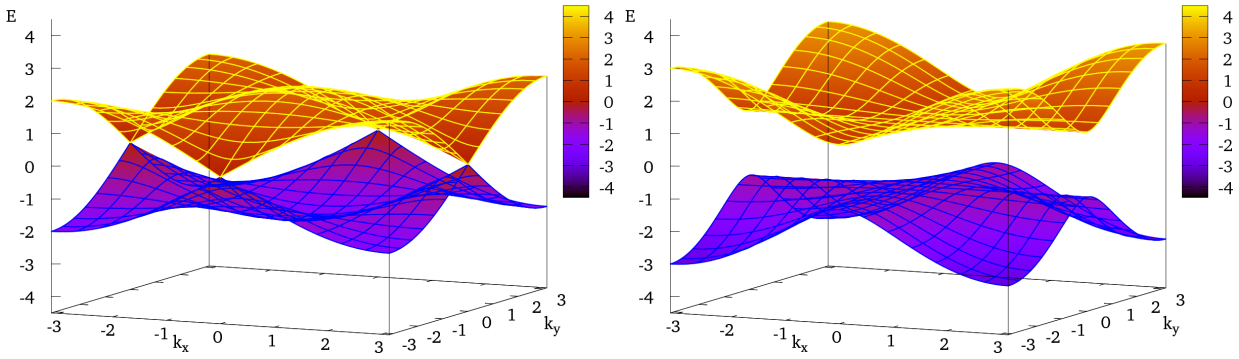

(a) Geschlossene Bandlücke, topologischer Phasenübergang

(b) Topologisch nichttrivaler Zustand des anomalen Quanten-Hall-Effekts mit nicht verschwindener topologischer Invariante $C_1 = 1$

Abbildung 4: Bänder des anomalen Quanten-Hall-Effekts

Die Spinleitfähigkeit ist dann mittels der Chern-Zahl festgelegt. Da in die Berechnung der Chernzahl nur der Vektor $\boldsymbol{g}(\boldsymbol{k})$ eingeht, bietet es sich an, dieses Vektorfeld auf der Brillouin-Zone zu darzustellen (Siehe Abbildung 3). Im Fall des Quanten-Spin-Hall-Systems oder genauer des anomalen Quanten-Hall-Systems, der als Teilsystem eines Quanten-Spin-Hall-Systems auftritt, erhält man eine Struktur namens „Skyrmion", benannt nach T. Skyrme, der diese zuerst als stabile Feldkonfigurationen in einem nichtlinearen Sigma-Modell beschrieb. Skyrmionen sind topologische Solitonen, bei denen sich die Vektorrichtung dreht. Berechnet man die Chern-Zahl des gegebenen Skyrmions, so erhält man $C_1 = 1$. Ein System mit Quanten-Spin-Hall-Effekt ist invariant unter Zeitumkehr. Die Leitfähigkeit des Systems entsteht durch sogenannte Helikale Randmoden, die jeweils aus zwei chiralen Randmoden bestehen. Die Moden zeigen Spin-Impuls-Locking, das heißt die Impulsrichtung ist an die Spinrichtung gebunden. Chirale Randmoden treten beim Integer-Quanten-Hall-Effekt alleine auf, da die Spinrichtung durch das äußere Magnetfeld fixiert ist. Das führt dazu, dass der Integer-Quanten-Hall-Effekt nicht invariant unter Zeitumkehr ist. Topologische Phasenübergänge eines Systems sind verbunden mit sich schließenden Bandlücken. Diese lassen sich durch die Bedingung $\boldsymbol{g}(\boldsymbol{k}) = 0$ finden. Abhängig von den Parametern des Modells schließen bzw. öffnen sich Bandlücken. Somit lässt sich ein topologisches Phasendiagramm erstellen. Ein weiterer Teil dieser Arbeit beschäftigt sich mit der Klassifikation von Hamiltonoperatoren nach den verallgemeinerten Symmetrietransformationen Zeitumkehr Θ, Ladungsumkehr Ξ und chirale Symmetrie Π. Je nachdem ob ein Hamiltonoperator diese Symmetrien aufweist oder nicht, fällt der Operator in eine unterschiedliche Symmetrieklasse. Die Symmetrieklasse ist direkt damit verbunden, ob das System topologische Invarianten aufweisen kann. Diese Methodik geht auf die Symmetrieklassifikation von Zufallsmatrizen zurück [1]. Das Resultat dieser Klassifikation ist die periodische Tabelle von topologischen Isolatoren und Supraleitern. Die periodische Tabelle unterscheidet insgesamt zehn

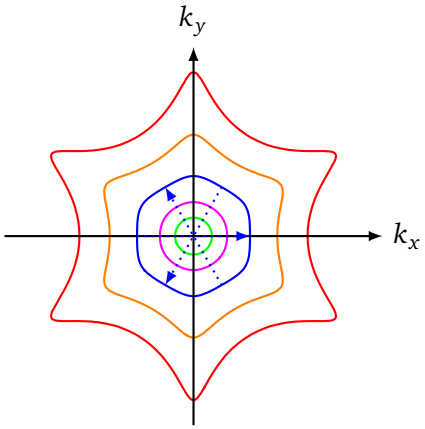

Abbildung 5: Schneeflockenstruktur der Fermifläche für unterschiedliche Werte des chemischen Potentials μ. Für $\mu = 0.725E^*$ bildet sich ein nahezu perfektes Sechseck. Wir zeigen drei inkommensurable Wellenvektoren.

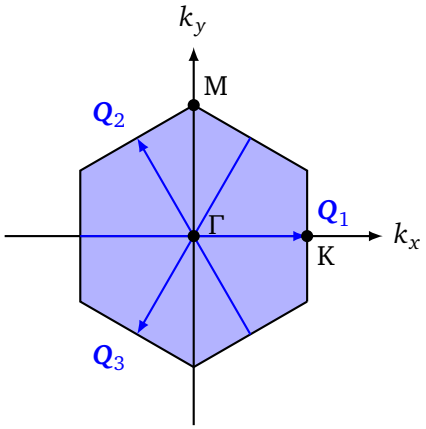

Abbildung 6: Fermifläche in perfekter Nesting-Situation mit den drei inkommensurablen Wellenvektoren $\boldsymbol{Q}_{1,2,3}$.

Symmetrieklassen und acht Raumdimensionen. Für höhere Raumdimensionen greift die sogenannte Bott-Periodizität, die dazu führt, dass sich die Tabelle in der Dimension mit der Periode acht wiederholt. Wir wenden diese Klassifikationsmethoden auf 2×2 und 4×4 Hamiltonoperatoren an. Als Resultat finden wir alle mögliche Konfigurationen abhängig von den Kommutationsrelationen der im Hamiltonoperator beteiligten Ordnungsparamter. Dieses Resultat kann dazu verwendet werden Hamiltonoperatoren mit gewünschten algebraischen und topologischen Eigenschaften aufzustellen.

In dieser Arbeit wenden wir die Methoden der topologischen Phasenübergänge und der Symmetrieklassifikation von Ordnungsparametern auf ein Modellsystem mit topologischen Dichtewellen an, das gegeben ist durch

$$\begin{aligned}\widehat{\mathcal{H}}(\boldsymbol{k}) = &\underbrace{-t(\cos k_x + \cos k_y)\tau_z\rho_z}_{\text{Hopping}} \\ &+ \underbrace{M_0^{\mathrm{C}}\tau_z\rho_x}_{\text{Ladungsdichtewelle}} + \underbrace{M_0^{\mathrm{S}}\tau_z\rho_x\sigma_z}_{\text{Spindichtewelle}} \\ &+ \underbrace{M_{x^2-y^2}^{\mathrm{C}}(\cos k_x - \cos k_y)\rho_y}_{\text{Singlet } id_{x^2-y^2}\text{-Dichtewelle}} + \underbrace{M_{xy}^{\mathrm{C}}\sin k_x \sin k_y \tau_z\rho_x}_{\text{Singlet } d_{xy}\text{-Dichtewelle}} \\ &+ \underbrace{M_{x^2-y^2}^{\mathrm{S}}(\cos k_x - \cos k_y)\rho_y\sigma_z}_{\text{Triplet } id_{x^2-y^2}\text{-Dichtewelle}} + \underbrace{M_{xy}^{\mathrm{S}}\sin k_x \sin k_y \tau_z\rho_x\sigma_z}_{\text{Triplet } d_{xy}\text{-Dichtewelle}}\,. \end{aligned} \tag{5}$$

Dieses System kombiniert mehrere bekannte Ordnungsparameter, die in Materialien wie den Cupraten vorkommen, und weist ein reichhaltiges Phasendiagramm auf, wenn man die Koexistenz der Phasen voraussetzt. Schließlich wenden wir unsere Methodik auf die Oberflächenmoden des 3D topologischen Isolators Bi_2Te_3 an, der zu den 3D topologischen Isolatoren zweiter Generation zählt. Ein 3D topologischer Isolator weist eine große Bandlücke im Bulk auf, die topologische Struktur führt zu leitenden Oberflächenmoden, ähnlich zu den Randmoden der Hall-Effekte. Die Fermifläche der Oberflächenmoden dieser topologischen Isolatoren ist üblicherweise rund und zeigt einen Dirac-Kegel. Allerdings tritt bei Bi_2Te_3 eine Verziehung der Fermifläche auf, so dass bei einem gewissen chemischen Potential eine schneeflockenartige Struktur entsteht. Wir zeigen die Fermifläche für unterschiedliche chemische Potentiale in Abbildung 5. Für einen bestimmten Wert des chemischen Potentials bildet die Fermifläche ein Sechseck. In diesem Fall besteht die Möglichkeit zur Ausbildung von Spindichtewellen. Die

Abbildung 7: s-Wellen-Supraleiter auf Bi_2Te_3

Seiten der Fermifläche werden durch drei inkommensurable Wellenvektoren $\boldsymbol{Q}_{1,2,3}$ verbunden (Siehe Abbildung 6). Wir entwickeln einen Spinorformalisms zur Klassifikation von Ordnungsparametern und führen eine Klassifikation möglicher Spindichtewellenordnungsparameter durch. Dabei setzen wir gewisse Symmetrieeigenschaften wie zum Beispiel Erhaltung der Punktgruppe C_{3v} voraus. Wir finden Ordnungsparameter mit einer Rashba-, Helizitäts- und Ising-artigen algebraischen Struktur. Für jeden der gefundenen Ordnungsparameter bestimmen wir die Magnetisierung und berechnen die Suszeptibilitäten. Schließlich kombinieren wir den 3D topologischen Isolator Bi_2Te_3 mit einem s-Wellen-Supraleiter. Durch den Proximity-Effekt tunneln Cooper-Paare in den Isolator. Effektiv entsteht ein topologischer Supraleiter. Wir untersuchen das Auftreten von Majorana-Zuständen. Diese Majorana-Zustände können zur Entwicklung topologischer Quantencomputer genutzt werden. In unserem System finden wir drei Subsysteme (entsprechend den drei Wellenvektoren $\boldsymbol{Q}_{1,2,3}$) die abhängig von der Stärke des Ordnungsparameters für Spindichtewellen und abhängig vom Supraleitungsparameter Δ in den topologisch nicht-trivialen Zustand übergehen.

In der weiteren Arbeit wollen wir die Berechnungen der Ordnungsparameter für Spindichtewellen verfeinern und mikroskopische selbstkonsistente Rechnungen durchführen. Damit soll das thermodynamische Phasendiagramm genauer untersucht werden. Außerdem wollen wir den Proximity-Effekt detaillierter untersuchen.

Preface

Recently there has been a lot of interest in topological phases in condensed matter systems. The reviews [2, 3] cover the latest developments. In this thesis we focus on systems exhibiting density waves and superconductivity. We perform a detailed symmetry classification of order parameters for density wave systems with a single commensurate vector $\boldsymbol{Q} = (\pi, \pi, \pi)$. This thesis is structured as follows:

In **Chapter 1** we introduce topological phases determined by non-zero topological invariants or equivalently by gap closings in the energy spectrum. We discuss the connection between topological invariants and topological defects called Skyrmions.

In **Chapter 2** we focus on topological classification of many-body Hamiltonians using generalized symmetries following the Altland and Zirnbauer (AZ) classification of random matrices. Using algebraic methods we find the classification of all 2×2 and 4×4 Hamiltonians.

In **Chapter 3** we introduce a basic Bogoliubov-de Gennes (BdG) formalism for order parameter classification using symmetries. We derive explicit formulas for inversion transformation $\mathcal{I}$, time reversal transformation $\mathcal{T}$, charge conjugation transformation $\mathcal{C}$ and point group transformations. The formalism is employed in the following chapters.

In **Chapter 4** we classify highly anisotropic lattice systems that exhibit density waves and superconductivity. We focus on the point group D_{4h} and symmetry breaking of the point group and its subgroups. Furthermore we concentrate on systems exhibiting one commensurate wave-vector $\boldsymbol{Q} = (\pi, \pi, \pi)$. For such a system we define all the accessible order parameters and perform a symmetry classification. Finally we study a concrete a model system with different types of coexisting density waves and determine the topological phases using topological invariants.

In **Chapter 5** we apply the symmetry and topological analysis to the surface states of the bulk topological insulator Bi_2Te_3 and investigate the possibilities for spin density wave phases. It has been proposed that bulk topological insulators in proximity to s-wave superconductors can be used to engineer topological superconductors which show Majorana states. We discuss the coexistence of a spin density wave phase and superconductivity and retrieve the values for the superconducting gap parameter Δ and the strength of the spin density wave order parameter that lead to Majorana modes.

The final **Chapter 6** concludes this thesis, summarizes the results and gives an outlook on further work.

Acknowledgments

At first I want to thank all members of the Institut für Theoretische Festkörperphysik for numerous inspiring and enlightening discussions. Without them this work would not have been possible. Especially I want to thank Professor Dr. Gerd Schön and Professor Dr. Alexander Shnirman for offering to me the possibility to work on this thesis and my advisor Dr. Panagiotis Kotetes for the great support. I really enjoyed our discussions. I am also deeply grateful for the support during difficult times. Then I want to thank my diploma colleagues Christian Karlewski and Sebastian Zanker for the nice coffee breaks, the humor and the pleasant working atmosphere in room 11.22. Many thanks go also to Andreas Heimes who was helpful and patient while explaining things like ARPES to me. I dedicate the nicer (gnu)plots in this thesis to him.

I am grateful for the support by the Studienstiftung des Deutschen Volkes during my whole physics studies. I participated in three summer schools organized by the Studienstiftung which were very interesting and stimulating.

I want to thank my old and new friends that I met during the physics studies and which made the studies interesting and enjoyable. Finally I want to thank my family, my sister and my brother for being the best sister and brother respectively and my parents for the financial support and the support in all the other more important aspects, for example the numerous care packages prepared by my mother.

Thank you all!

Notations

We follow some general rules for matrices and vectors. We use hats for matrices $\hat{m}$ while we denote the matrix elements m_{ij} without a hat. Due to historical conventions some special matrices are denoted without hat, e.g. the Pauli matrices. Vectors $\boldsymbol{v}$ are denoted in bold font while vector components v_i are denoted in normal font. For unit vectors $\hat{\boldsymbol{v}}$ we use a bold font with hat. Row vectors are written without comma, e.g. $\boldsymbol{k}^\intercal = \begin{pmatrix} k_x & k_y & k_z \end{pmatrix}$, but for convenience we sometimes write $\boldsymbol{k} = (k_x, k_y, k_z)$ which could either mean a row or column vector depending on context.

Pauli/Gell-Mann matrices

$\boldsymbol{\sigma} = (\sigma_x, \sigma_y, \sigma_z)$	Pauli matrix vector
$\{\mathbb{1}_\sigma, \sigma_x, \sigma_y, \sigma_z\}$	Pauli matrices for spin space
$\{\mathbb{1}_{\tau\sigma}, \sigma_x, \tau_z\sigma_y, \sigma_z\}$	Reducible Pauli matrices for spin in combined particle-hole and spin space
$\{\mathbb{1}_\tau, \tau_x, \tau_y, \tau_z\}$	Pauli matrices for Nambu particle-hole space
$\{\mathbb{1}_\rho, \rho_x, \rho_y, \rho_z\}$	Pauli matrices used for additional degree of freedom in the spinor
$\{\mathbb{1}_\lambda, \lambda_1, \ldots, \lambda_8\}$	Gell-Mann matrices

Nambu spinors

$\hat{\psi}_{\boldsymbol{k}}^\dagger = \begin{pmatrix} c_{\boldsymbol{k}\uparrow}^\dagger & c_{\boldsymbol{k}\downarrow}^\dagger \end{pmatrix}$	Nambu spinor in band space, e.g. spins
$\widehat{\Psi}_{\boldsymbol{k}}^\dagger = \begin{pmatrix} \hat{\psi}_{\boldsymbol{k}}^\dagger & \hat{\psi}_{\boldsymbol{k}+\boldsymbol{Q}}^\dagger \end{pmatrix}$	Nambu spinor in additional band space, e.g. for different momenta
$\hat{\chi}_{\boldsymbol{k}}^\dagger = \begin{pmatrix} \widehat{\Psi}_{\boldsymbol{k}}^\dagger & \widehat{\Psi}_{-\boldsymbol{k}}^\intercal \end{pmatrix}$	Nambu spinor in particle hole and band space

Generalized symmetry operators used for random matrix classification

$\Theta = \mathcal{K} U_\Theta$	Generalized antiunitary time reversal operator
$\Xi = \mathcal{K} U_\Xi$	Generalized antiunitary charge conjugation operator
$\Pi = U_\Pi$	Generalized unitary chiral symmetry operator

Hamilton operators

$\mathcal{H}$	Hamilton operator
$\widehat{\mathcal{H}}$	Hamilton operator in matrix form
$\widehat{\mathcal{H}}(\boldsymbol{k})$	BdG Hamiltonian in matrix form

Symmetry operators used in the order parameter classification

$\mathcal{T}$	Time reversal operator
$\mathcal{I}$	Space inversion operator
$\mathcal{C}$	Unitary charge conjugation operator
$\overline{\mathcal{C}}$	Antiunitary charge conjugation operator
$\mathcal{G}_i$	Group element of group $\mathcal{G}$
$\mathcal{O}$	General operator
$\mathcal{U}$	Unitary operator
$\overline{\mathcal{U}} = \mathcal{U}\mathcal{K} = \mathcal{K}\mathcal{U}^*$	Antiunitary operator
$\mathcal{K}$	Complex conjugation operator
$\widehat{D}(\mathcal{O})$	Matrix representation of operator $\mathcal{O}$ in combined spaces
$\widehat{D}_\sigma(\mathcal{O})$	Matrix representation of operator $\mathcal{O}$ in σ space
$\hat{d}(\mathcal{O})$	Notation for matrix representation of operator $\mathcal{O}$ in band space

Groups and algebras

SU(N)	Special unitary Lie group of degree N

$\mathrm{SO}(N)$	Special orthogonal Lie group of degree N
$\mathfrak{su}(N)$	Lie algebra of $\mathrm{SU}(N)$
$\mathfrak{so}(N)$	Lie algebra of $\mathrm{SO}(N)$
Miscellaneous	
$\boldsymbol{k} = (k_x, k_y, k_z)$	3-momentum
$G^0(\boldsymbol{k}, ik_n)$	Non-interacting Green's function
ik_n	Fermionic Matsubara frequency
iq_n	Bosonic Matsubara frequency

Contents

Chapter 1

Introduction to topological phases

The existence of diverse phases of matter and the corresponding phase transitions play a fundamental role in physics. The gas, liquid and solid phases are well known, but nature shows a much richer variety of phases. In condensed matter physics we encounter phases such as (anti-)ferromagnetism, superconductivity, density waves and many more. Phase transitions can be described by spontaneous symmetry breaking as introduced by Landau. For example in a ferromagnet the orientation of the spins breaks the rotational symmetry of the system. The symmetry breaking is connected to non-zero expectation values of quantum mechanical operators. The non-zero expectation value lead to the definition of order parameters. Order parameters decouple interactions and are used for an effective description. In Sections 1.1 and 1.2 we discuss density wave phases and the corresponding order parameters.

In addition to the mentioned phases there exist topological phases and phase transitions which are not connected to spontaneous symmetry breaking. In Section 1.3 we describe the integer quantum Hall effect (IQHE) as an example of topological phases and after that we describe the quantum anomalous Hall effect (QAHE) and the quantum spin Hall effect (QSHE). The integer quantum Hall effect was discovered in 1980. It shows a quantization of the Hall conductivity. The quantum spin Hall effect was proposed in 2005 for graphene and later discovered for HgTe quantum wells [4, 5]. The interesting property of the quantum spin Hall effect is the presence of time reversal invariance. The latest development was the discovery of 3D topological insulators. These are insulators in the bulk with a large insulating band gap but time reversal protected gapless surface states. There is a similarity between the integer quantum Hall effect and topological insulators. The conductivity of both systems is due to modes at the boundary, in the integer quantum Hall effect at the edges and for the 3D topological insulator at the surface. This property is called bulk-boundary correspondence. 3D topological insulators were first discovered in $Bi_{1-x}Sb_x$. The next generation of 3D topological insulators were Bi_2Se_3 and Bi_2Te_3 which we will also discuss later in this thesis. The 3D topological insulators of the second generation have a larger bandgap in the bulk and exhibit only a single surface Dirac cone.

1.1 Density waves

Density waves are modulations of a physical quantity such as charge and spin which occur in materials with highly anisotropic band structure. A charge density wave (CDW) in 1D (similar to Fig. 1.1a which is in 2D) can be described by a Hamiltonian like

$$\mathcal{H}_{\mathrm{CDW}} = \sum_j (-1)^j c_j^\dagger c_j \,. \tag{1.1}$$

A transformation from Wannier to Bloch operators

$$c_k^\dagger = \frac{1}{\sqrt{N}} \sum_j e^{ik\cdot R_j} c_j^\dagger \Leftrightarrow c_j^\dagger = \frac{1}{\sqrt{N}} \sum_k e^{-ik\cdot R_j} c_k^\dagger \tag{1.2}$$

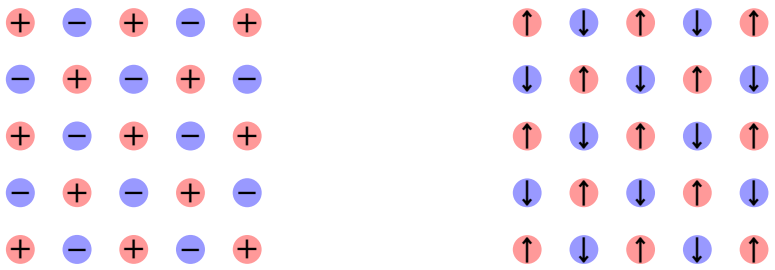

(a) Charge density wave (CDW) on a 2D lattice

(b) Spin density wave (SDW) on a 2D lattice

Figure 1.1: Charge and spin density waves

for the lattice sites at $R_j = a \cdot j$ yields in momentum space

$$\mathcal{H}_{\text{CDW}} = \sum_{kk'} \sum_{j} \frac{(-1)^j}{N} e^{iaj(k'-k)} c_k^\dagger c_{k'} \tag{1.3}$$

$$= \frac{1}{N} \sum_{kk'} \sum_{j} e^{ia2j(k'-k)} (1 - e^{ia(k'-k)}) c_k^\dagger c_{k'} \tag{1.4}$$

$$= \frac{N}{N} \sum_{k} c_k^\dagger c_{k+Q} (1 - e^{i\pi}) \tag{1.5}$$

$$= 2 \sum_{k} c_k^\dagger c_{k+Q} \,. \tag{1.6}$$

with the momentum transfer $Q = \pi/a$. Charge density waves might arise from electron-phonon interactions [6]. In the latter case, the electron-phonon coupling can lead to a lattice distortion which opens a gap Δ at the Fermi level at the same time breaking translational symmetry. The modified dispersion leads to a modulation of the electron density thus a charge density wave. In the next section we discuss order parameters in a more general manner.

1.2 Order parameters

Systems with phase transitions are described by order parameters. At first one usually starts with a microscopic model, e.g. an extended Hubbard model

$$\mathcal{H} = \underbrace{-\sum_{i \neq j, \sigma} t_{ij} c_{i\sigma}^\dagger c_{j\sigma}}_{\text{Hopping}} + \underbrace{U \sum_i n_{i\uparrow} n_{i\downarrow}}_{\text{On site repulsion}} + \underbrace{\sum_{i \neq j} V_{ij} n_i n_j}_{\text{Coloumb interaction}} + \underbrace{\sum_{i \neq j} J_{ij} \boldsymbol{S}_i \cdot \boldsymbol{S}_j}_{\text{Magnetic interaction}} \tag{1.7}$$

where $n_\sigma = c_{i\sigma}^\dagger c_{i\sigma}$ and $n_i = \sum_\sigma n_{i\sigma}$ are the number operators, $c_{i\sigma}^\dagger$ and $c_{i\sigma}$ are the creation and annihilation operators per lattice site i and spin σ respectively. The parameter t_{ij} describes a generalized kinetic term. U, V_{ij} and J_{ij} correspond to interaction strengths. We see that the $n_i n_j$ is a product of four creation and annihilation operators. For an effective description it is useful to perform an approximation, a so called mean field decoupling. At first, products of two operators are written as fluctuations around an expectation value. One can write for example

$$c_{i\sigma}^\dagger c_{j\sigma'}^\dagger = \langle c_{i\sigma}^\dagger c_{j\sigma'}^\dagger \rangle + \left(c_{i\sigma}^\dagger c_{j\sigma'}^\dagger - \langle c_{i\sigma}^\dagger c_{j\sigma'}^\dagger \rangle \right) \tag{1.8}$$

$$c_{i\sigma}^\dagger c_{j\sigma'} = \langle c_{i\sigma}^\dagger c_{j\sigma'} \rangle + \underbrace{\left(c_{i\sigma}^\dagger c_{j\sigma'} - \langle c_{i\sigma}^\dagger c_{j\sigma'} \rangle \right)}_{\text{Fluctuation}} . \tag{1.9}$$

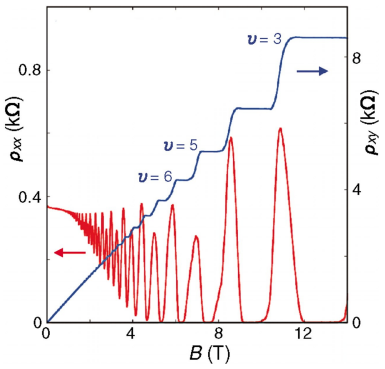

Figure 1.2: Quantized quantum Hall conductivity σ_{xy} (blue) depending on strength of perpendicular magnetic field B. The ratio of the resistivities ρ_{xx}/ρ_{xy} peaks at the phase transitions.

One introduces then variables for the mean values which are called order parameters

$$M_{ij\sigma\sigma'} \propto \langle c^\dagger_{i\sigma} c_{j\sigma'} \rangle, \quad \Delta_{ij\sigma\sigma'} \propto \langle c^\dagger_{i\sigma} c^\dagger_{j\sigma'} \rangle \,. \tag{1.10}$$

These can be used to decouple an interaction so that only products of two operators survive. Products of fluctuations are ignored and one obtains for example

$$\sum_{i\neq j} c^\dagger_{i\sigma} c_{i\sigma} c^\dagger_{j\sigma'} c_{j\sigma'} \approx \sum_{i\neq j} M_{ij\sigma\sigma'} c^\dagger_{j\sigma'} c_{i\sigma} + \sum_{i\neq j} M_{ij\sigma\sigma'} M_{ji\sigma'\sigma} \,. \tag{1.11}$$

However it is not obvious in which way an interaction has to be decoupled. Generally the relevant order parameters depend on the phenomenology and the phases of the physical system under consideration. The order parameters can lead to a symmetry breaking for example in the case of ferromagnetism which breaks the rotational symmetry of the system or superconductivity which breaks the U(1) gauge symmetry.

1.3 Integer quantum Hall effect

Since the discovery of the integer quantum Hall (IQHE) effect by von Klitzing [7] in the 80s and the consequent connection of the phenomena to a topological invariant a lot of efforts focused on understanding and exploring topological systems. In the IQHE the quantum Hall conductivity in the xy-plane, σ_{xy}, takes the quantized values

$$\sigma_{xy} = \frac{e^2}{h}\nu \tag{1.12}$$

where ν is an integer. Quantum Hall conductivity can be understood using Landau level quantization where the ν corresponds to the number of filled levels. Another possibility to understand the phenomenon is via topology and topological invariants. The integer number ν is in fact a topological invariant which is often called the TKNN number after the authors Thouless, Kohmoto, Nightingale and de Nijs [8, 9]. Among mathematicians the invariant is named first Chern number. The topological invariant is connected to the Berry phase [10] of the eigenvalues of the IQHE. In an IQHE system time reversal symmetry is broken due to the presence of a magnetic field.

1.4 Quantum anomalous Hall effect

The quantum anomalous Hall effect (QAHE) is similar to the integer quantum Hall effect with the difference that no magnetic field is present. Like the IQHE the topological phases are described by a

topological invariant called the first Chern number. The case in which the topological invariant vanishes defines the topologically trivial phase, compared to the non-trivial phases with a non-zero topological invariant. Systems exhibiting QAHE have not been discovered in nature yet but occur for example as subsystems in the quantum spin Hall effect which we discuss in the next section.

For the QAHE a configuration with a non-zero topological invariant is called a Skyrmion which was discovered by T. Skyrme as stable field configuration in the Skyrme model (topological solitons). This is the reason why it deserves the name ending "on" which is reserved for stable particles or excitations. The QAHE can be described by Hamiltonian of the form

$$\widehat{\mathcal{H}}(\boldsymbol{k}) = \epsilon(\boldsymbol{k}) + \boldsymbol{g}(\boldsymbol{k}) \cdot \boldsymbol{\sigma} \tag{1.13}$$

where $\boldsymbol{g}$ is an arbitrary vector field defined on some compact topological space and $\boldsymbol{\sigma} = (\sigma_x, \sigma_y, \sigma_z)$ are the Pauli matrices. The system configuration is defined by the vector field $\boldsymbol{g}$. For a certain configuration we can calculate the first Chern number $\boldsymbol{k} \to \widehat{\mathcal{H}}(\boldsymbol{k})$ (which is in fact the mapping $\boldsymbol{k} \to \boldsymbol{g}(\boldsymbol{k})$) which is given by

$$C_1 = \frac{1}{4\pi} \int dk_x\, dk_y \frac{\boldsymbol{g}}{|\boldsymbol{g}|^3} \cdot \left(\frac{\partial \boldsymbol{g}}{\partial k_x} \times \frac{\partial \boldsymbol{g}}{\partial k_y} \right) \tag{1.14}$$

$$= \frac{1}{4\pi} \int dk_x\, dk_y\, \hat{\boldsymbol{g}} \cdot \left(\frac{\partial \hat{\boldsymbol{g}}}{\partial k_x} \times \frac{\partial \hat{\boldsymbol{g}}}{\partial k_y} \right). \tag{1.15}$$

It can be shown that this number is a topological invariant. This means that it doesn't change under smooth deformations of the mapping. In physical terms the Chern number doesn't change under deformations which don't yield gap closings in the energy spectrum of the Hamiltonian. This is a useful tool if we want to identify topological phases. We can look either for gap closings or directly for changes in topological invariants. We observe that the topological invariant is independent of the length of the vector $\boldsymbol{g}(\boldsymbol{k})$ which corresponds to the energy scale. This means that the Chern number describes the topology of the mapping $\boldsymbol{k} \to \hat{\boldsymbol{g}}(\boldsymbol{k})$ with $\boldsymbol{k} = (k_x, k_y)$ defined in a compact topological space. The target space of unit vectors $\hat{\boldsymbol{g}}(\boldsymbol{k})$ is isomorphic to the sphere S^2 since every unit vector corresponds to a point on the sphere S^2 and vice versa.

Before we continue the discussion of momentum space topological defects we have first to consider the topology of the space where the $\boldsymbol{k}$ vectors are defined. As already mentioned it is crucial that this space is compact. This means non-compact spaces have to be compactified. Let's start with a simple example of a space which is already compact - the sphere S^2. In this case the Chern number is computed as follows

$$C_1 = \frac{1}{4\pi} \int_0^{\pi} d\theta \int_0^{2\pi} d\phi\, \hat{\boldsymbol{g}} \cdot \left(\partial_\theta \hat{\boldsymbol{g}} \times \partial_\phi \hat{\boldsymbol{g}} \right). \tag{1.16}$$

A non-trivial configuration is given for example by

$$\hat{\boldsymbol{g}}(\theta, \phi) = (\cos A\phi \sin\theta,\, \sin A\phi \sin\theta,\, \cos\theta) \tag{1.17}$$

which is for $A = 1$ just the parametrization of the sphere and gives us in fact $C_1 = A$. For $A > 1$ we find multiple Skyrmions distributed over the sphere which give a higher value for the topological invariant $C_1 = A > 1$. A can be seen as some kind of "winding number" which counts the number of times the $\boldsymbol{k}$ sphere is wrapped around the $\hat{\boldsymbol{g}}(\boldsymbol{k})$ target sphere. Now we see what happens if $\boldsymbol{k}$ live in a non-compact space. We define

$$\boldsymbol{g}_{\pm}(r, \phi) = (r \cos A\phi,\, r \sin A\phi,\, \pm 1) \tag{1.18}$$

which is just the linearized version of the $\boldsymbol{g}$ around $\theta = 0,\, \pi$. $\boldsymbol{g}_{\pm}$ is now defined in cylindrical coordinates. Integration of $\boldsymbol{g}_{\pm}$ with $r \in [0, \infty]$ yields $C_1 = \pm A/2$. The Chern number is not integer anymore! What

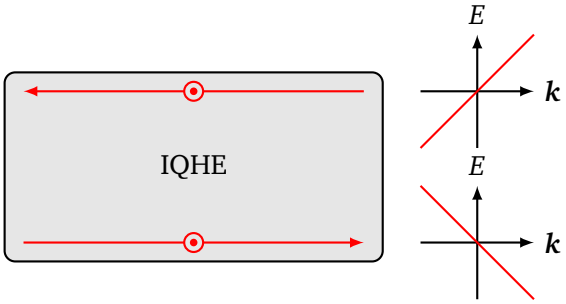

(a) Integer quantum Hall effect with chiral edge modes. Spin direction is fixed by magnetic field.

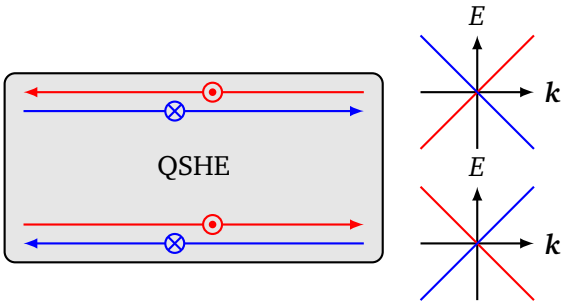

(b) Quantum spin Hall effect with helical edge modes which are made up from two chiral edge modes each.

Figure 1.3: Integer quantum Hall and quantum spin Hall effect in comparison (adapted from [11])

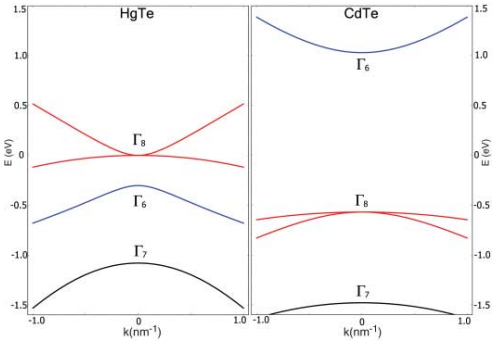

(a) Bulk bands of HgTe and CdTe near Γ

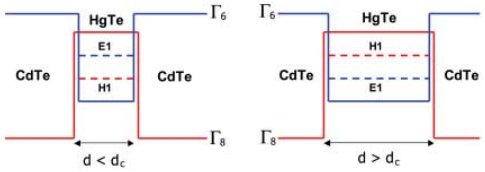

(b) The CdTe-HgTe-CdTe quantum well in the normal regime with E1 > H1, $d < d_c$ and in the inverted (topologically non-trivial) regime with E1 < H1, $d > d_c$

Figure 1.4: HgTe quantum wells, adapted from [4]

happened? We computed the Chern number for two non-compact half-spheres where $\boldsymbol{g}_+$ corresponds to the field on the northern hemisphere and $\boldsymbol{g}_-$ corresponds to the field on the southern hemisphere. The half topological invariant is not that of a Skyrmion but that of a half Skyrmion, a so called Meron. Compactification means that we glue the two hemispheres together at the equator creating a compact spherical space out of the two infinite planes.

1.5 Quantum spin Hall effect

Now let's discuss the quantum spin Hall effect (QSHE) which exhibits non-trivial momentum space topology. In the QSHE spin flows dissipationless and is carried by helical edge states in two-dimensional systems. Helical edge states show spin momentum locking, which means that the flow direction fixes or locks the spin. The QSHE preserves time reversal symmetry. A single edge mode with, let's say spin up and momentum $\boldsymbol{k}$, by itself breaks time reversal symmetry and is termed chiral. Combined with another chiral edge mode with spin down and momentum $-\boldsymbol{k}$ time reversal symmetry is preserved leading to helical edge modes. An even number of helical edge modes can hybridize by impurity scattering or interactions making the system topologically trivial by opening a gap at the edge. An odd number of edge modes corresponds to a topologically non-trivial system. As a matter of fact the topology can then be described by a $\mathbb{Z}_2$ invariant. The QSHE was first proposed for graphene [12, 13]. However it could not been discovered due to the too weak spin orbit interaction. Later the QSHE was proposed for HgTe quantum wells [5, 4] and experimentally discovered [14]. A HgTe quantum well of thickness d is "sandwiched" by two CdTe layers. In order to observe the QSHE, the thickness d has to be larger than a

certain critical thickness d_c. The essential properties of the system can be described by a 6 band model

$$\left\{|\Gamma_6,+1/2\rangle\,,\,|\Gamma_6,-1/2\rangle\,,\,|\Gamma_8,+3/2\rangle\,,\,|\Gamma_8,+1/2\rangle\,,\,|\Gamma_8,-1/2\rangle\,,\,|\Gamma_8,-3/2\rangle\right\}\,. \tag{1.19}$$

These bands can be combined linearly to form three spin up and three spin down bands respectively

$$\{|\mathrm{H1},+3/2\rangle\,,\,|\mathrm{E1},+1/2\rangle\,,\,|\mathrm{L1},+1/2\rangle\,,\,|\mathrm{H1},-3/2\rangle\,,\,|\mathrm{E1},-1/2\rangle\,,\,|\mathrm{L1},-1/2\rangle\}\,. \tag{1.20}$$

The $|\mathrm{H1},\pm 3/2\rangle$ is formed by the $|\Gamma_8,\pm 3/2\rangle$ states, the $|\mathrm{E1},\pm 1/2\rangle$ is formed by linear combination of the $|\Gamma_6,\pm 1/2\rangle$ and the $|\Gamma_8,\pm 1/2\rangle$ bands. The L1 bands are separated from the other bands so that they can be omitted in the effective description leaving a four band model

$$\{|\mathrm{H1},+3/2\rangle\,,\,|\mathrm{E1},+1/2\rangle\,,\,|\mathrm{H1},-3/2\rangle\,,\,|\mathrm{E1},-1/2\rangle\,,\,\}\,. \tag{1.21}$$

At $d = d_c$ a band inversion occurs and the system transits to the topologically non-trivial QSHE. The states with angular momentum $\pm 1/2$ have even parity, the states with angular momentum $\pm 3/2$ have odd parity. This implies that the mixing matrix element between two such states must be odd under inversion. The simplest possible Hamiltonian to describe the required properties has the form

$$\begin{aligned}\widehat{\mathcal{H}}(\boldsymbol{k}) &= \begin{pmatrix}\hat{h}(\boldsymbol{k}) & 0\\ 0 & \hat{h}^*(-\boldsymbol{k})\end{pmatrix}\,,\\ \hat{h}(\boldsymbol{k}) &= \epsilon(\boldsymbol{k}) + \boldsymbol{g}(\boldsymbol{k})\cdot\boldsymbol{\rho}\end{aligned}$$

with the Pauli matrix vector $\boldsymbol{\rho} = (\rho_x, \rho_y, \rho_z)$. The block diagonal form of the Hamiltonian ensures time reversal symmetry, the mixing functions $g_{1,2}(\boldsymbol{k})$ have to be odd and the functions $\epsilon(\boldsymbol{k})$ and $g_3(\boldsymbol{k})$ have to be even because of the parity of the different angular momenta. Since each of the block corresponds to a spin direction, we can rewrite the Hamiltonian as follows

$$\begin{aligned}\widehat{\mathcal{H}}(\boldsymbol{k}) &= \begin{pmatrix}\hat{h}_\uparrow(\boldsymbol{k}) & 0\\ 0 & \hat{h}_\downarrow(\boldsymbol{k})\end{pmatrix}\,,\\ \hat{h}_\sigma(\boldsymbol{k}) &= \epsilon(\boldsymbol{k}) + \boldsymbol{g}_\sigma(\boldsymbol{k})\cdot\boldsymbol{\rho}\,.\end{aligned}$$

In a tight binding model which is defined on the compact Brillouin zone the lowest-order crystal harmonics which fulfill the properties are given by

$$\epsilon(\boldsymbol{k}) = C + D(\cos k_x + \cos k_y)\,, \tag{1.22}$$

$$\boldsymbol{g}_\sigma(\boldsymbol{k}) = \begin{pmatrix}\sigma A \sin k_x\\ A\sin k_y\\ B(\cos k_x + \cos k_y - M)\end{pmatrix} \tag{1.23}$$

where A, B, C, D and M are parameters of the material or experimental setup. The parameter M corresponds to the well thickness d. The wave vectors live in the Brillouin zone $\boldsymbol{k} \in [-\pi,\pi]^2$, which is glued together at both edges giving rise to the topology of a torus T^2. The Brillouin zone is therefore a compact space and the Hamiltonian reflects this by a 2π periodicity (Only sin and cos functions appear in $\boldsymbol{g}_\sigma(\boldsymbol{k})$). We set $A = B = M = 1$ and plot the given vector field

$$\boldsymbol{g}(\boldsymbol{k}) = \left(\sin k_x,\, \sin k_y,\, \cos k_x + \cos k_y - 1\right) \tag{1.24}$$

to obtain the vector field configuration of the Skyrmion in Fig. 1.7 and the associated Merons in Fig. 1.8 when linearized around $\boldsymbol{k} = 0$. We see that the Hamiltonian $\hat{h}_\sigma(\boldsymbol{k})$ has an inherent U(1) symmetry (rotation of the $\boldsymbol{g}(\boldsymbol{k})$ vector around z-axis in the configuration space of the $\boldsymbol{g}$ vectors). This rotation corresponds to a change between the different point group representations, e.g. for no rotation one obtains $\sin k_x\sigma_x + \sin k_y\sigma_y$ which is a helicity term. For a rotation by 90° one obtains $\sin k_x\sigma_y - \sin k_y\sigma_x$

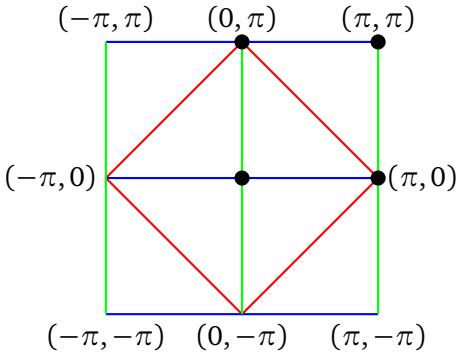

Figure 1.5: The relevant low energy points in the Brillouin zone. The low energy points lie at the intersections of the lines where $\sin k_x$, $\sin k_y$ and $\cos k_x + \cos k_y$ are zero.

which is a Rashba-term. The U(1) symmetry is reflected by a degeneracy in the Skyrmion configurations. For each of the subblocks we can compute the Chern number as described before by

$$C_1^\sigma = \frac{1}{4\pi}\int dk_x\, dk_y\, \hat{\boldsymbol{g}}_\sigma \cdot \left(\frac{\partial \hat{\boldsymbol{g}}_\sigma}{\partial k_x} \times \frac{\partial \hat{\boldsymbol{g}}_\sigma}{\partial k_y}\right). \tag{1.25}$$

The Chern number is directly proportional to the in plane charge conductivity $\sigma_{xy}^\sigma = -C_1^\sigma$ in appropriate units. Due the block diagonal form of the total Hamiltonian $\widehat{\mathcal{H}}(\boldsymbol{k})$ and $\sigma_{xy}^\uparrow = -\sigma_{xy}^\downarrow$ there is no charge conductivity $\sigma_{xy}^{\mathrm{C}} = \sigma_{xy}^\uparrow + \sigma_{xy}^\downarrow = 0$. However there can be spin conductivity $\sigma_{xy}^{\mathrm{S}} = \sigma_{xy}^\uparrow - \sigma_{xy}^\downarrow = 2\sigma_{xy}^\uparrow$. One can say that the system consists of two copies of the quantum anomalous Hall effect. Each copy itself breaks time reversal symmetry. The whole system is time reversal invariant. The Chern number can be used to define a $\mathbb{Z}_2$ invariant $N_2 \in \mathbb{Z}_2$ which describes the topological phases of the system appropriately

$$N_2 \equiv \sigma_{xy}^\uparrow \equiv \sigma_{xy}^\downarrow \mod 2. \tag{1.26}$$

Consequently the QSHE falls into the symmetry class AII while the quantum anomalous Hall effect subsystems break all symmetries and fall into symmetry class A. The symmetry classes are described in Chapter 2. In the next step we want to determine the topological phases of the QSHE. For this reason we find the gap closings of the Hamiltonian. Gap closings occur for $M = 0, \pm 2$ when $\boldsymbol{g}(\boldsymbol{k}) = 0$. For the different values of M we find the following points

$$\begin{aligned} M &= -2 \quad \Gamma = (0,0), \\ M &= 0 \quad (\pi,0) \equiv (-\pi,0),\ (0,\pi) \equiv (0,-\pi), \\ M &= +2 \quad (\pi,\pi) \equiv (-\pi,\pi) \equiv (\pi,-\pi) \equiv (-\pi,-\pi). \end{aligned}$$

which can also be called low energy points since they determine the low energy behavior of the system (see also Fig. 1.5). Since the low energy behavior is determined around the low energy points we can linearize the Hamiltonian around these points. The linearized vector fields are given by

$$(0,0): \quad \boldsymbol{g}_\sigma(\boldsymbol{k}) = (\sigma A \cdot k_x, A \cdot k_y, B(2-M)), \tag{1.27}$$
$$(\pi,0): \quad \boldsymbol{g}_\sigma(\boldsymbol{k}) = (-\sigma A \cdot k_x, A \cdot k_y, -BM), \tag{1.28}$$
$$(0,\pi): \quad \boldsymbol{g}_\sigma(\boldsymbol{k}) = (\sigma A \cdot k_x, -A \cdot k_y, -BM), \tag{1.29}$$
$$(\pi,\pi): \quad \boldsymbol{g}_\sigma(\boldsymbol{k}) = (-\sigma A \cdot k_x, -A \cdot k_y, -B(2+M)). \tag{1.30}$$

Now we compute the topological invariants around the low energy points using the linearized model giving us four Merons, four times $\pm 1/2$. The sum of the Merons gives the whole topological invariant of the Skyrmion. As a result we find the phases for the spin up quantum anomalous Hall subblock in Table 1.1. The band structure of the two energy bands of the quantum anomalous Hall system for each of the relevant phases is given in Fig. 1.6.

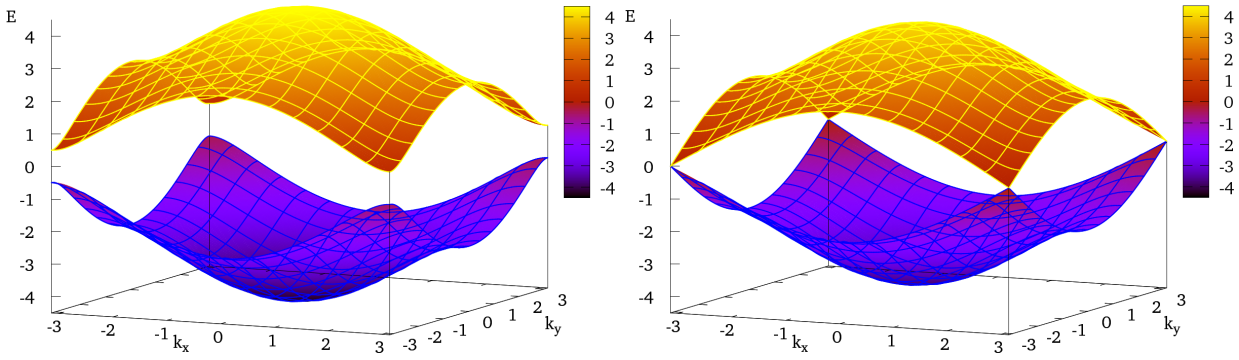

(a) Trivial phase for $M = -2.5$.

(b) Gap closing for $M = -2$.

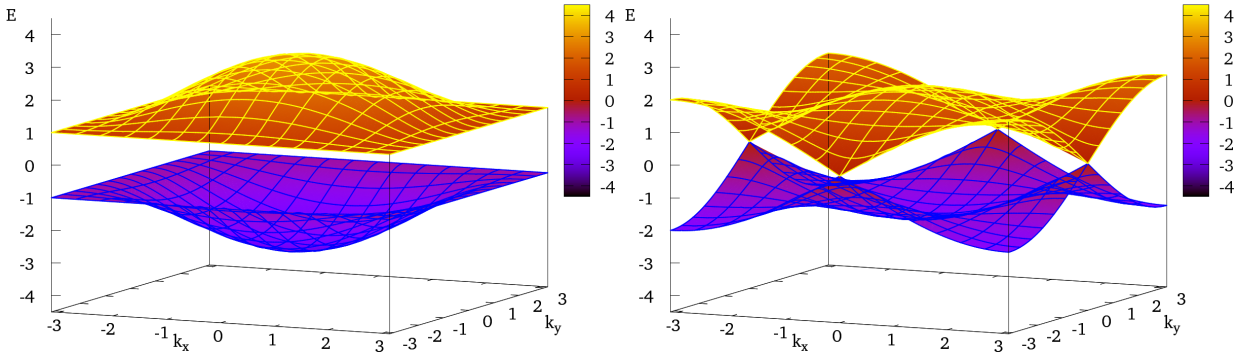

(c) Topological phase for $M = -1$ with the spin conductivity $\sigma^{S}_{xy} = +2$.

(d) Gap closing for $M = 0$.

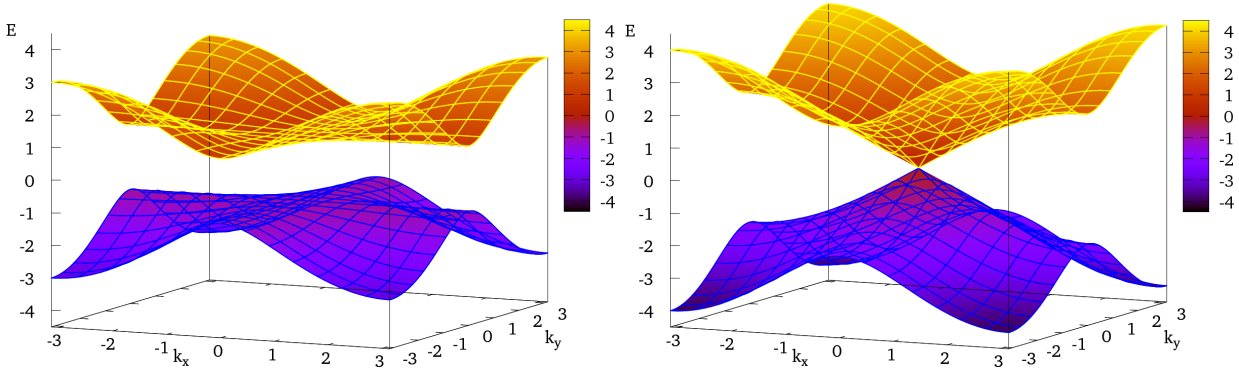

(e) Topological phase for $M = 1$ with the spin conductivity $\sigma^{S}_{xy} = -2$.

(f) Gap closing for $M = 2$.

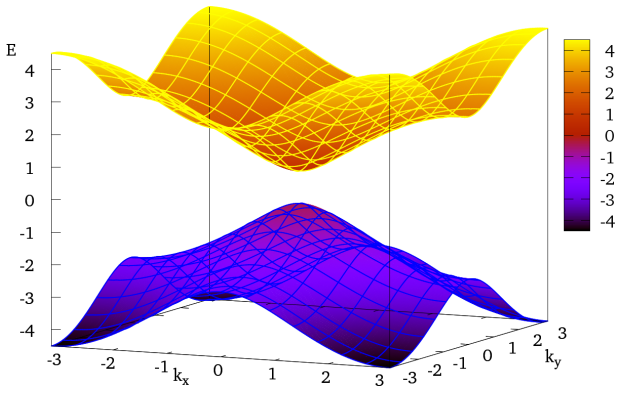

(g) Trivial phase for $M = 2.5$.

Figure 1.6: Band structure of the two bands of the quantum anomalous Hall system which occurs twice in the quantum spin Hall system.

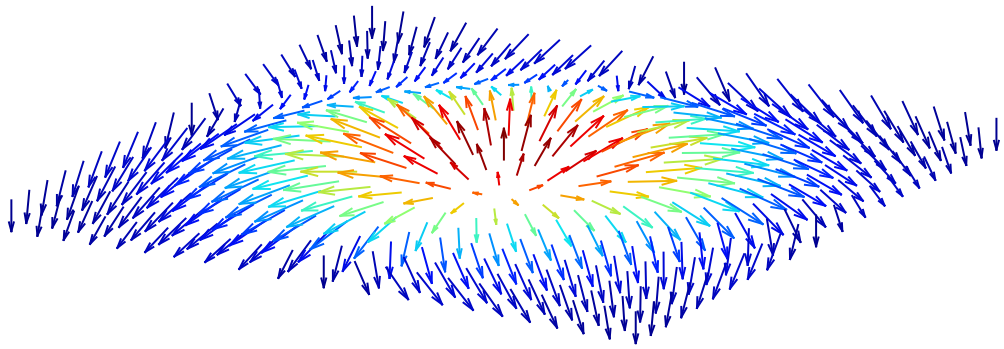

(a) No rotation

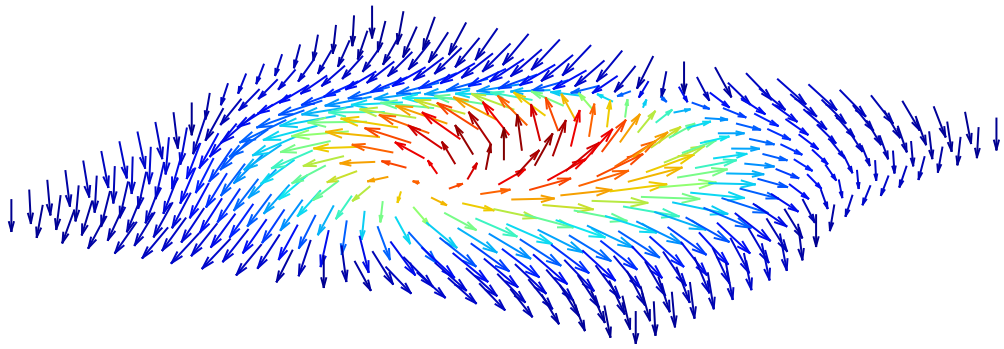

(b) Rotation by 45°

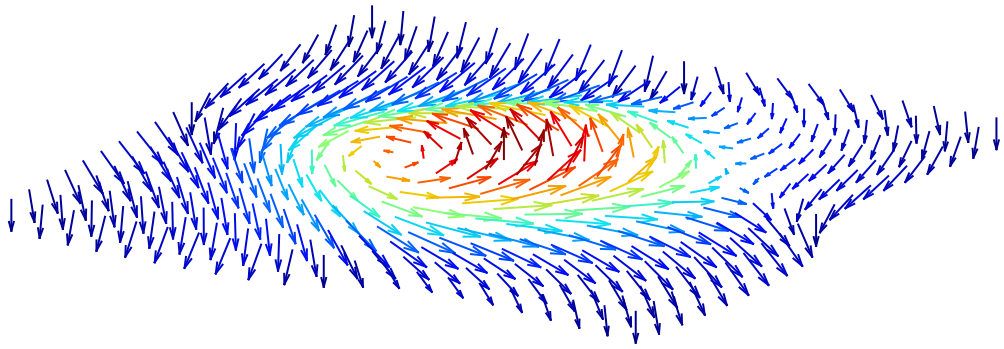

(c) Rotation by 90°

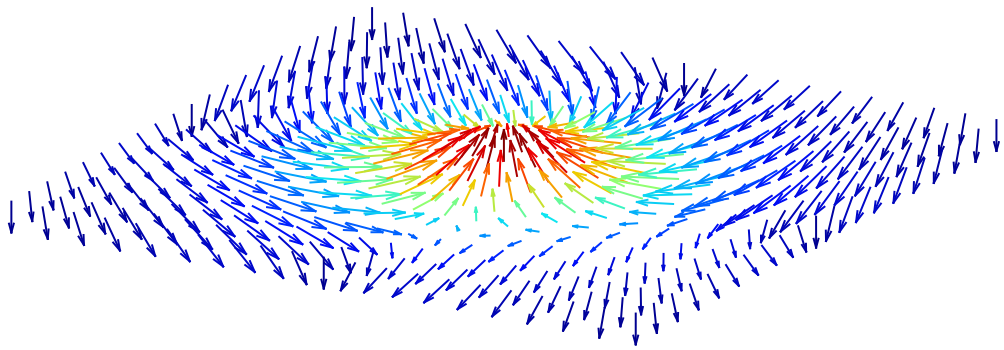

(d) Rotation by 180°

Figure 1.7: Skyrmion configuration $\boldsymbol{g}(\boldsymbol{k}) = (\sin k_x, \sin k_y, \cos k_x + \cos k_y - 1)$ defined on $[-\pi, \pi]^2$ with topological invariant $C_1 = 1$. We show different rotations of the normalized field vectors $\hat{\boldsymbol{g}}(\boldsymbol{k})$ around the z-axis. The rotation doesn't affect the topological invariant C_1. The vector field is actually defined on a torus T^2. This means the opposite boundaries have to be glued together (identified).

Table 1.1: Topological phases of the quantum anomalous Hall effect. The essential properties of the Hamiltonian are captured by linear expansion of the Hamiltonian around the low-energy points of the Brillouin zone $(0,0)$, $(\pi,0)$, $(0,\pi)$ and (π,π). Gap closings can occur only at these points. Computing the sum over the Merons at each of the points gives the value 1 for the topological invariant of the Skyrmion.

Phase		$\sigma^{\uparrow}_{xy}$		$(0,0)$	$(\pi,0)$	$(0,\pi)$	(π,π)
Trivial	$M<-2$	0	=	$-1/2$	$+1/2$	$+1/2$	$-1/2$
Gap closing	$M=-2$						
Topological	$-2<M<0$	$+1$	=	$-1/2$	$+1/2$	$+1/2$	$+1/2$
Gap closing	$M=0$						
Topological	$0<M<2$	-1	=	$-1/2$	$-1/2$	$-1/2$	$+1/2$
Gap closing	$M=2$						
Trivial	$2<M$	0	=	$+1/2$	$-1/2$	$-1/2$	$+1/2$

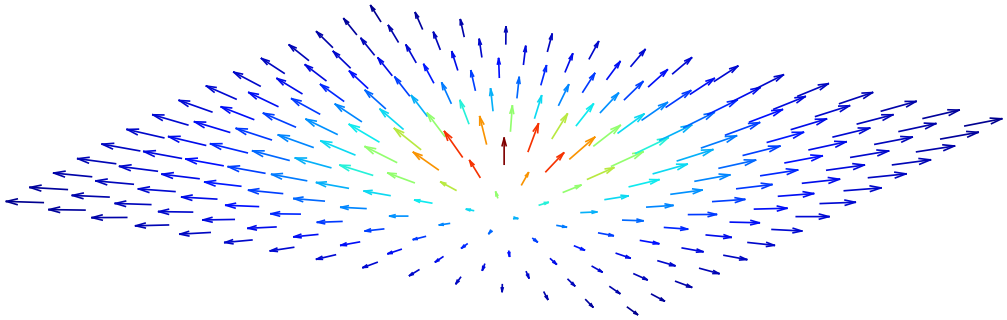

(a) Meron corresponding to $\boldsymbol{g}_+$

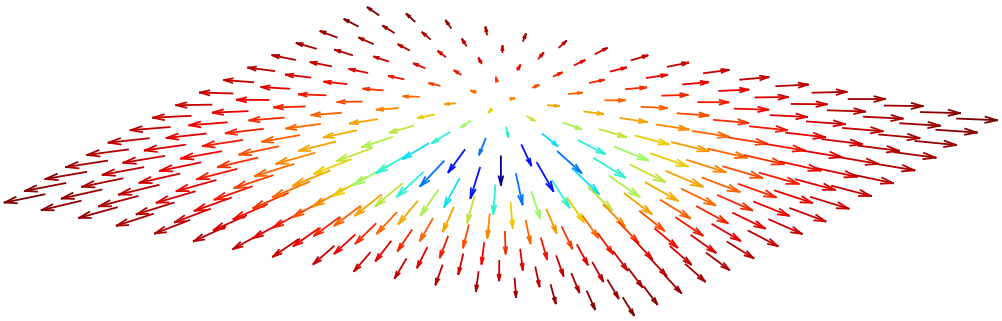

(b) Anti-Meron corresponding to $\boldsymbol{g}_-$

Figure 1.8: Meron and anti-Meron configurations for the linear model $\boldsymbol{g}_\pm(\boldsymbol{k}) = (k_x, k_y, \pm 1)$ with topological charge $C_1 = \pm 1/2$. The plots shows the normalized vectors $\hat{\boldsymbol{g}}_\pm(\boldsymbol{k})$.

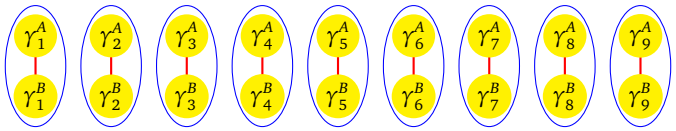

(a) Chain in a topologically trivial configuration where all Majorana operators are coupled.

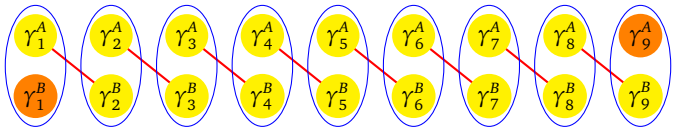

(b) Chain in a topologically non-trivial configuration with two Majorana operators. The Majorana edge states γ_1^B and γ_9^A are uncoupled and don't appear in the Hamiltonian.

Figure 1.9: p-wave superconducting chain with the Majorana operators $\gamma_i^{A,B}$ which arise after canonical transformations of the p-wave Hamiltonian.

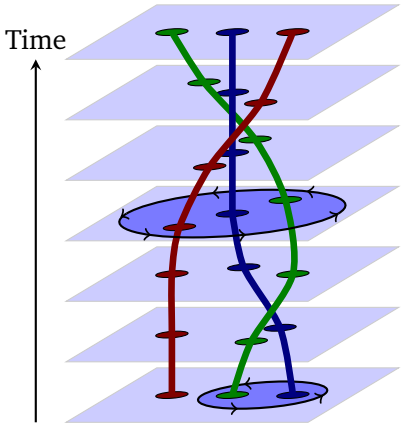

(a) Three Majorana anyons on a plane

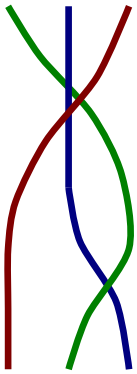

(b) Braid (Element of braiding group B_3) which corresponds to movement of Majorana anyons

Figure 1.10: Braiding performed with three Majorana modes living on a plane

1.6 Majorana modes and topological quantum computation

Ettore Majorana found purely real solutions of the Dirac equation. They describe particles which are their own anti-particles. It has been debated if neutrinos are Majorana or Dirac particles. In condensed matter systems Majorana modes can occur as excitations. Within a simple model, Kitaev [15] showed how Majorana bound states can appear at the boundaries of an 1D p-wave superconducting chain. The Majorana operators are either all coupled and appear in the Hamiltonian or leave two uncoupled Majorana edge states as in Fig. 1.9.

It has been proposed that Majorana bounds states can be used for implementing qubits which could be used to perform topological quantum computation. The key assumption is that Majorana qubits are topologically protected against local fluctuations compared to classical qubits like the superconducting flux or charge qubits and the spin qubits. This is due to the delocalized nature of the topological qubit implemented by Majorana bound states which live at the edges of e.g. a nanowire.

Operations on the Majorana qubits are carried using braiding operations [16] which are essentially adiabatic movement operations on the Majorana bound states using their non-abelian statistics as shown in Fig. 1.10. Interestingly the Majorana qubits are topologically protected while performing the operations. However, braiding operations cannot be used to build a complete set of quantum gates. The implementation of a complete set of gates makes the combination with either classical qubit operations or the use of non-adiabatic and topologically non-protected operations necessary.

Chapter 2

Topological classification

In this chapter we focus on topology and the topological properties of Hamiltonians. The topological classification is based on symmetry considerations. Altland and Zirnbauer (AZ) classified [1] random matrices using generalized time reversal symmetry Θ, charge conjugation symmetry Ξ and chiral symmetry Π. The AZ classification is built upon the well-known Wigner-Dyson classification [17, 18] which uses only time reversal symmetry. An important assumption for this kind of classification scheme is that all other symmetries are broken. In random matrix theory, which can be used to described disordered systems this condition is trivially fulfilled. For symmetric non-random systems we have to carefully check for additional space group symmetries [19]. Depending on the generalized symmetries we can distinguish ten different symmetry classes. These different symmetry classes show periodic topological properties which can be summarized in the periodic table [20]. The periodic table assigns a $\mathbb{Z}$ or $\mathbb{Z}_2$ invariant to each symmetry class and space dimension. A $\mathbb{Z}$ invariant is a number which can take integer values. If we compute a $\mathbb{Z}$ invariant for a physical system we can distinguish different topological phases. The fundamental property of the invariants is that they don't change under small perturbations of the Hamiltonian in such a way that no gap openings or closings in the energy spectrum occur. $\mathbb{Z}_2$ invariants can only take two values.

In some cases topological invariants are directly connected to measurable physical quantities. For example in the integer quantum Hall effect (IQHE) [7] the measured integer quantized Hall conductivity σ_{xy} is proportional to a $\mathbb{Z}$ invariant know as the first Chern number [8, 9]. Another example is the more recently discovered quantum spin Hall effect (QSHE) [4, 14] which exhibits a $\mathbb{Z}_2$ invariant. We have already described the IQHE and the QSHE in Chapter 1.

2.1 Periodic table of topological phases

The Altland and Zirnbauer (AZ) classification [1] of random matrices is built upon three fundamental symmetries: the generalized time reversal symmetry Θ, charge conjugation symmetry Ξ and chiral symmetry Π. The periodic table [20] which is shown in Table 2.1 assigns a $\mathbb{Z}$ or $\mathbb{Z}_2$ invariant to each symmetry class and space dimension. The names of the symmetric spaces are due to Élie Cartan who carried out an exhaustive classification. The entire classification contains symmetry spaces which depend on the matrix size N and spaces which have a fixed matrix size (due to the exceptional Lie groups). The periodic table only covers the spaces which depend on matrix size N since these allow the description of arbitrarily large physical systems. However for small systems the other cases might be useful.

We observe that the table is shown only up to dimension 8 because this covers all cases. Bott-periodicity states that the same patterns repeats itself for higher dimension. The symmetry classes A and AIII show a two Bott-periodicity in dimension. These cases are called complex cases since no reality condition is imposed on the Hamiltonian in these cases. We will describe this in the next section when we focus on the generalized symmetries. The other symmetry classes are real classes and they show a periodicity by eight in the dimension. Bott-periodicity is a very powerful phenomenon which appears in multiple branches of mathematics, in particular algebraic topology. The stable homotopy groups of

Table 2.1: Periodic table. The symmetries Θ, Ξ and Π lead to the distinction of ten cases. Cases with $\Pi = 1$ are termed chiral. The table is only shown up to dimension 8 due to Bott-periodicity.

Symmetry					**Dimension**						
		Θ	Ξ	Π	1	2	3	4	5	6	7	8
A	unitary	0	0	0	0	$\mathbb{Z}$	0	$\mathbb{Z}$	0	$\mathbb{Z}$	0	$\mathbb{Z}$
AIII	chiral unitary	0	0	1	$\mathbb{Z}$	0	$\mathbb{Z}$	0	$\mathbb{Z}$	0	$\mathbb{Z}$	0
AI	orthogonal	1	0	0	0	0	0	$\mathbb{Z}$	0	$\mathbb{Z}_2$	$\mathbb{Z}_2$	$\mathbb{Z}$
BDI	chiral orthogonal	1	1	1	$\mathbb{Z}$	0	0	0	$\mathbb{Z}$	0	$\mathbb{Z}_2$	$\mathbb{Z}_2$
D	BdG	0	1	0	$\mathbb{Z}_2$	$\mathbb{Z}$	0	0	0	$\mathbb{Z}$	0	$\mathbb{Z}_2$
DIII	chiral BdG	-1	1	1	$\mathbb{Z}_2$	$\mathbb{Z}_2$	$\mathbb{Z}$	0	0	0	$\mathbb{Z}$	0
AII	symplectic	-1	0	0	0	$\mathbb{Z}_2$	$\mathbb{Z}_2$	$\mathbb{Z}$	0	0	0	$\mathbb{Z}$
CII	chiral symplectic	-1	-1	1	$\mathbb{Z}$	0	$\mathbb{Z}_2$	$\mathbb{Z}_2$	$\mathbb{Z}$	0	0	0
C	BdG	0	-1	0	0	$\mathbb{Z}$	0	$\mathbb{Z}_2$	$\mathbb{Z}_2$	$\mathbb{Z}$	0	0
CI	chiral BdG	1	-1	1	0	0	$\mathbb{Z}$	0	$\mathbb{Z}_2$	$\mathbb{Z}_2$	$\mathbb{Z}$	0

the spheres show a Bott-periodicity. The $\mathbb{Z}$ and $\mathbb{Z}_2$ invariants in the periodic table are in fact the stable homotopy groups of the symmetry spaces. The homotopy groups of the symmetric spaces for large matrix sizes N become stable aka don't change anymore for large N. This what a stable homotopy group means [21].

2.2 Generalized unitary and antiunitary symmetries

At first we assume that the Hamiltonian operator $\widehat{\mathcal{H}}$ is hermitian and that there exist no other unitary operator which commutes with the Hamiltonian except the trivial scalar operators. This means that all symmetries of the system are broken. In the case of a many body Hamiltonian $\widehat{\mathcal{H}}(\boldsymbol{k})$ we have to consider also additional symmetries [19]. In Section 2.3 we discuss an example for an additional symmetry.

In the latter case there is a commuting matrix that can be simultaneously diagonalized with the Hamiltonian thus bringing the Hamiltonian in a block diagonal form. Then we can separately classify the blocks of the Hamiltonian. According to Wigner's theorem every symmetry acts as a unitary or antiunitary transformation. Since we already excluded all unitary commuting symmetries only three symmetries remain. We use a very general definition given in [22, 23] for the three symmetries that we call time reversal symmetry Θ, charge conjugation symmetry Ξ and chiral (or sublattice) symmetry Π. The definition of the symmetries is not necessarily connected to the definition of the physical symmetries which depends on the representation of the system for example in the BdG formalism. Time reversal symmetry and charge conjugation symmetry are defined as antiunitary operators which can be written as product of a unitary operator $\mathcal{U}$ and the complex conjugation operator $\mathcal{K}$, e.g. $\Theta = \mathcal{U}_\Theta^* \mathcal{K}$. We can equivalently define $\Theta = \mathcal{K}\mathcal{U}_\Theta$ (Be aware that $\mathcal{K}$ doesn't act on $\mathcal{U}_\Theta$ just yet). We define the chiral symmetry by $\Pi \equiv \Theta \cdot \Xi$ which gives a unitary operator. We define that a Hamiltonian operator $\widehat{\mathcal{H}}(\boldsymbol{k})$ has time reversal symmetry Θ, charge conjugation symmetry Ξ or chiral symmetry Π if the following relations are fulfilled respectively

$$\Theta: \quad \Theta^\dagger \widehat{\mathcal{H}}(\boldsymbol{k})\Theta = \mathcal{U}_\Theta^\dagger \widehat{\mathcal{H}}^*(-\boldsymbol{k})\mathcal{U}_\Theta = +\widehat{\mathcal{H}}(\boldsymbol{k}), \tag{2.1}$$

$$\Xi: \quad \Xi^\dagger \widehat{\mathcal{H}}(\boldsymbol{k})\Xi = \mathcal{U}_\Xi^\dagger \widehat{\mathcal{H}}^*(-\boldsymbol{k})\mathcal{U}_\Xi = -\widehat{\mathcal{H}}(\boldsymbol{k}), \tag{2.2}$$

$$\Pi: \quad \Pi^\dagger \widehat{\mathcal{H}}(\boldsymbol{k})\Pi = \mathcal{U}_\Pi^\dagger \widehat{\mathcal{H}}(\boldsymbol{k})\mathcal{U}_\Pi = -\widehat{\mathcal{H}}(\boldsymbol{k}) \tag{2.3}$$

where $\mathcal{U}_\Theta$, $\mathcal{U}_\Xi$ and $\mathcal{U}_\Pi$ are unitary matrices. We see that the existence of time reversal symmetry Θ and charge conjugation symmetry Ξ implies the existence of a chiral symmetry Π. The existence of time reversal symmetry Θ and chiral symmetry implies the existence of charge conjugation symmetry Ξ and vice versa. We write $\Theta = 0$ ($\Xi = 0$) for the absence of time reversal symmetry Θ (charge conjugation

symmetry Ξ). For the presence of time reversal symmetry Θ (charge conjugation symmetry Ξ) we write $\Theta = \pm 1$ ($\Xi = \pm 1$) depending on the square of the symmetry $\Theta^2 = \pm\mathbb{1}$ ($\Xi^2 = \pm\mathbb{1}$). In the physical interpretation, a symmetry can square to $-\mathbb{1}$ if the system behaves as a half-integer spin system. The chiral symmetry $\Pi = \Theta \cdot \Xi$ is necessary to distinguish the two cases $\Pi = 0$ and $\Pi = 1$ when $\Theta = \Xi = 0$. The symmetries Θ and Ξ can only square to ±1 since

$$(\mathcal{K}\mathcal{U})^\dagger \widehat{\mathcal{H}}(\boldsymbol{k})\mathcal{K}\mathcal{U} = \mathcal{U}^\dagger \widehat{\mathcal{H}}^*(-\boldsymbol{k})\mathcal{U} = \pm\widehat{\mathcal{H}}(\boldsymbol{k}) \tag{2.4}$$

$$\implies \left((\mathcal{K}\mathcal{U})^\dagger\right)^2 \widehat{\mathcal{H}}(\boldsymbol{k})(\mathcal{K}\mathcal{U})^2 = (\mathcal{U}^*\mathcal{U})^\dagger \widehat{\mathcal{H}}(\boldsymbol{k})\mathcal{U}^*\mathcal{U} = \widehat{\mathcal{H}}(\boldsymbol{k}) \tag{2.5}$$

$$\implies \left[\widehat{\mathcal{H}}(\boldsymbol{k}), \mathcal{U}^*\mathcal{U}\right] = 0 \tag{2.6}$$

where $\mathcal{U} = \mathcal{U}_\Theta, \mathcal{U}_\Xi$. Then $\mathcal{U}^*\mathcal{U}$ would be a unitary matrix which commutes with the Hamiltonian. Since we required that no other (non trivial) commuting matrices exist which leads to $\mathcal{U}^*\mathcal{U} = \pm\mathbb{1}$. No other symmetries of a Hamiltonian $\widehat{\mathcal{H}}$ are possible. This can be easily seen since

- if two different chiral symmetries $\Pi_1 = \mathcal{U}_1$ and $\Pi_2 = \mathcal{U}_2$ exist the product forms a unitary matrix $\Pi_1 \cdot \Pi_2 = \mathcal{U}_1\mathcal{U}_2$ which commutes with the Hamiltonian $\widehat{\mathcal{H}}(\boldsymbol{k})$ and we excluded this from the start.
- If two different time reversal symmetries $\Theta_1 = \mathcal{K}\mathcal{U}_1$ and $\Theta_2 = \mathcal{K}\mathcal{U}_2$ exist we would get a unitary matrix $\Theta_1 \cdot \Theta_2 = \mathcal{U}_1^*\mathcal{U}_2$ which would commute with the Hamiltonian $\widehat{\mathcal{H}}(\boldsymbol{k})$ and we excluded this from the start.
- If two different charge conjugation symmetries $\Xi_1 = \mathcal{K}\mathcal{U}_1$ and $\Xi_2 = \mathcal{K}\mathcal{U}_2$ exist we would get a unitary matrix $\Xi_1 \cdot \Xi_2 = \mathcal{U}_1^*\mathcal{U}_2$ which would commute with the Hamiltonian $\widehat{\mathcal{H}}(\boldsymbol{k})$ and we excluded this from the start.

Time reversal Θ and charge conjugation Ξ involve complex conjugation $\mathcal{K}$. If Θ and Ξ are absent one can say that no reality condition is imposed on the Hamiltonian $\widehat{\mathcal{H}}(\boldsymbol{k})$. The cases with $\Theta = \Xi = 0$ are therefore called complex cases. The corresponding complex classes in the periodic table show a Bott-periodicity by two.

2.3 Symmetry classification of 2×2 Hamiltonians

The simplest Hamiltonian we can classify using the AZ classification scheme is a 2×2 Hamiltonian. We can write a general 2×2 Hamiltonian in the form

$$\widehat{\mathcal{H}}(\boldsymbol{k}) = \epsilon(\boldsymbol{k}) + f_1(\boldsymbol{k})\,\sigma_1 + f_2(\boldsymbol{k})\,\sigma_2 + f_3(\boldsymbol{k})\,\sigma_3 \tag{2.7}$$

where $\epsilon(\boldsymbol{k})$ and f_i ($i = 1,2,3$) are arbitrary functions in $\boldsymbol{k}$ and σ_i are the Pauli matrices. We can permute the σ_i Pauli matrices in our definition because they anticommute. The functions $f_{1,2,3}$ can be either even (e.g. $f(k_x) = 1, k_x^2$), odd (e.g. $f(k_x) = k_x$) or asymmetric (neither even nor odd, e.g. $f(k_x) = k_x + k_x^2$). For asymmetric functions no time reversal Θ and no charge conjugation Ξ can exist.

We require that there is no commuting matrix. Otherwise the Hamiltonian could be block diagonalized. Therefore at least two f_i have to be nonzero. For each of the functions f_i we denote odd (even) behavior under inversion by + (−) in the following tables. For 2×2 Hamiltonians the chiral symplectic case CII cannot be reached since there are no two Pauli matrices with $\sigma_i^*\sigma_i = -\mathbb{1} \implies \sigma_i^\intercal = -\sigma_i$. We distinguish the following cases depending on $\epsilon(\boldsymbol{k})$.

- ϵ is present and asymmetric in $\boldsymbol{k}$ ($\epsilon(\boldsymbol{k}) \neq \pm\epsilon(-\boldsymbol{k})$): In this case all symmetries are broken and the resulting Hamiltonian belongs to class A.
- ϵ is present and even in $\boldsymbol{k}$ ($\epsilon(-\boldsymbol{k}) = +\epsilon(\boldsymbol{k})$): In this case charge conjugation and chiral symmetry are broken, since no matrix anticommutes with the identity matrix. Only time reversal symmetry Θ can exist, therefore we recover the standard Wigner-Dyson classes A, AI and AII. See Table 2.2.

- ϵ is present and odd in $\boldsymbol{k}$ ($\epsilon(-\boldsymbol{k}) = -\epsilon(\boldsymbol{k})$): In this case time reversal symmetry and chiral symmetry are broken, since no matrix anticommutes with the identity matrix. Only charge conjugation symmetry Ξ can exist. See Table 2.3.
- ϵ is absent ($\epsilon = 0$): This case is not as simple as the others since it allows for chiral symmetries. Constant energy shifts are prohibited in this case. Assume now that one f_i is asymmetric in $\boldsymbol{k}$ ($\exists i : f_i(\boldsymbol{k}) \neq \pm f_i(-\boldsymbol{k})$). In this case the only two classes are A (if all f_i are present) and AIII (if one f_i is absent). Assume now all f_i are either odd or even in $\boldsymbol{k}$ ($\forall i : f_i(\boldsymbol{k}) = \pm f_i(-\boldsymbol{k})$). In this case we can access the cases in Table 2.4. We see that the absence of one Pauli matrix leads to a chiral symmetry. The chiral symmetry is then given by the absent matrix itself.

Table 2.2: $\epsilon(-\boldsymbol{k}) = +\epsilon(\boldsymbol{k})$. Wigner-Dyson classes. $+$ ($-$) denotes even (odd) functions respectively and 0 means $f_i = 0$.

f_1	f_2	f_3	Θ	Ξ	Π		
$+$	$+$	$+$	0	0	0	**A**	unitary
$-$	$-$	$+$					
$-$	$+$	$0,+$	$+1$	0	0	**AI**	orthogonal
$+$	$+$	$0,-$					
$-$	$-$	$0,-$	-1	0	0	**AII**	symplectic

Table 2.3: $\epsilon(-\boldsymbol{k}) = -\epsilon(\boldsymbol{k})$. BdG classes. The red marked case with only odd functions leads to a gapless Hamiltonian. $+$ ($-$) denotes even (odd) functions respectively and 0 means $f_i = 0$.

f_1	f_2	f_3	Θ	Ξ	Π		
$-$	$+$	$+$	0	0	0	**A**	unitary
$-$	$-$	$-$					
$-$	$-$	$0,+$	0	$+1$	0	**D**	BdG
$-$	$+$	$0,-$					
$+$	$+$	$0,+$	0	-1	0	**C**	BdG

Table 2.4: $\epsilon(\boldsymbol{k}) = 0$. The cases with only odd functions lead to a gapless Hamiltonians. $+$ ($-$) denotes even (odd) functions respectively and 0 means $f_i = 0$.

f_1	f_2	f_3	Θ	Ξ	Π		
$-$	$+$	$+$	$+1$	0	0	**AI**	orthogonal
$-$	$-$	$+$	0	$+1$	0	**D**	BdG
$-$	$-$	$-$	-1	0	0	**AII**	symplectic
$+$	$+$	$+$	0	-1	0	**C**	BdG
$-$	$+$	0	$+1$	$+1$	1	**BDI**	chiral orthogonal
$+$	$+$	0	$+1$	-1	1	**CI**	chiral BdG
$-$	$-$	0	-1	$+1$	1	**DIII**	chiral BdG

By taking the example of 2×2 Hamiltonians we can shortly discuss the problem of additional symmetries which must also be checked if a symmetry classification of a Hamiltonian is performed. Let's consider the Hamiltonian

$$\widehat{\mathcal{H}}(k_x, k_y) = \epsilon + \sin k_x \sigma_x + \sin k_y \sigma_y + \sigma_z \quad k_x, k_y \in [-\pi, \pi] \tag{2.8}$$

which seems to have no additional symmetries. However the unitary transformation $\sigma_z \widehat{\mathcal{H}}(k_x+\pi, k_y+\pi)\sigma_z = \widehat{\mathcal{H}}(k_x, k_y)$ consisting of σ_z and a translation by (π, π) leaves the Hamiltonian invariant. This means that we have to somehow "block diagonalize" the system. This happens by going to a reduced Brillouin zone (RBZ) $[-\pi/2, \pi/2]^2$. The unitary symmetry $\sigma_z \widehat{\mathcal{H}}(k_x+\pi, k_y+\pi)\sigma_z = \widehat{\mathcal{H}}(k_x, k_y)$ still holds but now the translation is just a translation by the size of the RBZ and therefore not relevant since it connects points in the RBZ which were already identified. Remember that the RBZ has the topology of a torus T^2 which corresponds to gluing the edges of $[-\pi/2, \pi/2]^2$. The Hamiltonian defined on the RBZ belongs to class A since no other symmetries can be found.

2.4 Symmetry classification of 4×4 Hamiltonians

We perform a classification of 4×4 Hamiltonians. The 4×4 Hamiltonians are spanned by the $\mathfrak{su}(4)$ Lie algebra and the identity matrix $\mathbb{1}_4$. The $\mathfrak{su}(4)$ Lie algebra is spanned by 15 basis vectors. Thus a general Hamiltonian has the form

$$\widehat{\mathcal{H}}(\boldsymbol{k}) = \epsilon(\boldsymbol{k}) + \sum_{i=1}^{15} f_i(\boldsymbol{k})\,\Gamma_i\,. \tag{2.9}$$

We note that $\mathfrak{su}(4)$ is isomorphic to $\mathfrak{so}(6)$. The Lie algebra $\mathfrak{su}(4)$ spans the Lie group SU(4) whereas $\mathfrak{so}(6)$ spans the SO(6). The Lie groups SU(4) and SO(6) are locally isomorphic since they share exactly the same Lie algebra over the real numbers $\mathbb{R}$. However the Lie algebras can be spanned by different basis vectors, for example the $\mathfrak{su}(4)$ by the complex Pauli matrices compared to the real SO(6) generators which span the $\mathfrak{so}(6)$. For the following argumentation about the Lie algebras we follow [24]. The 15 basis vectors L_{ij} (with $i > j$) of $\mathfrak{so}(6)$ or equivalently the generators of the SO(6) fulfill the commutation relation

$$[L^{ij}, L^{km}] = i(\delta_{ik}L^{jm} + \delta_{jm}L^{ik} - \delta_{im}L^{jk} - \delta_{jk}L^{im})\,. \tag{2.10}$$

Thus we can organize the generators in a specific schema as shown in Table 2.5a. From the commutation relation we see that two generators commute if they share no common index. We also see that we can build $\mathfrak{so}(6-n)$ subalgebras by removing n columns and their corresponding rows from the table.

For the following analysis we don't have to fix a specific basis. The only requirement is that we restrict ourselves to purely real or imaginary generators as given by the Kronecker product of two Pauli matrices $\tau_i \otimes \sigma_j$. As an example we find specific generators of the SU(4) which fulfill the commutation relation as shown in Table 2.5b. For the symmetry classification we need at least four matrices, otherwise

Table 2.5: Generators of the SO(6). The generators fulfill the commutation relation Eq. (2.10) and can therefore organized in a table. The whole matrix is antisymmetric. Therefore the diagonal elements are zero. The diagonal elements and the elements above the diagonal are not shown here.

(a) General

L_{21}				
L_{31}	L_{22}			
L_{41}	L_{42}	L_{43}		
L_{51}	L_{52}	L_{53}	L_{54}	
L_{61}	L_{62}	L_{63}	L_{64}	L_{65}

(b) Specific basis given by Kronecker products of Pauli matrices

$-\tau_z\sigma_y$				
$+\tau_y$	$-\tau_x\sigma_y$			
$-\tau_z\sigma_z$	$-\sigma_x$	$+\tau_x\sigma_z$		
$-\tau_z\sigma_x$	$+\sigma_z$	$+\tau_x\sigma_x$	$-\sigma_y$	
$+\tau_x$	$+\tau_y\sigma_y$	$+\tau_z$	$+\tau_y\sigma_z$	$+\tau_y\sigma_x$

we would always find a commuting matrix, so we restrict ourselves us to the basic Hamiltonian

$$\widehat{\mathcal{H}}(\boldsymbol{k}) = \epsilon(\boldsymbol{k}) + f_1(\boldsymbol{k})\,\Gamma_1 + f_2(\boldsymbol{k})\,\Gamma_2 + f_3(\boldsymbol{k})\,\Gamma_3 + f_4(\boldsymbol{k})\,\Gamma_4\,. \tag{2.11}$$

This basic Hamiltonian is chiral since we can always find a matrix which anticommutes with all of the given ones. If we add more Γ matrices to the basic Hamiltonian we have to check if the added matrix breaks the chiral symmetry or not. From this we find to which classes the extended Hamiltonians belong. For now we concentrate on the basic Hamiltonian with only four Γ matrices. The four matrices cannot be arbitrary but have to be chosen in such a way that no commuting matrix is found, e.g. $\{\sigma_x, \tau_x, \tau_y, \tau_z\}$ are not acceptable since σ_x commutes with all of them. We distinguish the following cases depending on ϵ. If ϵ is present we cannot find a chiral symmetry.

- ϵ is present and asymmetric in $\boldsymbol{k}$ ($\epsilon(\boldsymbol{k}) \neq \pm\epsilon(-\boldsymbol{k})$): In this case all symmetries are broken and the resulting Hamiltonian belongs to class A.

- ϵ is present and even in $\boldsymbol{k}$ ($\epsilon(-\boldsymbol{k}) = +\epsilon(\boldsymbol{k})$). In this case we find no chiral symmetry, since no matrix anticommutes with the identity matrix. Additionally charge conjugation symmetry is broken. We can use the case $\epsilon = 0$ as starting point and find the class AI instead of BDI/CI and class AII instead of CII/DIII. We recovered the Wigner-Dyson classes which are non-chiral.

- ϵ is present and odd in $\boldsymbol{k}$ ($\epsilon(-\boldsymbol{k}) = -\epsilon(\boldsymbol{k})$): In this case we find no chiral symmetry, since no matrix anticommutes with the identity matrix. Additionally time reversal symmetry is broken. We can use the case $\epsilon = 0$ as starting point and find class D instead of BDI/DIII and C instead of CI/CII. In this case we found the non-chiral BdG classes.

- ϵ is absent ($\epsilon = 0$): This case is not as simple as the others since it allows for chiral symmetries. It can be used to describe systems with a robust particle-hole symmetry such as superconductors. We distinguish two subcases: Assume now that one function f_i is asymmetric in $\boldsymbol{k}$ ($\exists i : f_i(\boldsymbol{k}) \neq \pm f_i(-\boldsymbol{k})$). In this case the Hamiltonian falls into chiral class AIII. Assume now that all f_i are either odd or even in $\boldsymbol{k}$ ($\forall i : f_i(\boldsymbol{k}) = \pm f_i(-\boldsymbol{k})$). Then we get four distinct cases which we found by iterating all possible combinations of Γ matrices. We visualize the resulting cases using graphs. A node of a graph corresponds to a generator and an edge means that the connected generators anticommute. The $+$ or $-$ inside the node correspond to even or odd functions. In some cases we show nodes which are splitted in half and show $+$ and $-$. These graphs stand for two graphs similar to an equation with $\pm$ and $\mp$. The visualization using graphs reduces the number of separate cases we have to write down for the symmetry classes since graphs can be bended and deformed as shown in Fig. 2.1. In order to identify the case to which a Hamiltonian belongs one has to determine the anticommutation graph.

  - Case 1 (Four anticommuting generators, see Fig. 2.2). All generators anticommute pairwise. We can arrange the generators in the known schema which is shown in Fig. 2.2a. A simpler representation is possible using an anticommutation graph as in Fig. 2.2b which provides the anticommutation relation between the generators in a more accessible way. The graph Fig. 2.2c shows if the functions corresponding to the generators have to be odd or even. Depending on the functions the Hamiltonian falls into one of the chiral symmetry classes. We write an example Hamiltonian

$$\widehat{\mathcal{H}}(\boldsymbol{k}) = \boldsymbol{f}(\boldsymbol{k}) \cdot \tau_x \boldsymbol{\sigma} + g(\boldsymbol{k})\tau_y \,. \tag{2.12}$$

  - Case 2 ($L_{41} + L_{52} + L_{53} + L_{54}$, see Fig. 2.3). The generators L_{52} and L_{53} can be exchanged without changing the class. We show again the schema Fig. 2.2d, the anticommutation graph Fig. 2.2e and the different cases which lead to the corresponding symmetry classes Fig. 2.2f. We introduce the modified (reducible) Pauli matrices $\tilde{\boldsymbol{\sigma}} = (\sigma_x, \tau_z\sigma_y, \sigma_z)$ and write an example Hamiltonian

$$\widehat{\mathcal{H}}(\boldsymbol{k}) = \boldsymbol{f}(\boldsymbol{k}) \cdot \tau_x \tilde{\boldsymbol{\sigma}} + g(\boldsymbol{k})\tau_x\sigma_y \tag{2.13}$$

    where τ_x and $\tau_x\sigma_x$ are the matrices anticommuting with only one other matrix. In contrast $\tau_x\sigma_y$ and $\tau_y\sigma_y$ commute with two.

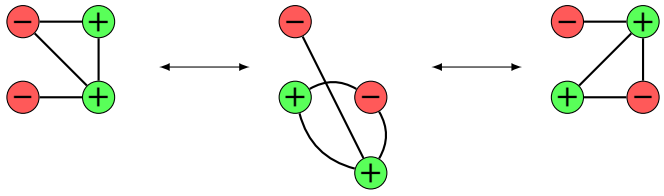

Figure 2.1: Equivalent graphs. Graphs can be deformed to reach all equivalent cases.

– Case 3 ($L_{31} + L_{42} + L_{53} + L_{54}$, see Fig. 2.4). The generator order can be reversed. We show again the schema Fig. 2.3a, the anticommutation graph Fig. 2.3b and the different cases which lead to the corresponding symmetry classes Fig. 2.3c. We write an example Hamiltonian

$$\widehat{\mathcal{H}}(\boldsymbol{k}) = f_1(\boldsymbol{k})\tau_x + f_2(\boldsymbol{k})\tau_x\sigma_x + g_1(\boldsymbol{k})\tau_x\sigma_y + g_2(\boldsymbol{k})\tau_y\sigma_y\,. \tag{2.14}$$

– Case 4 (Two $\mathfrak{su}(2)$ algebras, see Fig. 2.5). The generators split into the direct sum of two distinct $\mathfrak{su}(2)$ algebras. One of the algebras is spanned by L_{ij} and the other one by J_{ij}. We show again the schema Fig. 2.4a, the anticommutation graph Fig. 2.4b and the different cases which lead to the corresponding symmetry classes Fig. 2.4c. For our example we assume the two subalgebras are spanned by the Pauli matrices σ and τ respectively. We write an example Hamiltonian

$$\widehat{\mathcal{H}}(\boldsymbol{k}) = f_1(\boldsymbol{k})\sigma_x + f_2(\boldsymbol{k})\sigma_y + g_1(\boldsymbol{k})\tau_x + g_2(\boldsymbol{k})\tau_y\,. \tag{2.15}$$

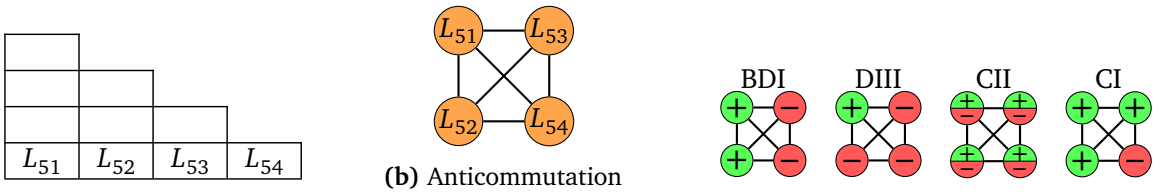

(a) Generators **(b)** Anticommutation graph **(c)** Symmetry classes

Figure 2.2: Case 1 (Four anticommuting generators)

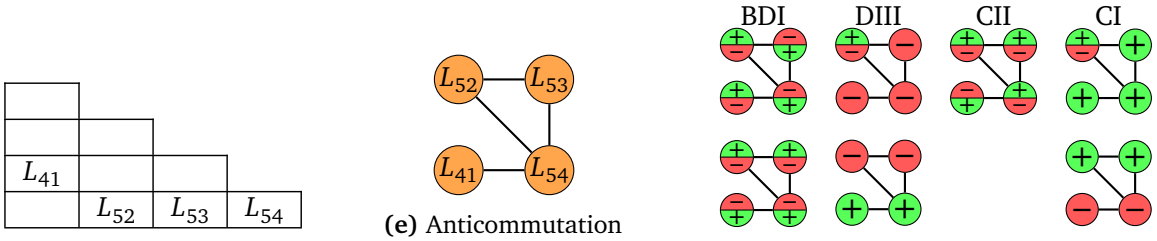

(d) Generators **(e)** Anticommutation graph **(f)** Symmetry classes

Figure 2.3: Case 2 ($L_{41} + L_{52} + L_{53} + L_{54}$)

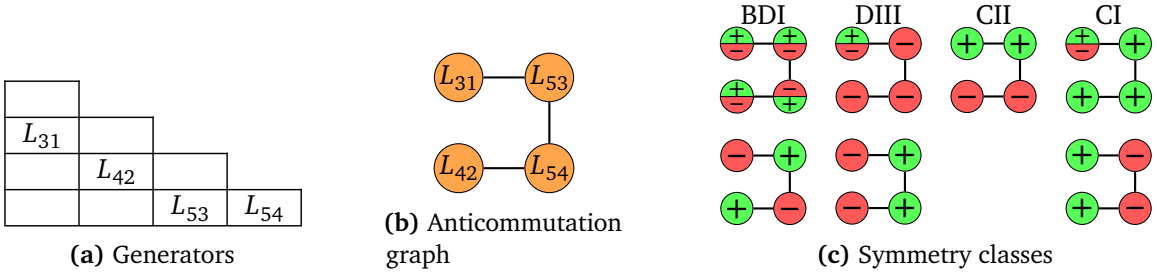

(a) Generators **(b)** Anticommutation graph **(c)** Symmetry classes

Figure 2.4: Case 3 ($L_{31} + L_{42} + L_{53} + L_{54}$)

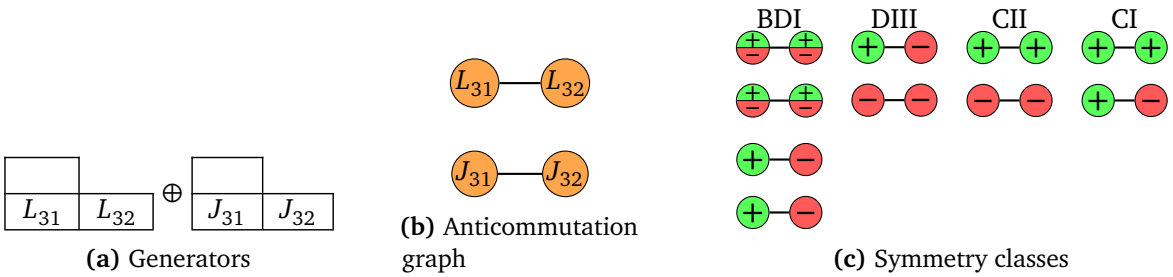

(a) Generators **(b)** Anticommutation graph **(c)** Symmetry classes

Figure 2.5: Case 4 (Two $\mathfrak{su}(2)$ algebras)

Chapter 3

Symmetry classification

One goal of this thesis is the classification of topological systems using symmetries and topological invariants. Symmetries are very fundamental properties of physical systems. In physics we find many examples of symmetries which we distinguish in continuous and discrete symmetries. We can also distinguish between internal (e.g. gauge symmetries) and space time symmetries. Due to Noether's theorem the existence of continuous symmetries is directly connected to a conservation law. The translation invariance of space and time leads to conservation of momentum and energy respectively. In condensed matter or solid state physics we can also study discrete symmetries like space inversion symmetry $\mathcal{I}$, time reversal symmetry $\mathcal{T}$ and charge conjugation symmetry $\mathcal{C}$. In our case we focus on the study of electrons and their band structure in crystals. Crystals show a periodicity in space which breaks the continuous translation symmetry. This leads to the formation of Bravais lattices. The periodicity in space gives rise to Brillouin zones in $\boldsymbol{k}$-space due to the Bloch theorem. Further the continuous rotation symmetry of space is broken to a discrete point group symmetry which describes rotations by certain discrete angles. The combined rotation and translation symmetry can be described by a space group. There exists a exhaustive classification of all space groups and the crystal systems in 2D and 3D. For example in 3D there exist 230 space groups which are combinations of the 32 crystallographic point groups with the 14 Bravais lattices. If you want to cover a volume or a surface always with the same elementary cell, you are restricted to elementary cells which are 2-, 3-, 4- or 6-fold symmetric. This leads to the restriction to 32 crystallographic point groups. However there are quasi crystals which were discovered by D. Shechtman (Nobel prize 2011 in chemistry [25]) which don't belong in this classification. These quasi crystals correspond to two-dimensional Penrose tilings [26, 27].

To describe the band structure of electrons the fundamental physical "object" is the Hamilton operator $\mathcal{H}$. The spectrum of the Hamilton operator corresponds to the set of allowed energies, the eigenvectors of the operator correspond to the states of the electrons. To describe a quantized field we use a many body Hamiltonian in the Bogoliubov-de Gennes (BdG) formalism. At first we study the classification of BdG Hamiltonians using inversion symmetry $\mathcal{I}$, time reversal symmetry $\mathcal{T}$, charge conjugation symmetry $\mathcal{C}$ and point group symmetries.

3.1 BdG formalism

At first we derive basic relations for symmetry transformations in a general BdG Hamiltonian formalism. These relations will be used later throughout this thesis. We assume that a physical system is described by a Hamiltonian $\mathcal{H}$ which operates on a Hilbert space. The Hilbert space is spanned by vectors or state kets $|n\rangle$ where n is a general index including quantum numbers such as wave-vector, spin, orbital etc. An active transformation $\mathcal{O}$ acts on the the state kets as $|n\rangle' = \mathcal{O}|n\rangle$. More precisely an active transformation transforms the state ket $|n\rangle$ while keeping the basis vectors fixed. On the contrary an equivalent passive transformation transforms the basis vectors instead while the state ket $|n\rangle$ stays fixed. Thus passive transformations correspond to a transformation of the operators describing the system. For the given active transformation by $\mathcal{O}$ we can find a passive transformation which acts on the linear

operator $\mathcal{A}$ as follows

$$\langle n|\mathcal{A}'|m\rangle = \langle n|'\,\mathcal{A}\,|m\rangle' = \langle n|\mathcal{O}^\dagger\mathcal{A}\mathcal{O}|m\rangle \implies \mathcal{A}' = \mathcal{O}^\dagger\mathcal{A}\mathcal{O}\,. \tag{3.1}$$

According to Wigner's theorem [28] every symmetry operation acts as a unitary or antiunitary[1] transformation $\mathcal{O}$ in the Hilbert space, therefore we can write $\mathcal{O}^{-1} = \mathcal{O}^\dagger$. A unitary transformation $\mathcal{U}$ leaves the scalar product invariant $\langle n|'\cdot|m\rangle' = \langle n|\mathcal{U}^\dagger\mathcal{U}|m\rangle = \langle n|m\rangle$ whereas an antiunitary transformation $\overline{\mathcal{U}} = \mathcal{U}\mathcal{K}$ leads to a complex conjugation of the scalar product $\langle n|'\cdot|m\rangle' = \langle n|\mathcal{K}^\dagger\mathcal{U}^\dagger\mathcal{U}\mathcal{K}|m\rangle = \langle n|m\rangle^*$. This means that every antiunitary operator can be split into a unitary operator $\mathcal{U}$ and the antiunitary complex conjugation operator $\mathcal{K}$

$$\overline{\mathcal{U}} = \mathcal{U}\mathcal{K} = \mathcal{K}\mathcal{U}^* \tag{3.2}$$

Now we consider a specific form of the Hamiltonian in second quantization. A general Bogoliubov-de Gennes (BdG) Hamiltonian describing a fermionic system is given in the explicit form by

$$\mathcal{H} = \hat{\psi}^\dagger\hat{m}\hat{\psi} + \frac{1}{2}\hat{\psi}^\dagger\hat{\Delta}\left(\hat{\psi}^\dagger\right)^\intercal + \frac{1}{2}\hat{\psi}^\intercal\hat{\Delta}^\dagger\hat{\psi} \tag{3.3}$$

where $\hat{\psi}^\dagger$ ($\hat{\psi}$) are Nambu spinors containing single fermion creation (annihilation) operators for multiple bands (e.g. spin or orbital) respectively. The fermion creation operator $\psi_n^\dagger$ creates the state $|n\rangle = \psi_n^\dagger|0\rangle$ by acting on the vacuum. The Fock space (which is the Hilbert space of the system) is spanned by these basis vectors with proper antisymmetrization e.g. for two fermions $|nm\rangle = |n\rangle\,|m\rangle = |n\rangle\otimes|m\rangle - |m\rangle\otimes|n\rangle$. $\hat{m}$ and $\hat{\Delta}$ are bilinears corresponding to particle-hole and particle-particle terms respectively. Given a unitary transformation $\mathcal{U}$ and its matrix representation $\hat{d}(\mathcal{U})$ with the matrix elements $d_{nm}(\mathcal{U}) = \langle n|\mathcal{U}|m\rangle$ we find the transformation relations of the basis kets $|n\rangle$ and the dual state vectors $\langle n|$ [2]

$$|n\rangle' = \mathcal{U}\,|n\rangle = \sum_m |m\rangle\,\langle m|\mathcal{U}|n\rangle = \sum_m |m\rangle\,d_{mn}(\mathcal{U})\,, \tag{3.4}$$

$$\langle n|' = \langle n|\,\mathcal{U}^\dagger = \sum_m \langle n|\mathcal{U}^\dagger|m\rangle\,\langle m| = \sum_m d_{nm}(\mathcal{U}^\dagger)\,\langle m|\,. \tag{3.5}$$

Using the fundamental relation of the sesquilinear form

$$\langle n|\mathcal{U}^\dagger|m\rangle = \langle m|\mathcal{U}|n\rangle^* \implies d_{nm}(\mathcal{U}^\dagger) = d^*_{mn}(\mathcal{U}) = d^\dagger_{nm}(\mathcal{U}) \tag{3.6}$$

we find the transformations of the bilinears by acting on state vectors

$$\left\langle n\,\middle|\,\hat{\psi}^\dagger\hat{m}'\hat{\psi}\,\middle|\,m\right\rangle = \langle n|'\,\hat{\psi}^\dagger\hat{m}\hat{\psi}\,|m\rangle' = \sum_{ij} d_{ni}(\mathcal{U}^\dagger)m_{ij}d_{jm}(\mathcal{U})$$

$$\implies \hat{m}' = \hat{d}^\dagger(\mathcal{U})\hat{m}\hat{d}(\mathcal{U})\,, \tag{3.7}$$

$$\left\langle nm\,\middle|\,\hat{\psi}^\dagger\hat{\Delta}'\left(\hat{\psi}^\dagger\right)^\intercal\,\middle|\,0\right\rangle = \langle nm|'\,\hat{\psi}^\dagger\hat{\Delta}\left(\hat{\psi}^\dagger\right)^\intercal|0\rangle = \sum_{ij} d_{ni}(\mathcal{U}^\dagger)d_{mj}(\mathcal{U}^\dagger)\Delta_{ij}$$

$$\implies \hat{\Delta}' = \hat{d}^\dagger(\mathcal{U})\hat{\Delta}\hat{d}^*(\mathcal{U})\,. \tag{3.8}$$

For further analysis we want to treat particle-particle and particle-hole terms on the same footing. This is done by introducing the enlarged Nambu spinor $\hat{\chi}^\dagger = \begin{pmatrix}\hat{\psi}^\dagger & \hat{\psi}^\intercal\end{pmatrix}$ where we use the Pauli matrices $\{\mathbb{1}_\tau, \tau_x, \tau_y, \tau_z\}$ as a basis for the particle-hole space. The spinor components are not independent since the relation $\hat{\chi}^\dagger = \hat{\chi}^\intercal\tau_x$ holds, where the transposition acts on both τ and band spaces. The enlarged spinor is not fermionic any more, but Majorana since $\{\chi_n, \chi_m\}$ is non-zero for some n and m. If we

[1] antilinear unitary

[2] The $\langle n|$ belongs to the dual space. The dual space of a Hilbert space is isomorphic to the Hilbert space due to Riesz.

would treat the components of the spinor as independent fields the spinor would still be fermionic. Using the fermionic anticommutation rules we can rewrite the BdG Hamiltonian as follows

$$\mathcal{H} = \frac{1}{2}\hat{\chi}^\dagger \begin{pmatrix} \hat{m} & \hat{\Delta} \\ \hat{\Delta}^\dagger & -\hat{m}^\intercal \end{pmatrix} \hat{\chi} + \frac{1}{2}\operatorname{Tr}\hat{m} \equiv \frac{1}{2}\hat{\chi}^\dagger \widehat{\mathcal{H}} \hat{\chi} + \frac{1}{2}\operatorname{Tr}\hat{m} \tag{3.9}$$

with the BdG Hamiltonian matrix $\widehat{\mathcal{H}}$. The last term is a constant shift of energy which can be omitted for the further analysis. We observe that the spinor relation constraints the form of the BdG Hamiltonian. The form of the BdG Hamiltonian is restricted by the relations $\hat{\Delta} = -\hat{\Delta}^\intercal$ and $\widehat{\mathcal{H}} = -\tau_x \widehat{\mathcal{H}}^\intercal \tau_x$. The Hamiltonian $\widehat{\mathcal{H}}$ transforms under $\mathcal{U}$ as follows

$$\widehat{\mathcal{H}}' = \mathcal{U}^\dagger \widehat{D}\mathcal{U} = \widehat{D}^\dagger(\mathcal{U})\widehat{\mathcal{H}}\widehat{D}(\mathcal{U}), \tag{3.10}$$

$$\widehat{D}(\mathcal{U}) = \begin{pmatrix} \hat{d}(\mathcal{U}) & 0 \\ 0 & \hat{d}^*(\mathcal{U}) \end{pmatrix} = \mathbb{1}_\tau \frac{\hat{d}(\mathcal{U}) + \hat{d}^*(\mathcal{U})}{2} + \tau_z \frac{\hat{d}\ (\mathcal{U}) - \hat{d}^*(\mathcal{U})}{2} \tag{3.11}$$

where $\widehat{D}(\mathcal{U})$ is the matrix representation of $\mathcal{U}$ in combined particle-hole and band space. Respectively for an antiunitary operator $\overline{\mathcal{U}} = \mathcal{U}\mathcal{K}$ we find

$$\widehat{\mathcal{H}}' = \overline{\mathcal{U}}^\dagger \widehat{D}\overline{\mathcal{U}} = \mathcal{K}^\dagger \widehat{D}^\dagger(\mathcal{U})\widehat{\mathcal{H}}\widehat{D}(\mathcal{U})\mathcal{K} = D^\intercal(\mathcal{U})\widehat{\mathcal{H}}^* D^*(\mathcal{U}). \tag{3.12}$$

Now we consider that the single fermion creation operators have the index $\boldsymbol{k}$ for momentum. This leads to the many-body Hamiltonian

$$\mathcal{H} = \frac{1}{2}\sum_{\boldsymbol{k}} \hat{\chi}_{\boldsymbol{k}}^\dagger \begin{pmatrix} \hat{m}(\boldsymbol{k}) & \hat{\Delta}(\boldsymbol{k}) \\ \hat{\Delta}^\dagger(\boldsymbol{k}) & -\hat{m}^\intercal(-\boldsymbol{k}) \end{pmatrix} \hat{\chi}_{\boldsymbol{k}} + \frac{1}{2}\sum_{\boldsymbol{k}} \operatorname{Tr}\hat{m}(\boldsymbol{k}) \equiv \frac{1}{2}\sum_{\boldsymbol{k}} \hat{\chi}_{\boldsymbol{k}}^\dagger \widehat{\mathcal{H}}(\boldsymbol{k}) \hat{\chi}_{\boldsymbol{k}} + \frac{1}{2}\sum_{\boldsymbol{k}} \operatorname{Tr}\hat{m}(\boldsymbol{k}) \tag{3.13}$$

with the spinor $\hat{\chi}_{\boldsymbol{k}}^\dagger = \begin{pmatrix} \hat{\psi}_{\boldsymbol{k}}^\dagger & \hat{\psi}_{-\boldsymbol{k}}^\intercal \end{pmatrix}$. The spinor satisfies the relation $\hat{\chi}_{-\boldsymbol{k}}^\dagger = \hat{\chi}_{\boldsymbol{k}}^\intercal \tau_x$. As before the spinor redundancy constraints the BdG Hamiltonian with the equations $\hat{\Delta}(\boldsymbol{k}) = -\hat{\Delta}^\intercal(-\boldsymbol{k})$ and

$$-\widehat{\mathcal{H}}(\boldsymbol{k}) = \tau_x \widehat{\mathcal{H}}^\intercal(-\boldsymbol{k})\tau_x. \tag{3.14}$$

Relation Eq. (3.14) is actually very important since it corresponds to the existence of the generalized charge conjugation symmetry $\Xi = \tau_x \mathcal{K}$. This means that our BdG Hamiltonian falls into a BdG or BDI symmetry class with $\Xi^2 = 1$. See Section 2.2 for more details on the symmetry classes.

To see how the many-body Hamiltonian transforms under a symmetry operation $\mathcal{U}$ we consider at first the wave function $\phi(\boldsymbol{k}) = \delta(\boldsymbol{k} - \boldsymbol{k}_0)$ of a particle with momentum $\boldsymbol{k}_0$. A transformation of the state gives $\phi'(\boldsymbol{k}) = \mathcal{U}\phi(\boldsymbol{k}) = \phi(\mathcal{U}^\dagger \boldsymbol{k})$ from which we derive

$$\int d\boldsymbol{k}\ \phi'^*(\boldsymbol{k})\mathcal{H}(\boldsymbol{k})\phi'(\boldsymbol{k}) = \int d\boldsymbol{k}\ \phi^*(\mathcal{U}^\dagger\boldsymbol{k})\mathcal{H}(\boldsymbol{k})\phi(\mathcal{U}^\dagger\boldsymbol{k}) = \int d\boldsymbol{k}\ \phi^*(\boldsymbol{k})\mathcal{H}(\mathcal{U}\boldsymbol{k})\phi(\boldsymbol{k}) \tag{3.15}$$

$$\implies \mathcal{H}'(\boldsymbol{k}) = \mathcal{U}^\dagger \mathcal{H}(\boldsymbol{k})\mathcal{U} = \mathcal{H}(\mathcal{U}\boldsymbol{k}). \tag{3.16}$$

Similarly in quantized field theory we transform $|\boldsymbol{k}_0\rangle' = \mathcal{U}|\boldsymbol{k}_0\rangle = |\mathcal{U}\boldsymbol{k}_0\rangle$ and derive

$$\begin{aligned} &\left\langle 0 \middle| c_{\mathcal{U}\boldsymbol{k}_0} \left[\sum_{\boldsymbol{k}} c_{\boldsymbol{k}}^\dagger \mathcal{H}(\boldsymbol{k}) c_{\boldsymbol{k}}\right] c_{\mathcal{U}\boldsymbol{k}_0}^\dagger \middle| 0 \right\rangle = \left\langle 0 \middle| c_{\mathcal{U}\boldsymbol{k}_0} c_{\mathcal{U}\boldsymbol{k}_0}^\dagger \mathcal{H}(\mathcal{U}\boldsymbol{k}_0) c_{\mathcal{U}\boldsymbol{k}_0} c_{\mathcal{U}\boldsymbol{k}_0}^\dagger \middle| 0 \right\rangle = \\ &\left\langle 0 \middle| c_{\boldsymbol{k}_0} \left[\sum_{\boldsymbol{k}} c_{\boldsymbol{k}}^\dagger \mathcal{H}(\mathcal{U}\boldsymbol{k}) c_{\boldsymbol{k}}\right] c_{\boldsymbol{k}_0}^\dagger \middle| 0 \right\rangle = \left\langle 0 \middle| c_{\boldsymbol{k}_0} c_{\boldsymbol{k}_0}^\dagger \mathcal{H}(\mathcal{U}\boldsymbol{k}_0) c_{\boldsymbol{k}_0} c_{\boldsymbol{k}_0}^\dagger \middle| 0 \right\rangle \end{aligned} \tag{3.17}$$

$$\implies \mathcal{H}'(\boldsymbol{k}) = \mathcal{U}^\dagger \mathcal{H}(\boldsymbol{k})\mathcal{U} = \mathcal{H}(\mathcal{U}\boldsymbol{k}). \tag{3.18}$$

We see that the wave function picture and the quantum field picture are consistent. We write down the transformation of the BdG Hamiltonian

$$\widehat{\mathcal{H}}(\boldsymbol{k})' = \mathcal{U}^\dagger \widehat{\mathcal{H}}(\boldsymbol{k})\mathcal{U} = \widehat{D}^\dagger(\mathcal{U})\widehat{\mathcal{H}}(\mathcal{U}\boldsymbol{k})\widehat{D}(\mathcal{U}) \tag{3.19}$$

with the matrix representation $\widehat{D}(\mathcal{U})$ in combined particle-hole and band space. Respectively for an antiunitary operator $\overline{\mathcal{U}} = \mathcal{U}\mathcal{K}$ we find

$$\widehat{\mathcal{H}}(\boldsymbol{k})' = \overline{\mathcal{U}}^{\dagger}\widehat{\mathcal{H}}(\boldsymbol{k})\overline{\mathcal{U}} = \widehat{D}^{\intercal}(\mathcal{U})\widehat{\mathcal{H}}^{*}(-\mathcal{U}\boldsymbol{k})\widehat{D}^{*}(\mathcal{U})\,. \tag{3.20}$$

After we have written the action of general symmetry transformations $\mathcal{O} = \mathcal{U}, \overline{\mathcal{U}}$ we consider specific discrete transformations.

3.2 Inversion, time reversal and charge conjugation transformation

In this section we find explicit expressions for the action of inversion $\mathcal{I}$, time reversal transformation $\mathcal{T}$ and charge conjugation $\mathcal{C}$ on a BdG Hamiltonian. Application of these discrete transformations can either leave physical systems invariant or not. When the system is left invariant we call the system to be symmetric or invariant under the transformation and we call the transformation a symmetry instead, for example inversion symmetry $\mathcal{I}$. After we found the explicit forms of the transformations we can use them to perform symmetry classification of order parameters.

3.2.1 Inversion transformation $\mathcal{I}$

Inversion transformation is a unitary operation defined by the following actions on the position operator $\hat{\boldsymbol{r}}$, the momentum operator $\hat{\boldsymbol{p}}$ and the spin operator $\widehat{\boldsymbol{S}}$

$$\mathcal{I}^{\dagger}\,\hat{\boldsymbol{r}}\,\mathcal{I} = -\hat{\boldsymbol{r}}\,, \quad \mathcal{I}^{\dagger}\,\hat{\boldsymbol{p}}\,\mathcal{I} = -\hat{\boldsymbol{p}}\,, \quad \mathcal{I}^{\dagger}\,\hat{\boldsymbol{r}}\times\hat{\boldsymbol{p}}\,\mathcal{I} = +\hat{\boldsymbol{r}}\times\hat{\boldsymbol{p}}\,, \quad \mathcal{I}^{\dagger}\,\widehat{\boldsymbol{S}}\,\mathcal{I} = +\widehat{\boldsymbol{S}}\,. \tag{3.21}$$

Assume we have a single particle state $|\boldsymbol{k},\sigma,\nu\rangle$, with wave vector $\boldsymbol{k}$, spin σ (eigenvalue of the operator $\widehat{S}_z$) and an orbital quantum number ν, we get

$$\mathcal{I}\,|\boldsymbol{k},\sigma,\nu\rangle = \eta_{\nu}\,|-\boldsymbol{k},\sigma,\nu\rangle \tag{3.22}$$

where $\eta_{\nu} = \langle\boldsymbol{k},\sigma,\nu|\mathcal{I}|\boldsymbol{k},\sigma,\nu\rangle$ is the intrinsic parity of the orbital. Since inversion squares to one the parity of an orbital can be either odd (-1) or even $(+1)$. In combined spin and orbital spaces the matrix representation is given by the diagonal matrix $\hat{d}(\mathcal{I}) = \hat{\eta}$. We obtain further the representation in combined particle-hole and band space

$$\widehat{D}(\mathcal{I}) = \mathbb{1}_{\tau}\,\frac{\hat{d}(\mathcal{I}) + \hat{d}^{*}(\mathcal{I})}{2} + \tau_{z}\,\frac{\hat{d}(\mathcal{I}) - \hat{d}^{*}(\mathcal{I})}{2} = \hat{\eta}\,. \tag{3.23}$$

As a result the BdG Hamiltonian transforms in the following way

$$\widehat{\mathcal{H}}(\boldsymbol{k})' = \mathcal{I}^{\dagger}\widehat{\mathcal{H}}(\boldsymbol{k})\mathcal{I} = \hat{\eta}\,\widehat{\mathcal{H}}(-\boldsymbol{k})\hat{\eta}\,. \tag{3.24}$$

At this point we recall that the BdG Hamiltonian satisfies Eq. (3.14) providing us one more expression for the transformation of the BdG Hamiltonian under inversion

$$\widehat{\mathcal{H}}(\boldsymbol{k})' = \mathcal{I}^{\dagger}\widehat{\mathcal{H}}(\boldsymbol{k})\mathcal{I} = -\tau_x\hat{\eta}\,\widehat{\mathcal{H}}^{\intercal}(\boldsymbol{k})\tau_x\hat{\eta}\,. \tag{3.25}$$

Restriction to a single orbital reduces $\hat{\eta} = \eta$ to a scalar matrix and the transformation of the Hamiltonian to

$$\widehat{\mathcal{H}}(\boldsymbol{k})' = \mathcal{I}^{\dagger}\widehat{\mathcal{H}}(\boldsymbol{k})\mathcal{I} = \widehat{\mathcal{H}}(-\boldsymbol{k}) = -\tau_x\widehat{\mathcal{H}}^{\intercal}(\boldsymbol{k})\tau_x\,. \tag{3.26}$$

3.2.2 Time reversal transformation $\mathcal{T}$

Time reversal transformation is an antiunitary transformation which is defined by the following actions

$$\mathcal{T}^\dagger\,\hat{\boldsymbol{r}}\,\mathcal{T}=+\hat{\boldsymbol{r}}\,,\quad \mathcal{T}^\dagger\,\hat{\boldsymbol{p}}\,\mathcal{T}=-\hat{\boldsymbol{p}}\,,\quad \mathcal{T}^\dagger\,\hat{\boldsymbol{r}}\times\hat{\boldsymbol{p}}\,\mathcal{T}=-\hat{\boldsymbol{r}}\times\hat{\boldsymbol{p}}\,,\quad \mathcal{T}^\dagger\,\widehat{\boldsymbol{S}}\,\mathcal{T}=-\widehat{\boldsymbol{S}}\,. \tag{3.27}$$

Since $\mathcal{T}$ is antiunitary we may write it as the product of a unitary time reversal operator $\mathcal{T}_U$ and the antiunitary complex conjugation operator $\mathcal{K}$ that acts on complex numbers and reverses momentum. For the usual representation of the spin operators with $\widehat{S}_y$ imaginary we find the following actions of the complex conjugation operator

$$\mathcal{K}^\dagger\,\hat{\boldsymbol{r}}\,\mathcal{K}=+\hat{\boldsymbol{r}}\,,\quad \mathcal{K}^\dagger\,\hat{\boldsymbol{p}}\,\mathcal{K}=-\hat{\boldsymbol{p}}\,,\quad \mathcal{K}^\dagger\,\widehat{S}_{x,z}\,\mathcal{K}=+\widehat{S}_{x,z}\,,\quad \mathcal{K}^\dagger\,\widehat{S}_y\,\mathcal{K}=-\widehat{S}_y\,. \tag{3.28}$$

Since $\mathcal{T}=\mathcal{T}_U\mathcal{K}$ the actions of the operator $\mathcal{T}_U$ are fixed as

$$\mathcal{T}_U^\dagger\,\hat{\boldsymbol{r}}\,\mathcal{T}_U=+\hat{\boldsymbol{r}}\,,\quad \mathcal{T}_U^\dagger\,\hat{\boldsymbol{p}}\,\mathcal{T}_U=+\hat{\boldsymbol{p}}\,,\quad \mathcal{T}_U^\dagger\,\widehat{S}_{x,z}\,\mathcal{T}_U=-\widehat{S}_{x,z}\,,\quad \mathcal{T}_U^\dagger\,\widehat{S}_y\,\mathcal{T}_U=+\widehat{S}_y\,. \tag{3.29}$$

For $\mathcal{T}_U=e^{-i\pi\widehat{S}_y/\hbar}$ the above relations are satisfied and we obtain $\mathcal{T}=e^{-i\pi\widehat{S}_y/\hbar}\mathcal{K}$. For a spin-1/2 we have $\widehat{S}_y=\hbar\sigma_y/2$ providing $\mathcal{T}=-i\sigma_y\mathcal{K}$. For a single particle state $|\boldsymbol{k},\sigma,\nu\rangle$ with orbital ν we also have to consider the action of time reversal on the orbital ν and obtain

$$\mathcal{T}=\mathcal{T}_U\mathcal{K}=e^{-i\pi\widehat{S}_y/\hbar}e^{-i\pi\widehat{L}_y/\hbar}\mathcal{K}=e^{-i\pi\widehat{J}_y/\hbar}\mathcal{K}\,, \tag{3.30}$$

with the angular momentum operator $\widehat{L}_y$ and the total angular momentum operator $\widehat{J}_y=\widehat{L}_y+\widehat{S}_y$. Since the representation $\hat{d}(\mathcal{T})$ is real we obtain

$$\widehat{D}(\mathcal{T})=\mathbb{1}_\tau\,\frac{\hat{d}(\mathcal{T})+\hat{d}^*(\mathcal{T})}{2}+\tau_z\,\frac{\hat{d}(\mathcal{T})-\hat{d}^*(\mathcal{T})}{2}=e^{-i\pi\widehat{J}_y/\hbar}\,. \tag{3.31}$$

Finally we retrieve the BdG Hamiltonian transformation

$$\widehat{\mathcal{H}}(\boldsymbol{k})'=\mathcal{T}^\dagger\widehat{\mathcal{H}}(\boldsymbol{k})\mathcal{T}=\mathcal{K}^\dagger e^{+i\pi\widehat{J}_y/\hbar}\widehat{\mathcal{H}}(\boldsymbol{k})e^{-i\pi\widehat{J}_y/\hbar}\mathcal{K}=e^{+i\pi\widehat{J}_y/\hbar}\widehat{\mathcal{H}}^*(-\boldsymbol{k})e^{-i\pi\widehat{J}_y/\hbar}\,. \tag{3.32}$$

Due to the property Eq. (3.14) of the BdG Hamiltonian we get

$$\widehat{\mathcal{H}}(\boldsymbol{k})'=\mathcal{T}^\dagger\widehat{\mathcal{H}}(\boldsymbol{k})\mathcal{T}=-\tau_x e^{+i\pi\widehat{J}_y/\hbar}\widehat{\mathcal{H}}(\boldsymbol{k})\tau_x e^{-i\pi\widehat{J}_y/\hbar}\,. \tag{3.33}$$

3.2.3 Charge conjugation $\mathcal{C}$

The BdG Hamiltonian permits to introduce a charge conjugation transformation. We can define it to be either unitary or antiunitary in the way it acts on the BdG Hamiltonian. In relativistic field theories charge conjugation is fixed to be antiunitary since CPT = 1. This is due to the CPT theorem and the fact that time reversal is antiunitary. Notice that inversion transformation is the same as parity transformation in 3D (However parity is not the same as inversion in 2D).

Let us at first consider a unitary charge conjugation $\mathcal{C}$ which we define by the action on the spinor as

$$\mathcal{C}\,\hat{\psi}_{\boldsymbol{k}}^\dagger\,\mathcal{C}^\dagger=\hat{\psi}_{-\boldsymbol{k}}^\intercal\quad\Longrightarrow\quad \mathcal{C}\,\hat{\chi}_{\boldsymbol{k}}^\dagger\,\mathcal{C}^\dagger=\mathcal{C}\begin{pmatrix}\hat{\psi}_{\boldsymbol{k}}^\dagger & \hat{\psi}_{-\boldsymbol{k}}^\intercal\end{pmatrix}\mathcal{C}^\dagger=\begin{pmatrix}\hat{\psi}_{-\boldsymbol{k}}^\intercal & \hat{\psi}_{\boldsymbol{k}}^\dagger\end{pmatrix}=\hat{\chi}_{\boldsymbol{k}}^\dagger\tau_x\,. \tag{3.34}$$

We obtain the matrix representation $\widehat{D}(\mathcal{C})=\tau_x$ and the transformation of the BdG Hamiltonian

$$\widehat{\mathcal{H}}(\boldsymbol{k})'=\mathcal{C}^\dagger\widehat{\mathcal{H}}(\boldsymbol{k})\mathcal{C}=\tau_x\widehat{\mathcal{H}}(\boldsymbol{k})\tau_x\,. \tag{3.35}$$

Due to the property Eq. (3.14) of the BdG Hamiltonian we get

$$\widehat{\mathcal{H}}(\boldsymbol{k})'=\mathcal{C}^\dagger\widehat{\mathcal{H}}(\boldsymbol{k})\mathcal{C}=-\mathcal{K}^\dagger\widehat{\mathcal{H}}(\boldsymbol{k})\mathcal{K}\,. \tag{3.36}$$

For antiunitary charge conjugation $\overline{\mathcal{C}}=\mathcal{C}\mathcal{K}$ we see immediately that

$$\widehat{\mathcal{H}}(\boldsymbol{k})'=\overline{\mathcal{C}}^\dagger\widehat{\mathcal{H}}(\boldsymbol{k})\overline{\mathcal{C}}=-\widehat{\mathcal{H}}(\boldsymbol{k}) \tag{3.37}$$

which fixes the behavior of the Hamiltonian under charge conjugation to give a -1. This corresponds to the existence of a generalized charge conjugation symmetry $\Xi=\overline{\mathcal{C}}=\tau_x\mathcal{K}$ (see Eq. (3.14) and Section 2.2).

3.3 Point group symmetry

A point group $\mathcal{G}$ is a finite group which operates on the real or momentum space with reflections and rotations. Space groups are more general and also include translations in space. Thus a point group forms a subgroup of a space group. We need space groups if we want to describe tight binding models which exhibit a periodicity in space effectively breaking the continuous translation symmetry to a discrete translation symmetry. However for continuum models the translation symmetry is unbroken and the study of the point group suffices. Due to the crystallographic restriction theorem the crystal point groups are restricted to 2-, 3-, 4- or 6-fold rotations. Thus there are only 32 crystallographic point groups. See Table 3.1 for an overview. For now we only want to discuss some general ideas about point groups. Later when we discuss systems with a 4-fold rotation symmetry we study the operation of a point group in detail.

Let's sum up some basic facts about groups. Assuming that we have a finite group $\mathcal{G}$ with the elements $\mathcal{G}_i$ ($i = 0, \ldots, n-1$, $\mathcal{G}_0 \equiv$ identity element). Then we can multiply two elements $\mathcal{G}_i$ and $\mathcal{G}_j$ so that $\mathcal{G}_i \cdot \mathcal{G}_j \in \mathcal{G}$. Additionally there must be a inverse element to each group element giving $\mathcal{G}_0 = \mathcal{G}_i \cdot \mathcal{G}_i^{-1}$. Now point group operations act on the BdG Hamiltonian as follows

$$\widehat{\mathcal{H}}(\boldsymbol{k})' = \mathcal{G}_i^\dagger \widehat{\mathcal{H}}(\boldsymbol{k})\mathcal{G}_i = \widehat{D}^\dagger(\mathcal{G}_i)\widehat{\mathcal{H}}(\mathcal{G}_i\boldsymbol{k})\widehat{D}(\mathcal{G}_i) \tag{3.38}$$

where the action on the vector $\boldsymbol{k}$ is especially important. The matrix representations $\widehat{D}(\mathcal{G}_i)$ are non-trivial for example if the system exhibits strong spin orbit coupling thus rotations affecting spin. This might not be case if we have a strong magnetic field which fixes the spin direction.

Table 3.1: Crystallographic point groups in Schoenflies notation. C_n are the cyclic groups. C_{nh} contains C_n and adds a reflection plane perpendicular to the rotation axis. C_{nv} contains C_n and adds reflection planes parallel to the rotation axis. D_n are the dihedral groups. S_{2n} (German "Spiegel") contain only a $2n$-fold rotation-reflection axis. The gray cells indicate duplicates, the red cells forbidden groups because they contain higher rotations (8- and 12-fold) which are forbidden by the crystallographic restriction theorem. Missing in the table are the tetrahedral and octohedral groups T, T_d, T_h, O and O_h. Counting all the groups yields 32 crystallographic point groups in total.

n	1	2	3	4	6
C_n	C_1	C_2	C_3	C_4	C_6
C_{nv}	$C_{1v} = C_{1h}$	C_{2v}	C_{3v}	C_{4v}	C_{6v}
C_{nh}	C_{1h}	C_{2h}	C_{3h}	C_{4h}	C_{6h}
D_n	$D_1 = C_2$	D_2	D_3	D_4	D_6
D_{nh}	$D_{1h} = C_{2v}$	D_{2h}	D_{3h}	D_{4h}	D_{6h}
D_{nd}	$D_{1d} = C_{2h}$	D_{2d}	D_{3d}	D_{4d}	D_{6d}
S_{2n}	S_2	S_4	S_6	S_8	S_{12}

Table 3.2: Character table of the dihedral point group D_{4h} which consists of rotations and reflections. See Fig. 4.2a for a visualization.

I.R.	E	$2C_4$	C_2	$2C_2'$	$2C_2''$	$\mathcal{I}$	$2S_4$	σ_h	$2\sigma_v$	$2\sigma_d$	Linear, Rotations	Higher functions
A_{1g}	+1	+1	+1	+1	+1	+1	+1	+1	+1	+1		x^2+y^2, z^2
A_{2g}	+1	+1	+1	−1	−1	+1	+1	+1	−1	−1	R_z	$xy(x^2-y^2)$
B_{1g}	+1	−1	+1	+1	−1	+1	−1	+1	+1	−1		x^2-y^2
B_{2g}	+1	−1	+1	−1	+1	+1	−1	+1	−1	+1		xy
E_g	+2	0	−2	0	0	+2	0	−2	0	0	(R_x, R_y)	(xz, yz)
A_{1u}	+1	+1	+1	+1	+1	−1	−1	−1	−1	−1		$xyz(x^2-y^2)$
A_{2u}	+1	+1	+1	−1	−1	−1	−1	−1	+1	+1	z	
B_{1u}	+1	−1	+1	+1	−1	−1	+1	−1	−1	+1		xyz
B_{2u}	+1	−1	+1	−1	+1	−1	+1	−1	+1	−1		$z(x^2-y^2)$
E_u	+2	0	−2	0	0	−2	0	+2	0	0	(x, y)	

3.3.1 Representations and character tables

The most important tool for the analysis of point groups is the character table which summarizes the essential properties of the irreducible representations (I.R.) $\widehat{D}_i$ of the point group. A representation $\widehat{D}_i$ is a mapping from the group elements to invertible matrices of some dimensionality. The representation of a group element $\mathcal{G}_n$ is a matrix $\widehat{D}_i(\mathcal{G}_n)$. In the simplest case these "matrices" are just numbers giving a one-dimensional representation. The defining property of a representation is that it is a group homomorphism, which essentially means that we can pull out the group multiplication $\widehat{D}_i(\mathcal{G}_n \cdot \mathcal{G}_m) = \widehat{D}_i(\mathcal{G}_n) \cdot \widehat{D}_i(\mathcal{G}_m)$. The interesting thing about representations is that all of them can be built up from irreducible representations. Two irreducible representations can be combined using a direct sum to form a new higher dimensional reducible representation as follows $\widehat{D} = \widehat{D}_i \oplus \widehat{D}_j$. Now for the irreducible representations of the elements one can define characters which are just traces of the matrices $\chi_i(\mathcal{G}_n) = \mathrm{Tr}\,\widehat{D}_i(\mathcal{G}_n)$. These characters are summarized in a so called character table of a point group. It can be shown that group elements fall into conjugacy classes which give the same character. See Section 3.3.2 for an explanation of conjugacy classes and for the construction of a character table.

At this point we mention the irreducible representations of the D_{4h} and explain its character table Table 3.2 since we will use this later. The first column contains the name of the irreducible representation (I.R.). In the usual nomenclature A and B are used for one-dimensional and E for two-dimensional representations. The subscript g or u means "gerade" (even in German) or "ungerade" (odd in German) which describes the behavior of the representation under inversion $\mathcal{I}$. The symbols A_{1g} etc. which are used as names for the irreducible representations are called Mullikan symbols. The last two columns list example basis functions which transform under the given transformation. For example the row A_{1g} contains the trivial representation with $D_{A_{1g}}(\mathcal{G}_i) = \chi_{A_{1g}}(\mathcal{G}_i) = 1$. Therefore transformation under the trivial representation is just a multiplication by 1. The function x^2+y^2 doesn't change under 4-fold rotation around the z-axis. Therefore the function x^2+y^2 belongs to the A_{1g} representation of the group D_{4h}. The column with the linear basis functions also contains rotations R_x, R_y, R_z around the x-, y- and z-axis respectively. For a rotation you have to consider the direction of the axis and the rotation direction which is per definition counter clockwise. Let's take a look at the operation σ_h which is a reflection at the xy plane and the rotations R_x and R_z. The reflection inverts the direction of R_z and makes the rotation clockwise. Compared to that the direction of R_x is unchanged but the rotation direction is also changed to clockwise. So to summarize, R_z doesn't change under σ_h while R_x acquires a -1.

3.3.2 The great orthogonality theorem

We want to cite a very important mathematical theorem called the **great orthogonality theorem** which is used to construct character tables. This section is based on [29]. For a group element $h \in \mathcal{G}$ we

define the conjugacy class by $\mathcal{G}\cdot h = \left\{ghg^{-1} \mid g \in \mathcal{G}\right\}$. The conjugacy class contains elements which are conjugate to each other. Two elements $a, b \in \mathcal{G}$ are conjugate if we find a $g \in \mathcal{G}$ so that $gag^{-1} = b$. Let $|\mathcal{G}|$ be the group order and d_i the dimension of the i-th irreducible representation $\widehat{D}_i$ (the dimension of the matrices $\widehat{D}_i(g)$ for an $g \in \mathcal{G}$). The **great orthogonality theorem** for group elements $g \in \mathcal{G}$ can then be stated as follows

$$\sum_g \widehat{D}_i(g)_{mn}\widehat{D}_j(g)^*_{m'n''} = \frac{|\mathcal{G}|}{\sqrt{d_i d_j}}\delta_{ij}\delta_{mm'}\delta_{nn'}\,. \tag{3.39}$$

We see that the matrix elements $\widehat{D}_i(g)_{mn}$ behave like a vector of square length $|\mathcal{G}|/d_i$

$$\sum_g \widehat{D}_i(g)_{mn}\widehat{D}_i(g)^*_{mn} = \frac{|\mathcal{G}|}{d_i}\,. \tag{3.40}$$

Vectors from different matrix elements or representations are orthogonal. This gives us five important rules about irreducible representations $\widehat{D}_i$ and their characters $\chi_i(g) = \operatorname{Tr}\widehat{D}_i(g)$ which are the traces of the respective representation matrices of the group elements.

1. $\sum_i d_i^2 = |\mathcal{G}|$
2. $\sum_g \chi_i(g)^2 = |\mathcal{G}|$
3. $\sum_g \chi_i(g)\chi_j(g) = 0$ for $i \neq j \implies \sum_g \chi_i(g)\chi_j(g) = \delta_{ij}h$
4. Characters of representation matrices of group elements which belong to the same class are equal (since the group elements are conjugate).
5. The number of irreducible representations equals the number of conjugacy classes.

To construct a character table we find at first the number of conjugacy classes which equals the number of irreducible representations. We know that every group has a trivial one-dimensional irreducible representation with $D(g) = \chi(g) = 1$. The vectors of characters of other representations have to be orthogonal to the trivial character vector with only ones. Using the above properties we can find all other representations.

3.4 Extending the spinor with a finite group

We assume that we have a finite group $\mathcal{R}$ which affects the wave vectors $\boldsymbol{k}$, e.g. a point group. In this case we can extend the spinor by adding transformed fermion creation operators to the spinor. For example we consider the action of the elements $\mathcal{R}_i$ ($i = 0, \ldots, n-1$, $\mathcal{R}_0 \equiv$ identity element) on the wave vectors $\boldsymbol{k}$. We can then construct the enlarged spinor

$$\widehat{\Psi}^\dagger_{\boldsymbol{k}} = \begin{pmatrix} \hat{\psi}^\dagger_{\boldsymbol{k}} & \hat{\psi}^\dagger_{\mathcal{R}_1\boldsymbol{k}} & \hat{\psi}^\dagger_{\mathcal{R}_2\boldsymbol{k}} & \ldots & \hat{\psi}^\dagger_{\mathcal{R}_{n-1}\boldsymbol{k}} \end{pmatrix}. \tag{3.41}$$

We use a set of ρ matrices as a basis of the new subspace. We find a representation $\hat{d}_\rho(\mathcal{R}_i)$ for the group operation $\mathcal{R}_i$ which acts in ρ space. We already know the action Eq. (3.38) of a group element $\mathcal{R}_i$ on the BdG Hamiltonian. Now we include the $\hat{d}_\rho(\mathcal{R}_i)$ in the representation $\widehat{\mathscr{D}}(\mathcal{R}_i)$ (compared to $\widehat{D}(\mathcal{R}_i)$) and get

$$\mathscr{D}(\mathcal{R}_i) = \begin{pmatrix} \hat{d}(\mathcal{R}_i)\hat{d}_\rho(\mathcal{R}_i) & 0 \\ 0 & \hat{d}^*(\mathcal{R}_i)\hat{d}^*_\rho(\mathcal{R}_i) \end{pmatrix}, \tag{3.42}$$

$$\begin{aligned}\widehat{\mathcal{H}}(\boldsymbol{k})' &= \mathcal{R}_i^\dagger\widehat{\mathcal{H}}(\boldsymbol{k})\mathcal{R}_i = \widehat{D}^\dagger(\mathcal{R}_i)\widehat{\mathcal{H}}(\mathcal{R}_i\boldsymbol{k})\widehat{D}(\mathcal{R}_i) \\ &= \widehat{\mathscr{D}}^\dagger(\mathcal{R}_i)\widehat{\mathcal{H}}(\boldsymbol{k})\widehat{\mathscr{D}}(\mathcal{R}_i)\,.\end{aligned} \tag{3.43}$$

We will use this spinor extension technique for density waves in Chapter 4 to include an additional translation symmetry to the spinor and in Chapter 5 to add three different incommensurate wave-vectors to the spinor.

Chapter 4

Density waves in highly anisotropic materials

In this chapter we perform a symmetry classification of systems showing a strong anisotropy in z-direction. The high anisotropy is realized by different kinetic terms in the xy-plane and the z-direction as for example in

$$\mathcal{H}_{\text{kin}} = \sum_{\boldsymbol{k},\sigma,\sigma'} t_z \cos k_z c^\dagger_{\boldsymbol{k}\sigma} c_{\boldsymbol{k}\sigma'} + \sum_{\boldsymbol{k},\sigma,\sigma'} t(\cos k_x + \cos k_y) c^\dagger_{\boldsymbol{k}\sigma} c_{\boldsymbol{k}\sigma'} \tag{4.1}$$

with $t_z \ll t$. Such highly anisotropic systems can be described as quasi 2D systems. The kinetic term corresponds to nearest neighbor hopping which can be seen by Fourier transformation as in Fig. 4.1a. We focus on the point group D_{4h} which is appropriate to describe such quasi 2D systems. We discuss the point group D_{4h} in detail and a specific symmetry breaking scheme in the next section. After that we focus on the formation of density waves with the commensurate wave vector $\boldsymbol{Q} = (\pi, \pi, \pi)$ due to strong Fermi surface nesting which occurs at half filling. The nesting situation can be seen by inspecting the Fermi surface as in Fig. 4.1b. We perform an exhaustive classification of the density wave and superconductivity order parameters for such a system. During this thesis we also worked on an exhaustive classification for $\boldsymbol{Q} = (\pi, \pi, 0)$ which is shown in Appendix B. In the last section of this chapter we apply the classification methods to a topological system with density waves and determine the topological phases by finding the gap closings in the energy spectrum.

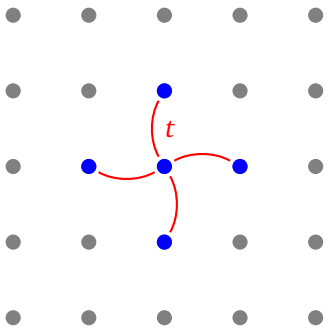

(a) Fourier transformation yields that $\cos k_x + \cos k_y$ corresponds to nearest neighbor hopping in lattice real space.

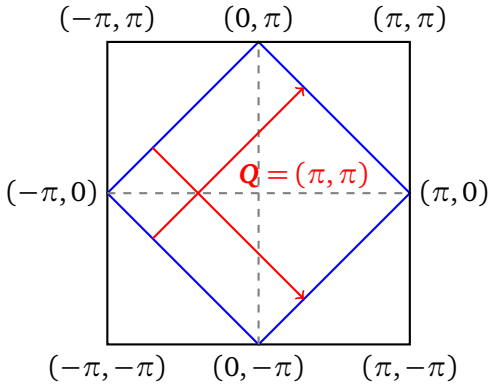

(b) Brillouin zone with $\cos k_x + \cos k_y = 0$ in blue. At half filling the Fermi surface is in the perfect nesting scenario. The commensurate wave vector $\boldsymbol{Q} = (\pi, \pi)$ connects the sides of the Fermi surface.

Figure 4.1: Kinetic term $t(\cos k_x + \cos k_y) c^\dagger_{\boldsymbol{k}} c_{\boldsymbol{k}}$

4.1 Point group D_{4h}

The point group D_{4h} contains proper and improper rotations (rotary reflections). We show the rotation axes and reflection planes of D_{4h} and various subgroups in Fig. 4.2. The subgroups are important when we discuss the symmetry breaking in the next section. From the Fig. 4.2 one sees directly the group – subgroup relations. For example the point C_{4v} emerges from D_{4h} by removing the σ_h reflection plane. For the analysis of the D_{4h} it is useful to mention that the group is equivalent to $D_4 \times \{E, \mathcal{I}\}$ where E is the identity operation and $\mathcal{I}$ is space inversion. Since we already analyzed the inversion operation $\mathcal{I}$ in Chapter 3 we focus here on the point group D_4 which contains only rotation operations. We have to find how spin and angular momentum transform under the elements of D_4. D_4 has 8 elements. The identity E, the fourfold rotations $C_4, C_4^{-1} = \overline{C}_4$ around the z-axis, the twofold $C_2 = C_4^2$ rotation around the z-axis, two twofold rotations C_2' with the vertical axes x, y and two twofold rotations C_2'' with the diagonal axes given by $x = y$ and $x = -y$. At first we write down the transformation of the wave vector under the action of D_4 elements

$$C_4\left(k_x,k_y,k_z\right) = \left(-k_y,k_x,k_z\right), \qquad \overline{C}_4\left(k_x,k_y,k_z\right) = \left(k_y,-k_x,k_z\right), \tag{4.2}$$

$$C_2\left(k_x,k_y,k_z\right) = \left(-k_x,-k_y,k_z\right), \tag{4.3}$$

$$C_{2a}'\left(k_x,k_y,k_z\right) = \left(k_x,-k_y,-k_z\right), \quad C_{2b}'\left(k_x,k_y,k_z\right) = \left(-k_x,k_y,-k_z\right), \tag{4.4}$$

$$C_{2a}''\left(k_x,k_y,k_z\right) = \left(k_y,k_x,-k_z\right), \quad C_{2b}''\left(k_x,k_y,k_z\right) = \left(-k_y,-k_x,-k_z\right). \tag{4.5}$$

The spin and angular momentum transformations are generated by the appropriate rotation generators. We find the following representations

$$\hat{d}_J(C_4) = e^{-i\frac{\pi}{2}\widehat{J}_z/\hbar}, \qquad \hat{d}_J(\overline{C}_4) = e^{+i\frac{\pi}{2}\widehat{J}_z/\hbar}, \tag{4.6}$$

$$\hat{d}_J(C_2) = e^{-i\pi\widehat{J}_z/\hbar}, \tag{4.7}$$

$$\hat{d}_J(C_{2a}') = e^{-i\pi\widehat{J}_x/\hbar}, \qquad \hat{d}_J(C_{2b}') = e^{-i\pi\widehat{J}_y/\hbar}, \tag{4.8}$$

$$\hat{d}_J(C_{2a}'') = e^{-i\pi\left(\widehat{J}_x+\widehat{J}_y\right)/(\sqrt{2}\hbar)}, \quad \hat{d}_J(C_{2b}'') = e^{-i\pi\left(\widehat{J}_x-\widehat{J}_y\right)/(\sqrt{2}\hbar)} \tag{4.9}$$

where we used the total angular momentum operator $\widehat{\boldsymbol{J}}$. For a spin-1/2 we have $\widehat{\boldsymbol{J}} = \widehat{\boldsymbol{S}} = \hbar\boldsymbol{\sigma}/2$ and the above representations become

$$\hat{d}_\sigma(C_4) = \frac{\mathbb{1}_\sigma - i\sigma_z}{\sqrt{2}}, \qquad \hat{d}_\sigma(\overline{C}_4) = \frac{\mathbb{1}_\sigma + i\sigma_z}{\sqrt{2}}, \tag{4.10}$$

$$\hat{d}_\sigma(C_2) = -i\sigma_z, \tag{4.11}$$

$$\hat{d}_\sigma(C_{2a}') = -i\sigma_x, \qquad \hat{d}_\sigma(C_{2b}') = -i\sigma_y, \tag{4.12}$$

$$\hat{d}_\sigma(C_{2a}'') = -i\frac{\sigma_x+\sigma_y}{\sqrt{2}}, \quad \hat{d}_\sigma(C_{2b}'') = -i\frac{\sigma_x-\sigma_y}{\sqrt{2}}. \tag{4.13}$$

Since our spinor lives also in τ space we have to compute the complete representation $\widehat{D}(\mathcal{G})$ of the group operations

$$\widehat{D}(\mathcal{G}) \equiv \begin{pmatrix} \hat{d}(\mathcal{G}) & 0 \\ 0 & \hat{d}^*(\mathcal{G}) \end{pmatrix} = \mathbb{1}_\tau \frac{\hat{d}(\mathcal{G}) + \hat{d}^*(\mathcal{G})}{2} + \tau_z \frac{\hat{d}(\mathcal{G}) - \hat{d}^*(\mathcal{G})}{2}. \tag{4.14}$$

For the sake of completeness we write down the explicit form of the complete representations $\widehat{D}(\mathcal{G})$

$$\widehat{D}(C_4) = \frac{\mathbb{1} - i\tau_z\sigma_z}{\sqrt{2}}, \qquad \widehat{D}(\overline{C}_4) = \frac{\mathbb{1} + i\tau_z\sigma_z}{\sqrt{2}}, \tag{4.15}$$

$$\widehat{D}(C_2) = -i\tau_z\sigma_z, \tag{4.16}$$

$$\widehat{D}(C_{2a}') = -i\tau_z\sigma_x, \qquad \widehat{D}(C_{2b}') = -i\sigma_y, \tag{4.17}$$

$$\widehat{D}(C_{2a}'') = -i\frac{\tau_z\sigma_x+\sigma_y}{\sqrt{2}}, \quad \widehat{D}(C_{2b}'') = -i\frac{\tau_z\sigma_x-\sigma_y}{\sqrt{2}}. \tag{4.18}$$

Now let's remember that the BdG Hamiltonian transforms as follows

$$\widehat{\mathcal{H}}(\boldsymbol{k})' = \mathcal{G}^\dagger \widehat{\mathcal{H}}(\boldsymbol{k})\mathcal{G} = \widehat{D}^\dagger(\mathcal{G})\widehat{\mathcal{H}}(\mathcal{G}\boldsymbol{k})\widehat{D}(\mathcal{G})\,. \tag{4.19}$$

This transformation rule of the BdG Hamiltonian will be used in the classification of the order parameters in Section 4.3. We will identify the representations the order parameters belong to.

4.2 Point group symmetry breaking

Now we discuss a symmetry breaking scheme of the point groups. A Hamiltonian consists of a sum of terms with each term transforming under a one-dimensional representations of a point group. In our case we discuss the point group $\mathrm{D}_{4\mathrm{h}}$. If we inspect the character table Table 3.2 we see that different representations lead to different transformation behavior under certain symmetry operations. Assume that we transform the system with inversion operation $\mathcal{I}$ and assume that the Hamiltonian contains a first term transforming under the A_{1g} and a second term transforming under the A_{1u} representation. We see that the first term stays the same when we apply $\mathcal{I}$. In contrast the second term acquires a minus sign. Thus the whole Hamiltonian is not invariant under $\mathcal{I}$ anymore. This means that the symmetry group of the Hamiltonian is not $\mathrm{D}_{4\mathrm{h}}$ anymore but something smaller, more precisely the subgroup D_4. So we summarize: adding terms belonging to different representations leads to symmetry breaking. We show the possible breaking paths in Fig. 4.3. For a more detailed analysis of the breaking schemes see Appendix A.

4.3 System with a commensurate nesting vector $Q = (\pi, \pi, \pi)$

We assume that the system favors density waves with a commensurate wave vector $\boldsymbol{Q} = (\pi, \pi, \pi)$ which connects the two sides of the Fermi surface. The specific commensurate wave vector fulfills the relation $\boldsymbol{k} + 2\boldsymbol{Q} = \boldsymbol{k}$. For the classification we introduce the following spinor

$$\widehat{\Psi}^\dagger_{\boldsymbol{k}} = \begin{pmatrix} \hat{\psi}^\dagger_{\boldsymbol{k}} & \hat{\psi}^\dagger_{\boldsymbol{k}+\boldsymbol{Q}} \end{pmatrix}. \tag{4.20}$$

To avoid double-counting we restrict the wave vectors $\boldsymbol{k}$ in the Hamiltonian to the reduced Brillouin zone (RBZ) as follows

$$\hat{\chi}^\dagger_{\boldsymbol{k}} = \begin{pmatrix} \widehat{\Psi}^\dagger_{\boldsymbol{k}} & \mathcal{K}\widehat{\Psi}^\intercal_{\boldsymbol{k}} \end{pmatrix}, \tag{4.21}$$

$$\mathcal{H} = \frac{1}{2}\sum_{\boldsymbol{k}}^{\mathrm{RBZ}} \hat{\chi}^\dagger_{\boldsymbol{k}} \widehat{\mathcal{H}}(\boldsymbol{k})\hat{\chi}_{\boldsymbol{k}}\,. \tag{4.22}$$

In order to keep only this two component spinor the specific nesting wave vector must necessarily be invariant under the point group. For the $\mathrm{D}_{4\mathrm{h}}$ this works fine for $\boldsymbol{Q} = (\pi, \pi, \pi)$ and $\boldsymbol{Q} = (\pi, \pi, 0)$ but not for $\boldsymbol{Q}_x = (\pi, 0, 0)$. Rotation of $\boldsymbol{Q}_x$ would create the commensurate wave vector $\boldsymbol{Q}_y = (0, \pi, 0)$ and this would enlarge the spinor. In a group theoretical language this means that one has to include the star of $\boldsymbol{Q}_x$ to the spinor, where star means the set of all vectors obtained by carrying out the point group operations on $\boldsymbol{Q}_x$. We also performed a classification for a system with the commensurate wave vectors $\boldsymbol{Q}_{x,y}$ which we omitted from this thesis for reasons of compactness. The classification works in a similar way though. Now let's get back to the system with one commensurate wave vector $\boldsymbol{Q}$. We shall use the $\{\mathbb{1}_\rho, \rho_x, \rho_y, \rho_z\}$ Pauli matrices as basis for the momentum transfer space. Now we shall consider an additional symmetry transformation – translation by $\boldsymbol{Q}$ with operator $t_{\boldsymbol{Q}}$. From the definition we have that $t_{\boldsymbol{Q}}\boldsymbol{k} = \boldsymbol{k} + \boldsymbol{Q}$ and $\widehat{D}(t_{\boldsymbol{Q}}) = \rho_x$ since the translation doesn't act in spin, orbital and particle-hole space. As an action on the Hamiltonian we obtain

$$t^\dagger_{\boldsymbol{Q}}\widehat{\mathcal{H}}(\boldsymbol{k})t_{\boldsymbol{Q}} = \widehat{\mathcal{H}}(\boldsymbol{k}+\boldsymbol{Q}) = \widehat{D}^\dagger(t_{\boldsymbol{Q}})\widehat{\mathcal{H}}(\boldsymbol{k}+\boldsymbol{Q})\widehat{D}(t_{\boldsymbol{Q}}) = \rho_x\widehat{\mathcal{H}}(\boldsymbol{k})\rho_x\,. \tag{4.23}$$

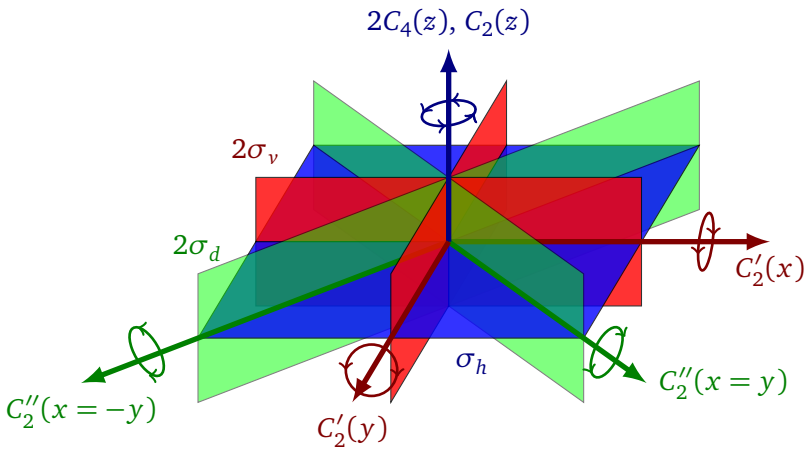

(a) Point group D_{4h}

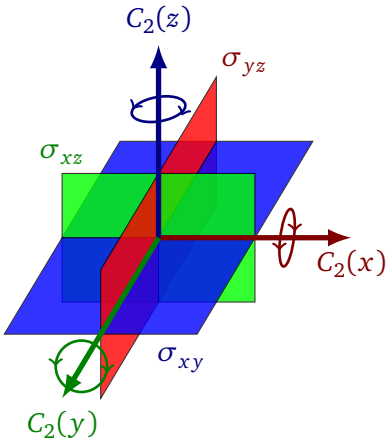

(b) Point group D_{2h}

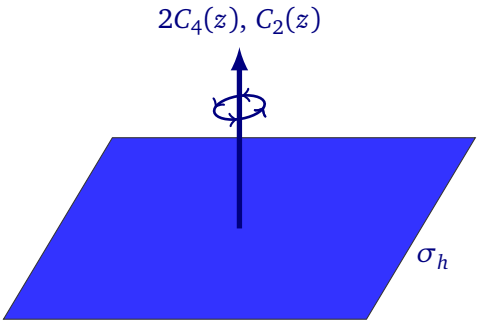

(c) Point group C_{4h}

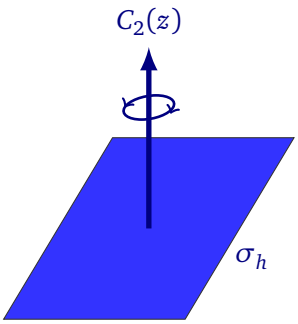

(d) Point group C_{2h}

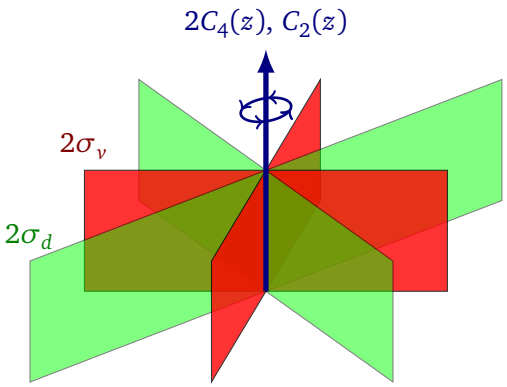

(e) Point group C_{4v}

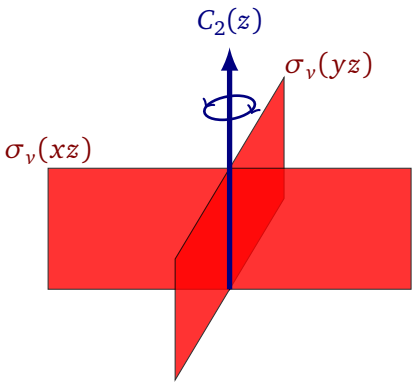

(f) Point group C_{2v}

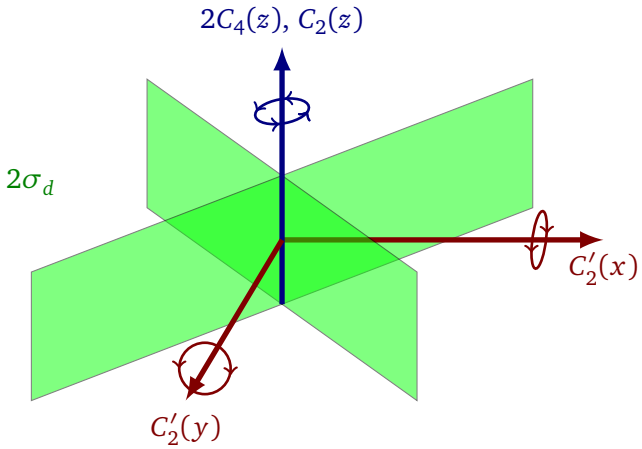

(g) Point group D_{2d}

Figure 4.2: Rotation axes and reflection planes of various point groups

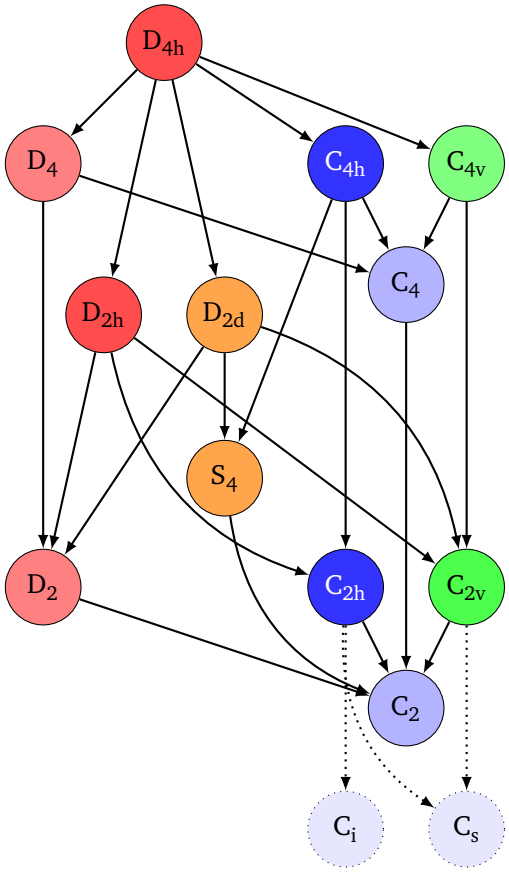

Figure 4.3: All subgroups of the point group D_{4h}. The arrows correspond to a breaking of the symmetry to a subgroup. The subgroups C_s and C_i cannot be reached by the discussed symmetry breaking scheme.

We see that the translation by $\boldsymbol{Q}$ can be carried out in two different ways. Now let's consider the case of a single orbital and a spin-1/2 system using the spinor $\hat{\psi}^\dagger_{\boldsymbol{k}} = \begin{pmatrix} c^\dagger_{\boldsymbol{k}\uparrow} & c^\dagger_{\boldsymbol{k}\downarrow} \end{pmatrix}$ where the Pauli matrices $\{\mathbb{1}_\sigma, \sigma_x, \sigma_y, \sigma_z\}$ act in spin space. Using the results from Section 4.1 and Chapter 3 we can write down the action of the symmetry operations $\mathcal{I}, \mathcal{T}, \mathcal{C}$ and the point group on the BdG Hamiltonian $\widehat{\mathcal{H}}(\boldsymbol{k})$. In principle we have to find the symmetry operations for the enlarged spinor including the ρ space. The wave-vector $\boldsymbol{Q}$ is invariant under the transformations and consequently the action of the symmetry operations doesn't change. We write down the complete set of discrete symmetry operations of the Hamiltonian

$$\mathcal{I}^\dagger \widehat{\mathcal{H}}(\boldsymbol{k})\mathcal{I} = \widehat{\mathcal{H}}(-\boldsymbol{k}) = -\tau_x \widehat{\mathcal{H}}^\intercal(\boldsymbol{k})\tau_x\,, \tag{4.24}$$

$$\mathcal{T}^\dagger \widehat{\mathcal{H}}(\boldsymbol{k})\mathcal{T} = \sigma_y \widehat{\mathcal{H}}^*(-\boldsymbol{k})\sigma_y = -\tau_x\sigma_y \widehat{\mathcal{H}}(\boldsymbol{k})\tau_x\sigma_y\,, \tag{4.25}$$

$$\mathcal{C}^\dagger \widehat{\mathcal{H}}(\boldsymbol{k})\mathcal{C} = \tau_x \widehat{\mathcal{H}}(\boldsymbol{k})\tau_x = -\widehat{\mathcal{H}}^\intercal(-\boldsymbol{k})\,. \tag{4.26}$$

For the point group operations we obtain

$$\overline{C}_4 \widehat{\mathcal{H}}(\boldsymbol{k})C_4 = \frac{\mathbb{1} + i\tau_z\sigma_z}{\sqrt{2}}\, \widehat{\mathcal{H}}(C_4\boldsymbol{k})\, \frac{\mathbb{1} - i\tau_z\sigma_z}{\sqrt{2}}\,, \tag{4.27}$$

$$C_4 \widehat{\mathcal{H}}(\boldsymbol{k})\overline{C}_4 = \frac{\mathbb{1} - i\tau_z\sigma_z}{\sqrt{2}}\, \widehat{\mathcal{H}}(\overline{C}_4\boldsymbol{k})\, \frac{\mathbb{1} + i\tau_z\sigma_z}{\sqrt{2}}\,, \tag{4.28}$$

$$C_2^\dagger \widehat{\mathcal{H}}(\boldsymbol{k})C_2 = \tau_z\sigma_z \widehat{\mathcal{H}}(C_2\boldsymbol{k})\tau_z\sigma_z\,, \tag{4.29}$$

$$C_{2a}'^\dagger \widehat{\mathcal{H}}(\boldsymbol{k})C_{2a}' = \tau_z\sigma_x \widehat{\mathcal{H}}(C_{2a}'\boldsymbol{k})\tau_z\sigma_x\,, \tag{4.30}$$

$$C_{2b}'^\dagger \widehat{\mathcal{H}}(\boldsymbol{k})C_{2b}' = \sigma_y \widehat{\mathcal{H}}(C_{2b}'\boldsymbol{k})\sigma_y\,, \tag{4.31}$$

$$C_{2a}''^\dagger \widehat{\mathcal{H}}(\boldsymbol{k})C_{2a}'' = \frac{\tau_z\sigma_x - \sigma_y}{\sqrt{2}}\, \widehat{\mathcal{H}}(C_{2a}''\boldsymbol{k})\, \frac{\tau_z\sigma_x + \sigma_y}{\sqrt{2}}\,, \tag{4.32}$$

$$C_{2b}''^\dagger \widehat{\mathcal{H}}(\boldsymbol{k})C_{2b}'' = \frac{\tau_z\sigma_x + \sigma_y}{\sqrt{2}}\, \widehat{\mathcal{H}}(C_{2b}''\boldsymbol{k})\, \frac{\tau_z\sigma_x - \sigma_y}{\sqrt{2}}\,. \tag{4.33}$$

Furthermore the Hamiltonian exhibits the discussed translational symmetry by $\boldsymbol{Q}$

$$t_{\boldsymbol{Q}}^\dagger \widehat{\mathcal{H}}(\boldsymbol{k})t_{\boldsymbol{Q}} = \widehat{\mathcal{H}}(\boldsymbol{k}+\boldsymbol{Q}) = \rho_x \widehat{\mathcal{H}}(\boldsymbol{k})\rho_x\,. \tag{4.34}$$

Now we can write all possible order parameters in the basis $\tau \otimes \rho \otimes \sigma$ and find their behavior under the symmetries thus classifying them. We follow similar steps as [30]. We find that the order parameters belong to different representations of the point group D_{4h}. For each order parameter we can find exemplary basis functions. The combination of basis function times order parameter matrix representation can be added to the Hamiltonian.

For shortness of notation we introduce the modified Pauli matrices in spin space $\tilde{\boldsymbol{\sigma}} = (\sigma_x, \tau_z\sigma_y, \sigma_z)$. The spin operators acquire the form $\tilde{\boldsymbol{S}} = \hbar\tau_z\tilde{\boldsymbol{\sigma}}/2 = \hbar(\tau_z\sigma_x, \sigma_y, \tau_z\sigma_z)/2$. As an overview we classify the generators under the $\mathcal{I}$, $\mathcal{T}$ and $t_{\boldsymbol{Q}}$ symmetry transformations distinguishing between particle-hole and particle-particle generators and between singlets and triplets in Table 4.1.

For each generator we find the allowed point group irreducible representations (I.R.) in Tables 4.2 to 4.4. The singlet generators in Table 4.2 carry the trivial A_{1g} and A_{1u} representations. By multiplication with the basis functions which carry the complete representation we obtain the complete order parameter. The triplet generators in Table 4.3 along the z-direction carry already the A_{2g} and A_{2u} representations since $\tau_z\sigma_z$ carries the A_{2g} representation. Multiplication with an A_{1g} basis function yields therefore a A_{2g} or A_{2u} order parameter. The triplet generators along the x- and y-direction transform under E_g and E_u representations. For example the $\tau_z(\tilde{\sigma}_x, \tilde{\sigma}_y) = (\tau_z\sigma_x, \sigma_y)$ in plane component of the vector $\tau_z\tilde{\boldsymbol{\sigma}}$ carries the E_g representation and therefore transforms like (xz, yz).

Table 4.1: Classifying the generators of SU(8) by inversion symmetry $\mathcal{I}$, time reversal symmetry $\mathcal{T}$, translation symmetry $t_{\boldsymbol{Q}}$ and momentum transfer $\boldsymbol{p}$

p-h generator	$\mathcal{I}$	$\mathcal{T}$	$t_{\boldsymbol{Q}}$	$\boldsymbol{p}$	p-p generator	$\mathcal{I}$	$\mathcal{T}$	$t_{\boldsymbol{Q}}$	$\boldsymbol{p}$
τ_z, $\tau_z\tilde{\boldsymbol{\sigma}}$	+	+,−	+	$\mathbf{0}$	$\tau_x\sigma_y$, $\tau_y\sigma_y$	+	−,+	+	$\mathbf{0}$
$\tau_z\rho_z$, $\tau_z\rho_z\tilde{\boldsymbol{\sigma}}$	+	+,−	−	$\mathbf{0}$	$\tau_x\rho_z\sigma_y$, $\tau_y\rho_z\sigma_y$	+	−,+	−	$\mathbf{0}$
$\tau_z\rho_x$, $\tau_z\rho_x\tilde{\boldsymbol{\sigma}}$	+	+,−	+	$\boldsymbol{Q}$	$\tau_x\rho_x\sigma_y$, $\tau_y\rho_x\sigma_y$	+	−,+	+	$\boldsymbol{Q}$
ρ_y, $\rho_y\tilde{\boldsymbol{\sigma}}$	+	−,+	−	$\boldsymbol{Q}$	$\tau_x\rho_y(i\sigma_y)\tilde{\boldsymbol{\sigma}}$, $\tau_y\rho_y(i\sigma_y)\tilde{\boldsymbol{\sigma}}$	+	+,−	−	$\boldsymbol{Q}$
$\tilde{\boldsymbol{\sigma}}$	−	+	+	$\mathbf{0}$	$\tau_x(i\sigma_y)\tilde{\boldsymbol{\sigma}}$, $\tau_y(i\sigma_y)\tilde{\boldsymbol{\sigma}}$	−	+,−	+	$\mathbf{0}$
ρ_z, $\rho_z\tilde{\boldsymbol{\sigma}}$	−	−,+	−	$\mathbf{0}$	$\tau_x\rho_z(i\sigma_y)\tilde{\boldsymbol{\sigma}}$, $\tau_y\rho_z(i\sigma_y)\tilde{\boldsymbol{\sigma}}$	−	+,−	−	$\mathbf{0}$
ρ_x, $\rho_x\tilde{\boldsymbol{\sigma}}$	−	−,+	+	$\boldsymbol{Q}$	$\tau_x\rho_x(i\sigma_y)\tilde{\boldsymbol{\sigma}}$, $\tau_y\rho_x(i\sigma_y)\tilde{\boldsymbol{\sigma}}$	−	+,−	+	$\boldsymbol{Q}$
$\tau_z\rho_y$, $\tau_z\rho_y\tilde{\boldsymbol{\sigma}}$	−	+,−	−	$\boldsymbol{Q}$	$\tau_x\rho_y\sigma_y$, $\tau_y\rho_y\sigma_y$	−	−,+	−	$\boldsymbol{Q}$

Table 4.2: Classifying the singlet generators which carry the A_{1g} representation

Generator	q	$\boldsymbol{p}$	$\mathcal{T}$	$\mathcal{I}$	$t_{\boldsymbol{Q}}$	I.R.	Representative basis functions
τ_z	0	$\mathbf{0}$	+	+	+	A_{1g}	1, $\cos 2k_z$, $\cos k_x \cos k_y$, $\cos 2k_x + \cos 2k_y$,
$\tau_z\rho_x$	0	$\boldsymbol{Q}$	+				$\cos k_z(\cos k_x + \cos k_y)$, $\cos k_x \cos k_y \cos 2k_z$
$\tau_y\sigma_y$	$2e$	$\mathbf{0}$	+			A_{2g}	$\sin k_x \sin k_y \cos k_z(\cos k_x - \cos k_y)$,
$\tau_x\sigma_y$	$2e$	$\mathbf{0}$	−				$\sin 2k_x \sin 2k_y(\cos k_x - \cos k_y)$,
$\tau_y\rho_x\sigma_y$	$2e$	$\boldsymbol{Q}$	+				$\sin k_x \sin k_y(\cos 2k_x - \cos 2k_y)$
$\tau_x\rho_x\sigma_y$	$2e$	$\boldsymbol{Q}$	−			B_{1g}	$\cos 2k_x - \cos 2k_y$, $\cos k_z(\cos k_x - \cos k_y)$
						B_{2g}	$\sin k_x \sin k_y$
$\tau_z\rho_z$	0	$\mathbf{0}$	+	+	−	A_{1g}	$\cos k_z$, $\cos k_x + \cos k_y$, $\cos k_z(\cos 2k_x + \cos 2k_y)$,
ρ_y	0	$\boldsymbol{Q}$	−				$\cos 2k_z(\cos k_x + \cos k_y)$, $\cos k_x \cos k_y \cos k_z$
$\tau_y\rho_z\sigma_y$	$2e$	$\mathbf{0}$	+			A_{2g}	$\sin k_x \sin k_y(\cos k_x - \cos k_y)$
$\tau_x\rho_z\sigma_y$	$2e$	$\mathbf{0}$	−			B_{1g}	$\cos k_x - \cos k_y$, $\cos k_z(\cos 2k_x - \cos 2k_y)$,
							$\cos 2k_z(\cos k_x - \cos k_y)$
						B_{2g}	$\sin k_x \sin k_y \cos k_z$
ρ_x	0	$\boldsymbol{Q}$	−	−	+	A_{1u}	$\sin k_x \sin k_y \sin k_z(\cos k_x - \cos k_y)$
						A_{2u}	$\sin 2k_z$, $\sin k_z(\cos k_x + \cos k_y)$,
							$\cos k_x \cos k_y \sin 2k_z$
						B_{1u}	$\sin k_x \sin k_y \sin 2k_z$
						B_{2u}	$\sin k_z(\cos k_x - \cos k_y)$
ρ_z	0	$\mathbf{0}$	−	−	−	A_{1u}	$\sin k_x \sin k_y \sin k_z(\cos 2k_x - \cos 2k_y)$
$\tau_z\rho_y$	0	$\boldsymbol{Q}$	+			A_{2u}	$\sin k_z$, $\cos k_x \cos k_y \sin k_z$,
$\tau_y\rho_y\sigma_y$	$2e$	$\boldsymbol{Q}$	+				$\sin 2k_z(\cos k_x + \cos k_y)$, $\sin k_z(\cos 2k_x + \cos 2k_y)$
$\tau_x\rho_y\sigma_y$	$2e$	$\boldsymbol{Q}$	−			B_{1u}	$\sin k_x \sin k_y \sin k_z$
						B_{2u}	$\sin 2k_z(\cos k_x - \cos k_y)$, $\sin k_z(\cos 2k_x - \cos 2k_y)$

Table 4.3: Classifying the triplet generators in the z-direction which carry the A_{2g} representation

Generator	q	$\boldsymbol{p}$	$\mathcal{T}$	$\mathcal{I}$	$t_{\boldsymbol{Q}}$	Rep.	Representative basis functions
$\tau_z\tilde{\sigma}_z$	0	$\boldsymbol{0}$	$-$	$+$	$+$	A_{1g}	$\sin k_x \sin k_y \cos k_z(\cos k_x - \cos k_y)$,
$\tau_z\rho_x\tilde{\sigma}_z$	0	$\boldsymbol{Q}$	$-$				$\sin k_x \sin k_y(\cos 2k_x - \cos 2k_y)$,
							$\sin 2k_x \sin 2k_y(\cos k_x - \cos k_y)$
						A_{2g}	$\cos 2k_z$, $\cos k_x \cos k_y$, $\cos 2k_x + \cos 2k_y$,
							$\cos k_z(\cos k_x + \cos k_y)$, $\cos k_x \cos k_y \cos 2k_z$
						B_{1g}	$\sin k_x \sin k_y$
						B_{2g}	$\cos 2k_x - \cos 2k_y$, $\cos k_z(\cos k_x - \cos k_y)$
$\tau_z\rho_z\tilde{\sigma}_z$	0	$\boldsymbol{0}$	$-$	$+$	$-$	A_{1g}	$\sin k_x \sin k_y(\cos k_x - \cos k_y)$
$\rho_y\tilde{\sigma}_z$	0	$\boldsymbol{Q}$	$+$			A_{2g}	$\cos k_z$, $\cos k_x + \cos k_y$, $\cos k_z(\cos 2k_x + \cos 2k_y)$,
$\tau_x\rho_y i\sigma_y\tilde{\sigma}_z$	$2e$	$\boldsymbol{Q}$	$+$				$\cos 2k_z(\cos k_x + \cos k_y)$, $\cos k_x \cos k_y \cos k_z$
$\tau_y\rho_y i\sigma_y\tilde{\sigma}_z$	$2e$	$\boldsymbol{Q}$	$-$			B_{1g}	$\sin k_x \sin k_y \cos k_z$
						B_{2g}	$\cos k_x - \cos k_y$, $\cos k_z(\cos 2k_x - \cos 2k_y)$,
							$\cos 2k_z(\cos k_x - \cos k_y)$
$\tilde{\sigma}_z$	0	$\boldsymbol{0}$	$+$	$-$	$+$	A_{1u}	$\sin 2k_z$, $\sin k_z(\cos k_x + \cos k_y)$, $\cos k_x \cos k_y \sin 2k_z$
$\rho_x\tilde{\sigma}_z$	0	$\boldsymbol{Q}$	$+$			A_{2u}	$\sin k_x \sin k_y \sin k_z(\cos k_x - \cos k_y)$
$\tau_y i\sigma_y\tilde{\sigma}_z$	$2e$	$\boldsymbol{0}$	$-$			B_{1u}	$\sin k_z(\cos k_x - \cos k_y)$
$\tau_x i\sigma_y\tilde{\sigma}_z$	$2e$	$\boldsymbol{0}$	$+$			B_{2u}	$\sin k_x \sin k_y \sin 2k_z$
$\tau_x\rho_x i\sigma_y\tilde{\sigma}_z$	$2e$	$\boldsymbol{Q}$	$+$				
$\tau_y\rho_x i\sigma_y\tilde{\sigma}_z$	$2e$	$\boldsymbol{Q}$	$-$				
$\rho_z\tilde{\sigma}_z$	0	$\boldsymbol{0}$	$+$	$-$	$-$	A_{1u}	$\sin k_z$, $\cos k_x \cos k_y \sin k_z$,
$\tau_z\rho_y\tilde{\sigma}_z$	0	$\boldsymbol{Q}$	$-$				$\sin 2k_z(\cos k_x + \cos k_y)$, $\sin k_z(\cos 2k_x + \cos 2k_y)$
$\tau_x\rho_z i\sigma_y\tilde{\sigma}_z$	$2e$	$\boldsymbol{0}$	$+$			A_{2u}	$\sin k_x \sin k_y \sin 2k_z(\cos k_x - \cos k_y)$,
$\tau_y\rho_z i\sigma_y\tilde{\sigma}_z$	$2e$	$\boldsymbol{0}$	$-$				$\sin k_x \sin k_y \sin k_z(\cos 2k_x - \cos 2k_y)$
						B_{1u}	$\sin 2k_z(\cos k_x - \cos k_y)$, $\sin k_z(\cos 2k_x - \cos 2k_y)$
						B_{2u}	$\sin k_x \sin k_y \sin k_z$

Table 4.4: Classifying the triplet generators in the x- and y-direction which carry the E_g representation

Generator	q	$\boldsymbol{p}$	$\mathcal{T}$	$\mathcal{I}$	$t_{\boldsymbol{Q}}$	I.R.	Representative basis functions
$\tau_z\tilde{\boldsymbol{\sigma}}_{xy}$	0	$\boldsymbol{0}$	$-$	$+$	$+$	A_{1g}	$\sin k_z(-\sin k_y, \sin k_x)$
$\tau_z\rho_x\tilde{\boldsymbol{\sigma}}_{xy}$	$\boldsymbol{Q}$	$-$				A_{2g}	$\sin k_z(\sin k_x, \sin k_y)$
						B_{1g}	$\sin k_z(\sin k_y, \sin k_x)$
						B_{2g}	$\sin k_z(\sin k_x, -\sin k_y)$
$\tau_z\rho_z\tilde{\boldsymbol{\sigma}}_{xy}$	0	$\boldsymbol{0}$	$-$	$+$	$-$	A_{1g}	$\sin k_z(-\sin 2k_y, \sin 2k_x)$, $\sin 2k_z(-\sin k_y, \sin k_x)$
$\rho_y\tilde{\boldsymbol{\sigma}}_{xy}$	0	$\boldsymbol{Q}$	$+$			A_{2g}	$\sin k_z(\sin 2k_x, \sin 2k_y)$, $\sin 2k_z(\sin k_x, \sin k_y)$
$\tau_x\rho_y i\sigma_y\tilde{\boldsymbol{\sigma}}_{xy}$	$2e$	$\boldsymbol{Q}$	$+$			B_{1g}	$\sin k_z(\sin 2k_y, \sin 2k_x)$, $\sin 2k_z(\sin k_y, \sin k_x)$
$\tau_y\rho_y i\sigma_y\tilde{\boldsymbol{\sigma}}_{xy}$	$2e$	$\boldsymbol{Q}$	$-$			B_{2g}	$\sin k_z(\sin 2k_x, -\sin 2k_y)$, $\sin 2k_z(\sin k_x, -\sin k_y)$
$\tilde{\boldsymbol{\sigma}}_{xy}$	0	$\boldsymbol{0}$	$+$	$-$	$+$	A_{1u}	$(\sin 2k_x, \sin 2k_y)$, $\cos k_z(\sin k_x, \sin k_y)$,
$\rho_x\tilde{\boldsymbol{\sigma}}_{xy}$	0	$\boldsymbol{Q}$	$+$				$(\cos k_x + \cos k_y)(\sin k_x, \sin k_y)$
$\tau_x i\sigma_y\tilde{\boldsymbol{\sigma}}_{xy}$	$2e$	$\boldsymbol{0}$	$+$			A_{2u}	$\cos k_z(-\sin k_y, \sin k_x)$, $(-\sin 2k_y, \sin 2k_x)$
$\tau_y i\sigma_y\tilde{\boldsymbol{\sigma}}_{xy}$	$2e$	$\boldsymbol{0}$	$-$			B_{1u}	$\cos k_z(\sin k_x, -\sin k_y)$, $(\sin 2k_x, -\sin 2k_y)$
$\tau_x\rho_x i\sigma_y\tilde{\boldsymbol{\sigma}}_{xy}$	$2e$	$\boldsymbol{Q}$	$+$			B_{2u}	$\cos k_z(\sin k_y, \sin k_x)$, $(\sin 2k_y, \sin 2k_x)$
$\tau_y\rho_x i\sigma_y\tilde{\boldsymbol{\sigma}}_{xy}$	$2e$	$\boldsymbol{Q}$	$-$				
$\rho_z\tilde{\boldsymbol{\sigma}}_{xy}$	0	$\boldsymbol{0}$	$+$	$-$	$-$	A_{1u}	$(\sin k_x, \sin k_y)$
$\tau_z\rho_y\tilde{\boldsymbol{\sigma}}_{xy}$	0	$\boldsymbol{Q}$	$-$			A_{2u}	$(-\sin k_y, \sin k_x)$
$\tau_x\rho_z i\sigma_y\tilde{\boldsymbol{\sigma}}_{xy}$	$2e$	$\boldsymbol{0}$	$+$			B_{1u}	$(\sin k_x, -\sin k_y)$
$\tau_y\rho_z i\sigma_y\tilde{\boldsymbol{\sigma}}_{xy}$	$2e$	$\boldsymbol{0}$	$-$			B_{2u}	$(\sin k_y, \sin k_x)$

4.4 Topological density waves

Using our classification we study a simple example with coexisting conventional and unconventional density waves in order to gain further insight concerning topological phase transitions. However this model is not of mere academic interest since the terms appearing in this Hamiltonian haven been proposed to appear separately or combined to describe the phenomenology of several materials as the cuprates and heavy fermion systems. We propose the BdG Hamiltonian

$$\begin{aligned}\widehat{\mathcal{H}}(\boldsymbol{k}) = & \underbrace{-t(\cos k_x + \cos k_y)\tau_z\rho_z}_{\text{Hopping}} \\ & + \underbrace{M_0^{\mathrm{C}}\tau_z\rho_x}_{\text{Charge density wave}} + \underbrace{M_0^{\mathrm{S}}\tau_z\rho_x\sigma_z}_{\text{Spin density wave}} \\ & + \underbrace{M^{\mathrm{C}}_{x^2-y^2}(\cos k_x - \cos k_y)\rho_y}_{\text{Singlet } id_{x^2-y^2}\text{-density wave}} + \underbrace{M^{\mathrm{C}}_{xy}\sin k_x \sin k_y \tau_z\rho_x}_{\text{Singlet } d_{xy}\text{-density wave}} \\ & + \underbrace{M^{\mathrm{S}}_{x^2-y^2}(\cos k_x - \cos k_y)\rho_y\sigma_z}_{\text{Triplet } id_{x^2-y^2}\text{-density wave}} + \underbrace{M^{\mathrm{S}}_{xy}\sin k_x \sin k_y \tau_z\rho_x\sigma_z}_{\text{Triplet } d_{xy}\text{-density wave}}\end{aligned} \tag{4.35}$$

with the kinetic parameter t and the charge and spin density wave strengths $M^{\mathrm{C,S}}$. See Fig. 4.5 for the structure of the terms in real lattice space and $\boldsymbol{k}$ space. The charge density wave occurs for example in $NbSe_3$ [6], the spin density waves in organic linear chain materials [31]. Different combinations of the singlet and triplet order parameters lead to time reversal breaking or invariance. The following time reversal symmetry breaking combinations have been proposed for the cuprates [32, 33, 34, 35]

$$\underbrace{M^{\mathrm{C}}_{x^2-y^2}(\cos k_x - \cos k_y)\rho_y}_{\text{Singlet } id_{x^2-y^2}\text{-density wave}} + \underbrace{M^{\mathrm{C}}_{xy}\sin k_x \sin k_y \tau_z\rho_x}_{\text{Singlet } d_{xy}\text{-density wave}}, \tag{4.36}$$

$$\underbrace{M^{\mathrm{S}}_{x^2-y^2}(\cos k_x - \cos k_y)\rho_y\sigma_z}_{\text{Triplet } id_{x^2-y^2}\text{-density wave}} + \underbrace{M^{\mathrm{S}}_{xy}\sin k_x \sin k_y \tau_z\rho_x\sigma_z}_{\text{Triplet } d_{xy}\text{-density wave}}. \tag{4.37}$$

Time reversal invariant combinations are also possible and were proposed in [36]

$$\underbrace{M^{\mathrm{C}}_{x^2-y^2}(\cos k_x - \cos k_y)\rho_y}_{\text{Singlet } id_{x^2-y^2}\text{-density wave}} + \underbrace{M^{\mathrm{S}}_{xy}\sin k_x \sin k_y \tau_z\rho_x\sigma_z}_{\text{Triplet } d_{xy}\text{-density wave}}, \tag{4.38}$$

$$\underbrace{M^{\mathrm{C}}_{xy}\sin k_x \sin k_y \tau_z\rho_x}_{\text{Singlet } d_{xy}\text{-density wave}} + \underbrace{M^{\mathrm{S}}_{x^2-y^2}(\cos k_x - \cos k_y)\rho_y\sigma_z}_{\text{Triplet } id_{x^2-y^2}\text{-density wave}}. \tag{4.39}$$

For the analysis we rewrite the system

$$\widehat{\mathcal{H}}(\boldsymbol{k}) = \begin{pmatrix} \begin{pmatrix} \hat{h}_\uparrow(\boldsymbol{k}) & 0 \\ 0 & \hat{h}_\downarrow(\boldsymbol{k}) \end{pmatrix} & 0 \\ 0 & \begin{pmatrix} -\hat{h}^{\intercal}_\uparrow(-\boldsymbol{k}) & 0 \\ 0 & -\hat{h}^{\intercal}_\downarrow(-\boldsymbol{k}) \end{pmatrix} \end{pmatrix}, \tag{4.40}$$

$$\hat{h}_\sigma(\boldsymbol{k}) = \boldsymbol{g}_\sigma(\boldsymbol{k})\cdot\boldsymbol{\rho}\,, \tag{4.41}$$

$$\boldsymbol{g}_\sigma(\boldsymbol{k}) = \begin{pmatrix} M_0^{\mathrm{C}} + M_0^{\mathrm{S}}\sigma + (M^{\mathrm{C}}_{xy} + M^{\mathrm{S}}_{xy}\sigma)\sin k_x \sin k_y \\ (M^{\mathrm{C}}_{x^2-y^2} + M^{\mathrm{S}}_{x^2-y^2}\sigma)(\cos k_x - \cos k_y) \\ -t(\cos k_x + \cos k_y) \end{pmatrix} \tag{4.42}$$

where the subblocks has a similar structure like the quantum spin Hall effect described in Section 1.5. The second block is due to the redundancy in the spinor (particle and hole terms). There are no off-diagonal

terms in particle-hole space in the Hamiltonian since our model doesn't include any superconducting terms. This means that we can concentrate on the upper left block only for further analysis. For convenience we introduce the following variables

$$M_0^\sigma = M_0^{\mathrm{C}} + M_0^{\mathrm{S}} \cdot \sigma\,, \quad M_{xy}^\sigma = M_{xy}^{\mathrm{C}} + M_{xy}^{\mathrm{S}} \cdot \sigma\,, \quad M_{x^2-y^2}^\sigma = M_{x^2-y^2}^{\mathrm{C}} + M_{x^2-y^2}^{\mathrm{S}} \cdot \sigma\,. \tag{4.43}$$

Using the new variables we obtain the vector field

$$\boldsymbol{g}_\sigma(\boldsymbol{k}) = \begin{pmatrix} M_0^\sigma + M_{xy}^\sigma \sin k_x \sin k_y \\ M_{x^2-y^2}^\sigma (\cos k_x - \cos k_y) \\ -t(\cos k_x + \cos k_y) \end{pmatrix}. \tag{4.44}$$

Assuming that all phases coexist which is equivalent to the condition that all individual terms are non-zero we can find gap closings $\boldsymbol{g}_\sigma(\boldsymbol{k}) = 0$ in the energy spectrum only for $M_0^\sigma = \pm M_{xy}^\sigma$. In this case we find the following four low energy points

$$\begin{aligned} M_0^\sigma &= +M_{xy}^\sigma \quad (-\pi/2, -\pi/2) \equiv (\pi/2, \pi/2)\,, \\ M_0^\sigma &= -M_{xy}^\sigma \quad (-\pi/2, \pi/2) \equiv (\pi/2, -\pi/2) \end{aligned}$$

which are pairwise equivalent in the reduced Brillouin zone as shown in Fig. 4.6. To determine the topological phases we compute the first Chern number or anomalous Hall conductivity

$$\sigma_{xy}^\sigma = -C_1^\sigma = -\frac{1}{4\pi} \int_{\mathrm{RBZ}} dk_x\, dk_y\, \hat{\boldsymbol{g}}_\sigma \cdot \left(\frac{\partial \hat{\boldsymbol{g}}_\sigma}{\partial k_x} \times \frac{\partial \hat{\boldsymbol{g}}_\sigma}{\partial k_y} \right). \tag{4.45}$$

Furthermore we define the in plane charge quantum Hall conductivity $\sigma_{xy}^{\mathrm{C}} = \sum_\sigma \sigma_{xy}^\sigma$ and the in plane spin quantum Hall conductivity $\sigma_{xy}^{\mathrm{S}} = \sum_\sigma \sigma \cdot \sigma_{xy}^\sigma$. Now we can compute the phases as shown in Table 4.5. We depict the different phases in Fig. 4.7.

Table 4.5: Topological phases of the topological density wave system

				Critical points	
Phase		σ_{xy}^σ		$(-\pi/2, \pi/2)$	$(-\pi/2, -\pi/2)$
Trivial	$\lvert M_{xy}^\sigma\rvert < \lvert M_0^\sigma\rvert$	0	$=$	$+s_\sigma/2$	$-s_\sigma/2$
Gap closing	$\lvert M_{xy}^\sigma\rvert = \lvert M_0^\sigma\rvert$				
Topological	$\lvert M_{xy}^\sigma\rvert > \lvert M_0^\sigma\rvert$	r_σ	$=$	$+r_\sigma/2$	$+r_\sigma/2$
$t > 0$,	$r_\sigma = \operatorname{sgn} M_{xy}^\sigma \cdot \operatorname{sgn} M_{x^2-y^2}^\sigma$,		$s_\sigma = r_\sigma \cdot \operatorname{sgn} M_0^\sigma$		

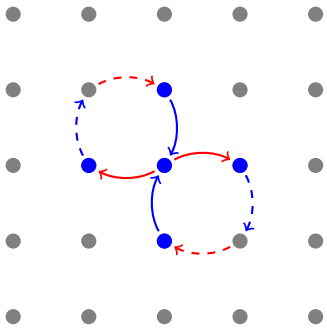

(a) $id_{x^2-y^2}$ hoppings in the real space lattice

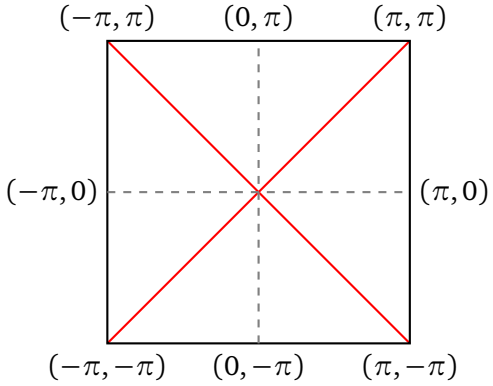

(b) $\cos k_x - \cos k_y = 0$ on the Brillouin zone

Figure 4.4: $id_{x^2-y^2}$-wave term

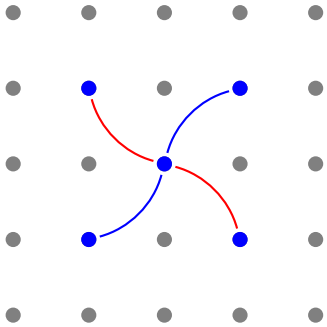

(c) d_{xy} hoppings in the real space lattice

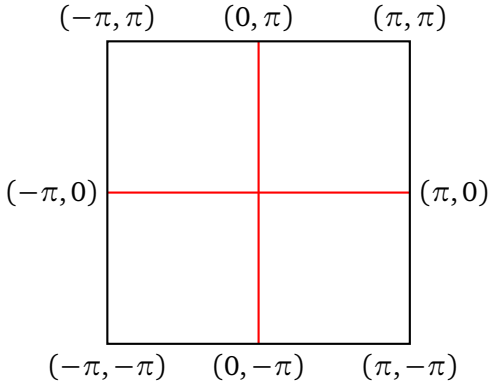

(d) $\sin k_x \sin k_y = 0$ on the Brillouin zone

Figure 4.5: d_{xy}-wave term

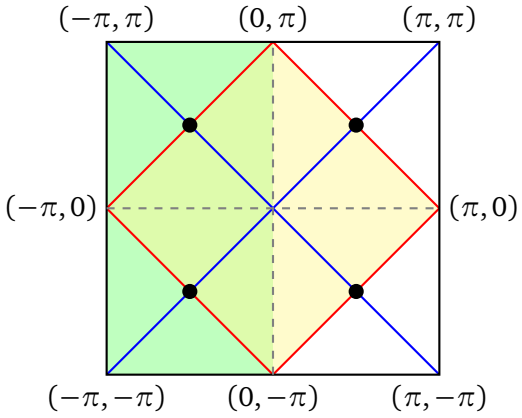

Figure 4.6: Brillouin zone for the topological density wave system. We show the four points relevant in the low energy limit. These are the points were gap closings can occur. Gap closings can only happen at points were $\cos k_x - \cos k_y = 0$ and $\cos k_x + \cos k_y = 0$. There are multiple equivalent ways to define a reduced Brillouin zone (shown in yellow and green).

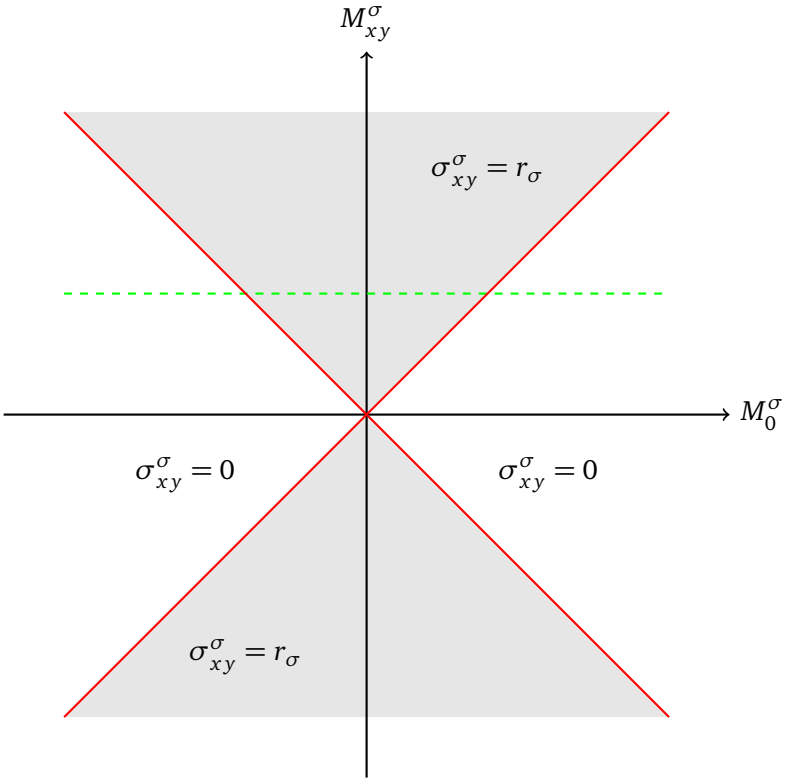

(a) Phase diagram depending on M^σ_0 and M^σ_{xy} with $r_\sigma = \operatorname{sgn} M^\sigma_{xy} \cdot \operatorname{sgn} M^\sigma_{x^2-y^2}$. We fix a certain M^σ_{xy} and cut along the green dashed line. Then we analyze further for the relation of M^C_0 and $M^\mathrm{S}_0 \cdot \sigma$ since $M^\sigma_0 = M^\mathrm{C}_0 + M^\mathrm{S}_0 \cdot \sigma$. We distinguish the two cases $r_\sigma = \pm 1$ and $r_\sigma = \pm\sigma$ which are shown in the following figures.

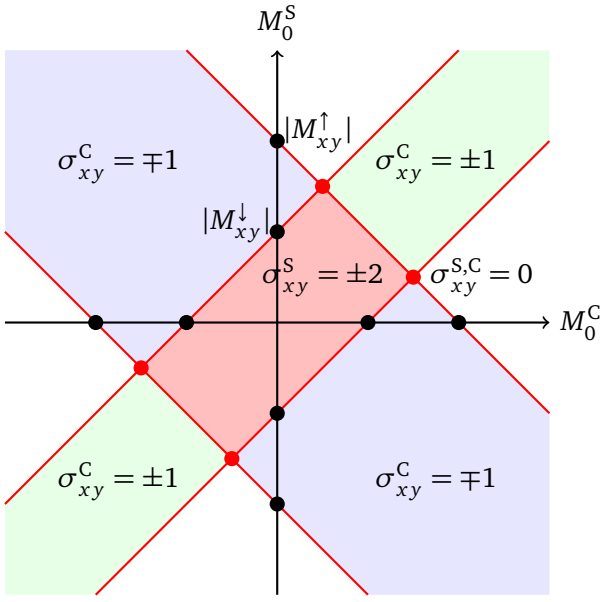

(b) $r_\sigma = \pm\sigma$

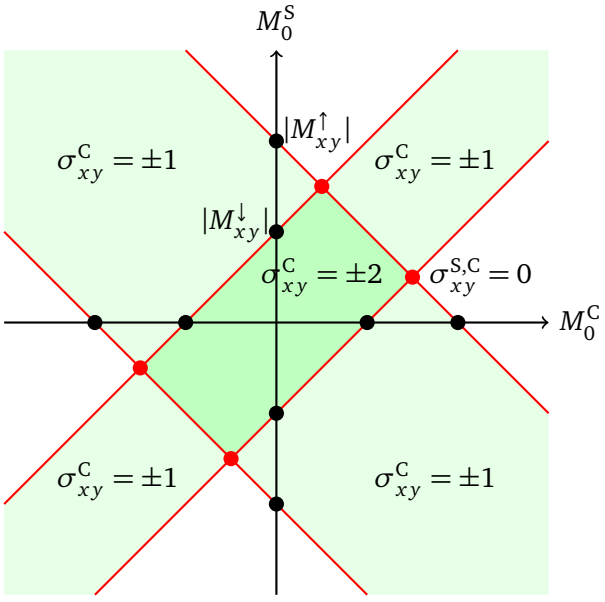

(c) $r_\sigma = \pm 1$

Figure 4.7: Phase diagrams for the topological density wave model

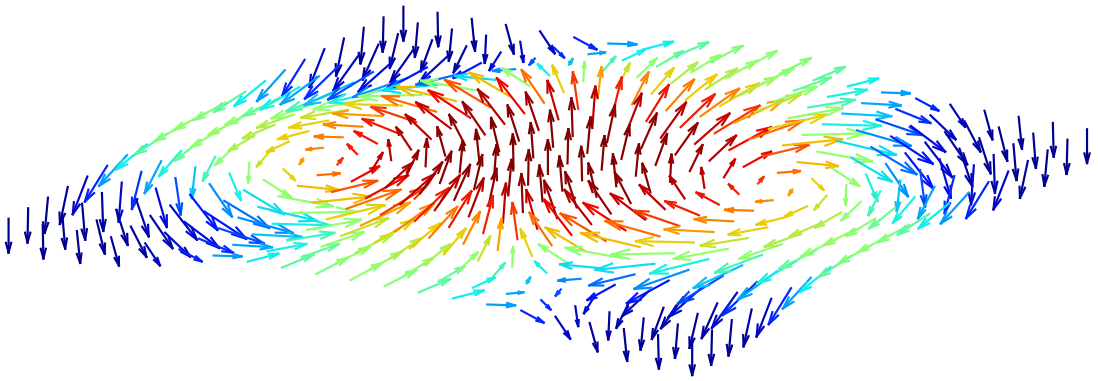

Figure 4.8: Vector field $\boldsymbol{g}_{\uparrow}(\boldsymbol{k}) = (\sin k_x \sin k_y,\ \cos k_x - \cos k_y,\ \cos k_x + \cos k_y)$ with Skyrmion structure and topological invariant 2 defined on the whole Brillouin zone $[-\pi, \pi]^2$.

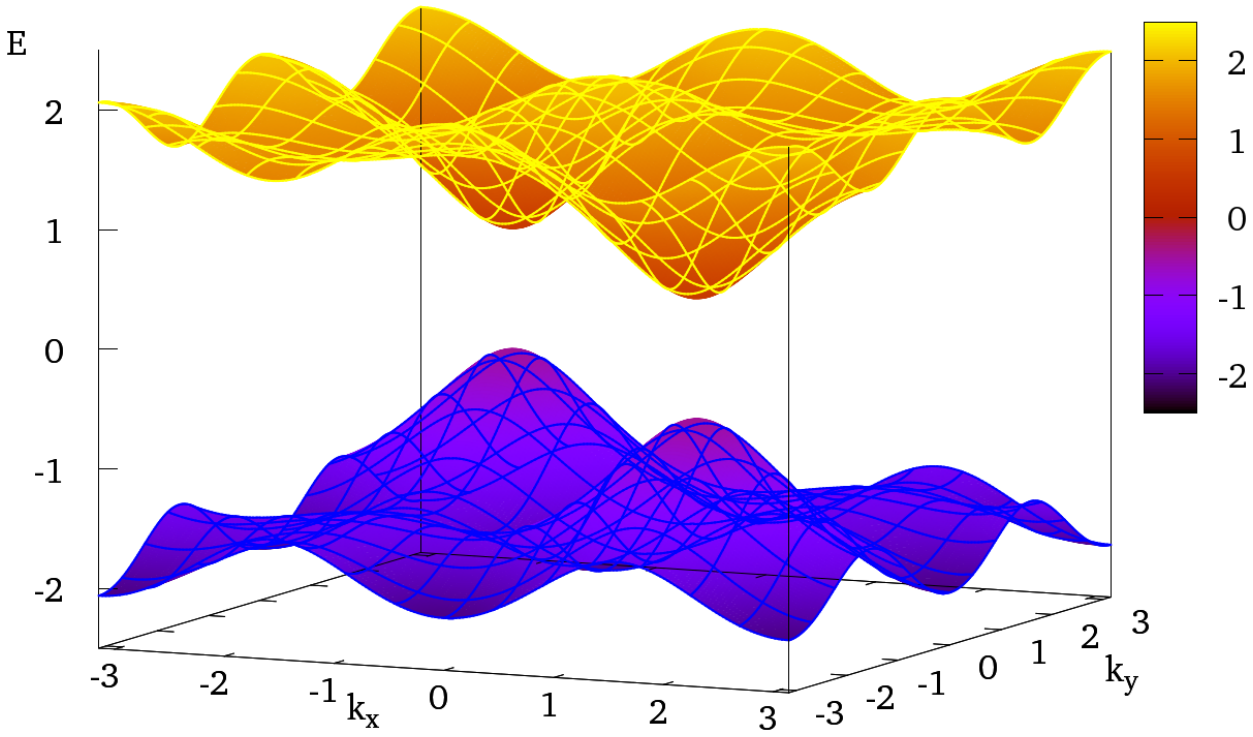

Figure 4.9: Bands of $\hat{h}_{\uparrow}(\boldsymbol{k})$ in the topologically non-trivial phase for $|M^{\sigma}_{xy}| > |M^{\sigma}_{0}|$

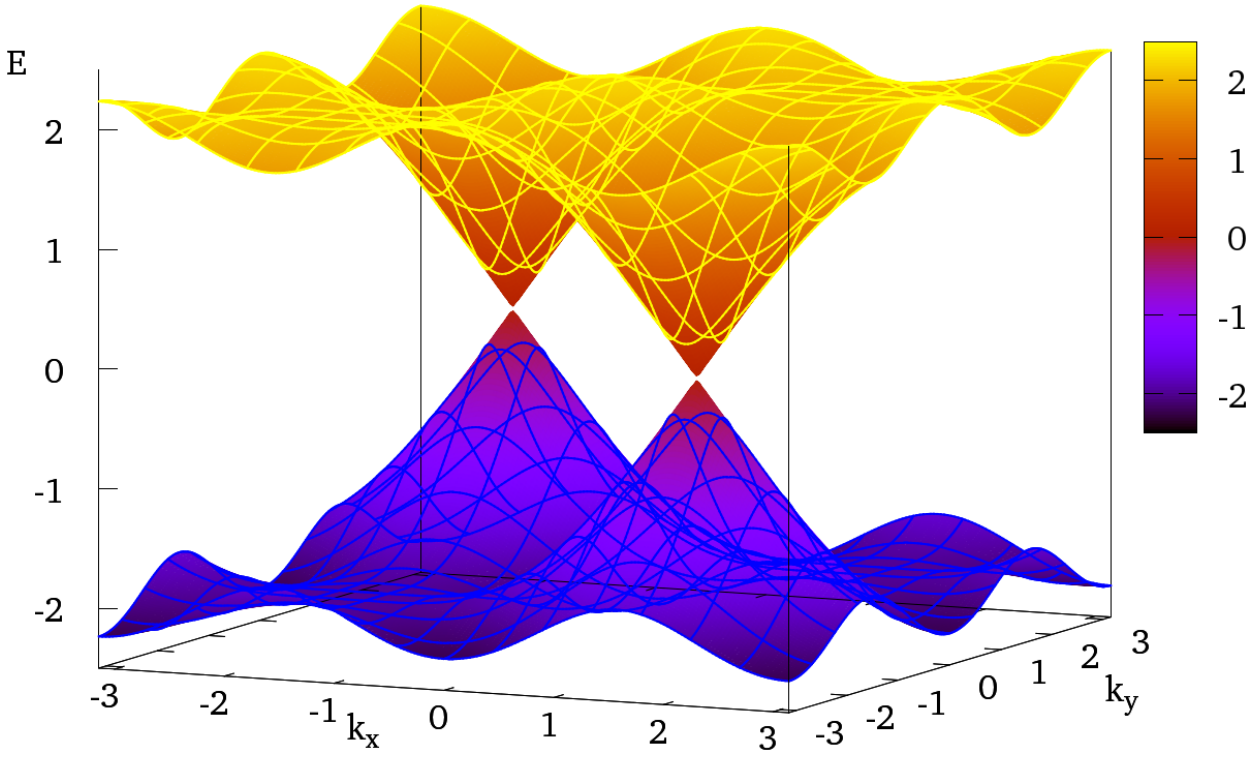

Figure 4.10: Bands of $\hat{h}_{\uparrow}(\boldsymbol{k})$ which show a gap closing for $|M^{\sigma}_{xy}| = |M^{\sigma}_{0}|$

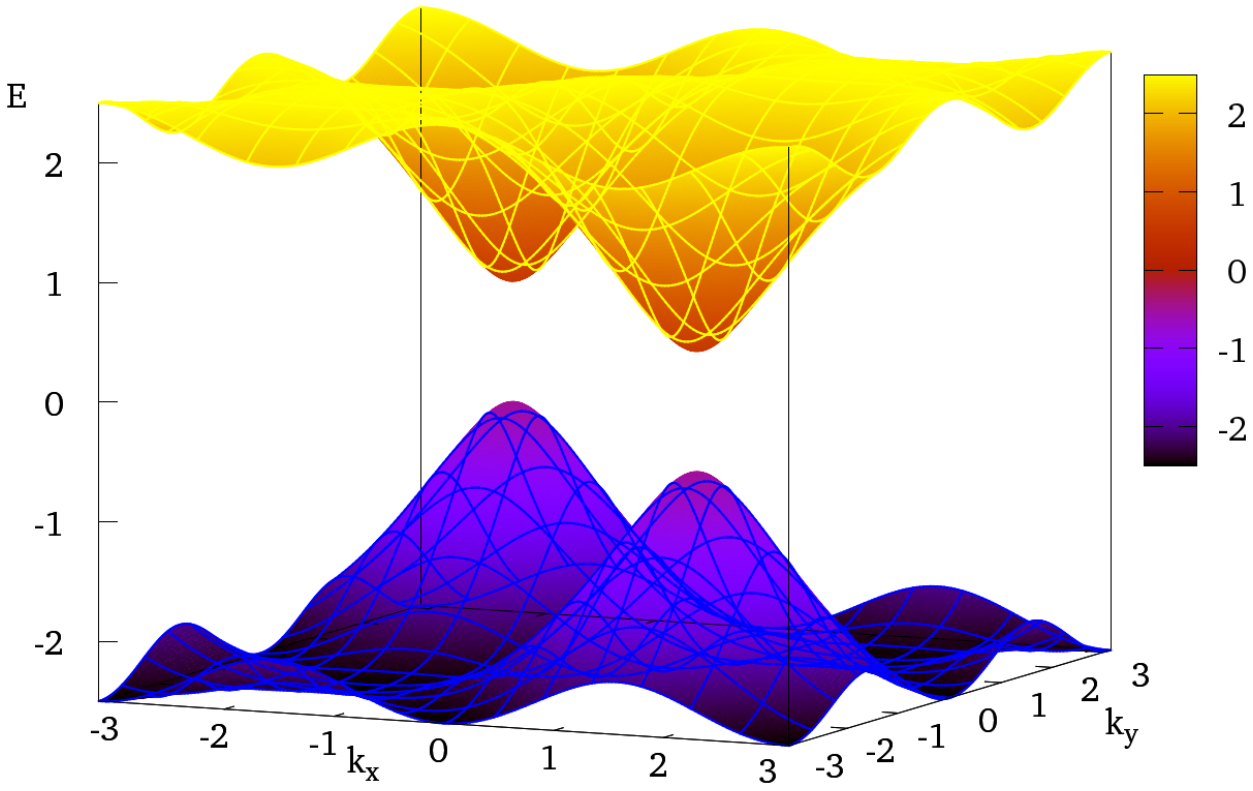

Figure 4.11: Bands of $\hat{h}_{\uparrow}(\boldsymbol{k})$ in the topologically trivial phase for $|M^{\sigma}_{xy}| < |M^{\sigma}_{0}|$

Chapter 5

Spin density waves and Majorana modes in Bi_2Te_3

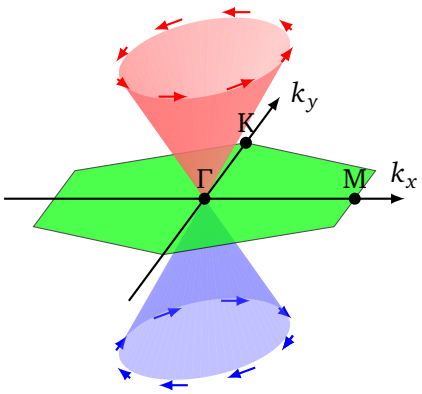

Figure 5.1: Dirac cone

Bi_2Te_3 is a time reversal invariant 3D topological insulator in the class of Bi-compounds which manifests its topologically non-trivial structure through helical surface states [38]. A distinctive feature of this 3D topological insulator is the large insulating band gap in the bulk compared to the insulators discovered earlier. In this chapter we want to apply the described classification methods onto the Dirac electrons on the [111][1] surface of the bulk topological insulator. The surface states of bulk topological insulators show helical dispersion around $\boldsymbol{k} = 0$. This usually leads to the formation of a single Dirac cone dispersion on the surface as shown in Fig. 5.1. Lowest order of $k \cdot p$ perturbation theory yields a Rashba spin-orbit coupling term $k_x\sigma_y - k_y\sigma_x$ in the first order Hamiltonian describing an isotropic 2D Dirac fermion around the Γ point

$$\widehat{\mathcal{H}}_0(\boldsymbol{k}) = v_0(k_x\sigma_y - k_y\sigma_x) \tag{5.1}$$

where v_0 is the Dirac velocity or strength of the Rashba term. We see that the lowest order Rashba term leaves the system rotationally invariant thus giving rise to an emerging U(1) rotation symmetry of the system around the z-axis. We refer to [39] for the derivation of Hamiltonians using $k \cdot p$ theory and symmetries. However ARPES[2] measurements of the Bi_2Te_3 dispersion show a hexagonal warping of the Fermi surface, compared to the circular Fermi surface that was expected (See Fig. 5.2). Fu proposed an additional warping term which is added to the standard Rashba-Dirac Hamiltonian to describe the warping effects [40]. The warping term is fixed by the threefold rotation symmetry of the Bi_2Te_3 surface and corresponds to a third order term in $k \cdot p$ perturbation theory effectively breaking the rotational

[1] Miller indices in the direct lattice
[2] Angle-resolved photon emission spectroscopy

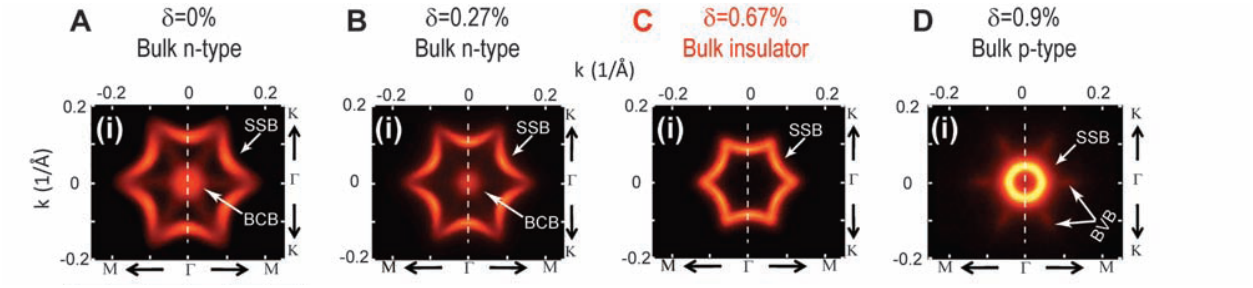

(a) Fermi surface symmetrized according to crystal symmetry. The pocket formed by the surface state band (SSB) is observed for all dopings. The pocket from the bulk conductance band (BCB) shrinks upon doping and vanishes in columns C and D. In column D pockets formed by the bulk valence band (BVB) emerge outside the SSB pockets.

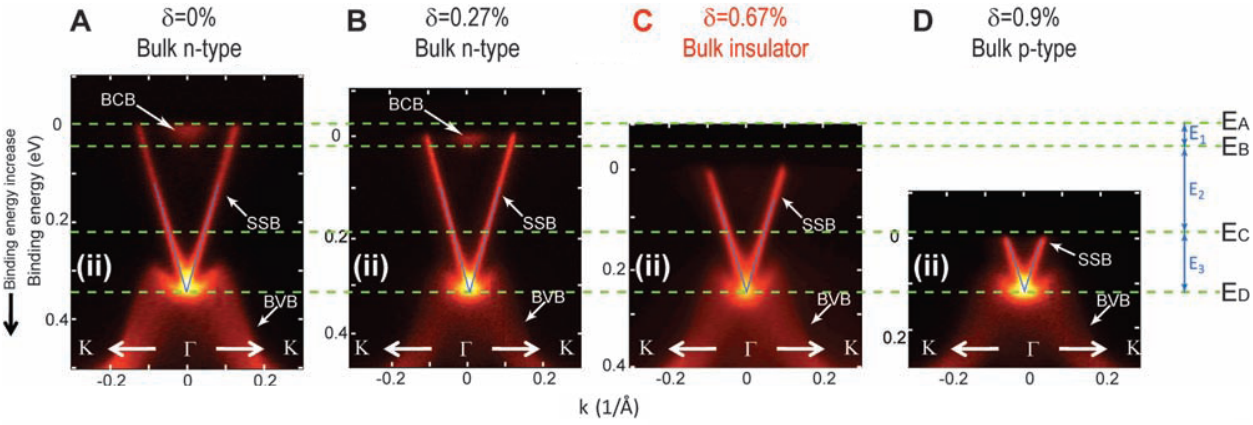

(b) Band dispersions along K-G-K direction as indicated by white dashed lines in (a). The E_F positions of the four doping samples are at 0.34, 0.325, 0.25, and 0.12 eV above the Dirac point, respectively. E_A is the Fermi energy for undoped Bi_2Te_3, E_B is the bottom of the BCB, E_C is the top of the BVB and E_D is the position of the Dirac point.

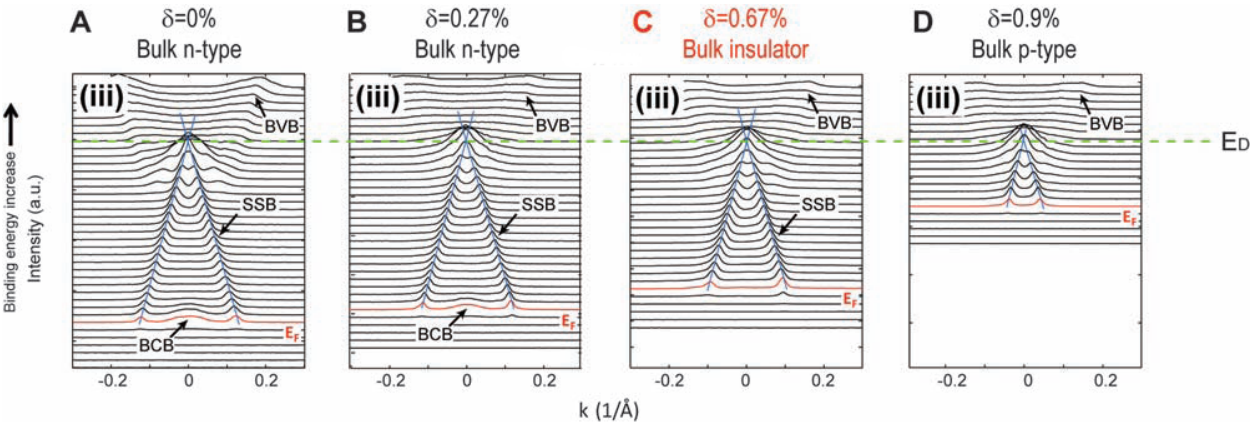

(c) Momentum distribution curve (MDC) plots of the raw data. The lorentzian peaks in the energy curves E_F correspond to the Fermi momentum k_F.

Figure 5.2: ARPES measurement of the Bi_2Te_3 surface [37] which show the doping dependence of Fermi surface and Fermi energy E_F. Columns A to D show measured Fermi surfaces and band dispersions for 0, 0.27, 0.67 and 0.9% doping. We are interested in the bulk insulating phase (doping 0.67%) where the Fermi surface forms a snowflake.

invariance of the lowest order Hamiltonian. The third order Hamiltonian is given by

$$\widehat{\mathcal{H}}_{\mathrm{Fu}}(\boldsymbol{k}) = E_0(k) + \underbrace{v_k(k_x\sigma_y - k_y\sigma_x)}_{\text{Rashba term}} + \underbrace{\frac{\Lambda}{2}\left(k_+^3 + k_-^3\right)\sigma_z}_{\text{Warping term}} \tag{5.2}$$

$$E_0(k) = \frac{k^2}{2m^*} - \mu \tag{5.3}$$

where $E_0(k)$ generates particle-hole asymmetry, m^* is an effective mass and μ is the chemical potential. The Dirac velocity $v_k = v_{-k} = v_0(1+\alpha k^2)$ contains a second order momentum correction α. Λ is a parameter describing the warping strength and $k_\pm = k_x \pm ik_y$ is introduced for ease of notation. There are studies discussing higher order $k\cdot p$ terms in the model resulting in better quantitative description [41]. For our more qualitative study these higher orders don't affect the existing picture. We can even assume momentum independence of the Dirac velocity v_k by setting $\alpha = 0$.

Hexagonal warping of the system gives the possibility for spin density waves if a certain filling is fixed by choosing a chemical potential via gating the system. The spin density waves can be understood as modulated magnetization of the material. In this chapter we want to investigate the possibilities for spin density waves to emerge and the topological properties of Bi_2Te_3 in proximity to an s-wave superconductor. It has been proposed that bulk topological insulators in proximity to s-wave superconductors lead to non-trivial topology and thus to the existence of zero energy Majorana modes [42]. In our setup we analyze the topological phases of the system in the regime of coexisting magnetization and superconductivity. The magnetization arises from the spin density waves, the superconductivity is induced by the superconductor via proximity effect. The precise mechanisms of the proximity effect need further investigation. In our work we just assume that correlations lead to an additional s-wave order parameter $\Delta\tau_y\sigma_y$ in the Hamiltonian, that can be explained as tunneling of Cooper pairs from the superconductor into the bulk topological insulator.

5.1 Crystal structure and C_{3v} symmetry

At this point we take a closer look at the rotation and reflection (point group) symmetries of the [111] surface of Bi_2Te_3 to understand the warping term in Eq. (5.3). To do that we need to consider the crystal structure of the material which is shown in Fig. 5.3. The top view Fig. 5.3b clearly shows a hexagonal structure (sixfold rotation) which is broken to threefold rotations because of the triangles corresponding to the Bi and Te1 atoms. The index in Te1 and Te2 describes the layers of the Te atoms if seen from the side as in Fig. 5.3a. The figure shows also the basis vectors $\boldsymbol{t}_{1,2,3}$ which are used to describe the [111] plane. More precisely, the [111] plane lies perpendicular to the vector $1\cdot\boldsymbol{t}_1 + 1\cdot\boldsymbol{t}_2 + 1\cdot\boldsymbol{t}_3$. For further discussion it is necessary to fix the orientation of the x axis which we choose to lie along the Γ to the high symmetry K point. These points are shown in Figs. 5.1 and 5.2.

The symmetry of the Bi_2Te_3 surface can be described by the point group C_{3v} (see the character table Table 5.1a) which consists of rotations by 120° around the z-axis (denoted C_3 and C_3^2), a reflection σ_v at the yz-plane and further reflections $\sigma_v' = C_3\sigma_v C_3^{-1}$ and $\sigma_v'' = C_3\sigma_v' C_3^{-1}$ which are just combinations of the reflection σ_v and rotations C_3. The reflection planes are depicted in Fig. 5.3c. Under threefold rotations of the system around the z-axis and the given reflections the Hamiltonian is left unchanged thus is called invariant under C_{3v}. Additionally the Hamiltonian is time reversal invariant. This explains why a threefold symmetric Hamiltonian features a sixfold symmetric Fermi surface. Based upon [40] we now take a closer look at the C_{3v} operations acting on the spin ladder operators $\sigma_\pm = \sigma_x \pm i\sigma_y$ and the similarly denoted momenta $k_\pm = k_x \pm ik_y$ in the complex plane. For the rotations we get

$$C_3 k_\pm = e^{\pm 2\pi i/3}k_\pm\,, \quad C_3^{-1}\sigma_\pm C_3 = e^{\pm 2\pi i/3}\sigma_\pm\,, \quad C_3^{-1}\sigma_z C_3 = \sigma_z \tag{5.4}$$

For the reflection σ_v at the yz-plane we get

$$\sigma_v k_\pm = -k_\mp\,, \quad \sigma_v^{-1}\sigma_\pm\sigma_v = \sigma_\mp\,, \quad \sigma_v^{-1}\sigma_z\sigma_v = -\sigma_z\,. \tag{5.5}$$

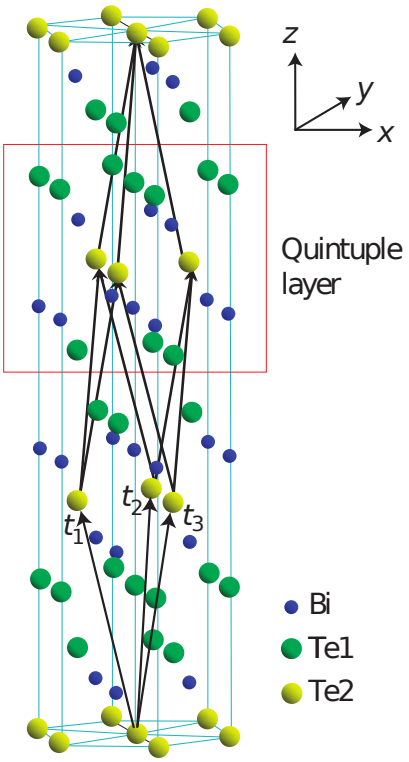

(a) Side view. The quintuple layer repeats itself along the z-axis. The [111] plane is perpendicular to $1 \cdot \boldsymbol{t}_1 + 1 \cdot \boldsymbol{t}_2 + 1 \cdot \boldsymbol{t}_3$ where $\boldsymbol{t}_{1,2,3}$ are the basis vectors shown in this figure.

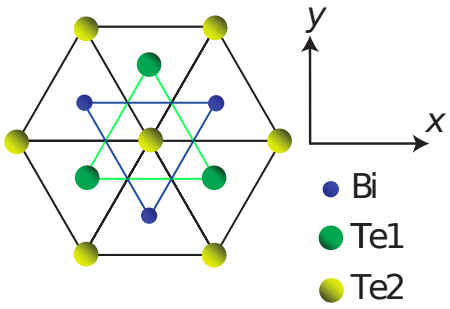

(b) Top view at the [111] surface. The structure shows a threefold rotation symmetry.

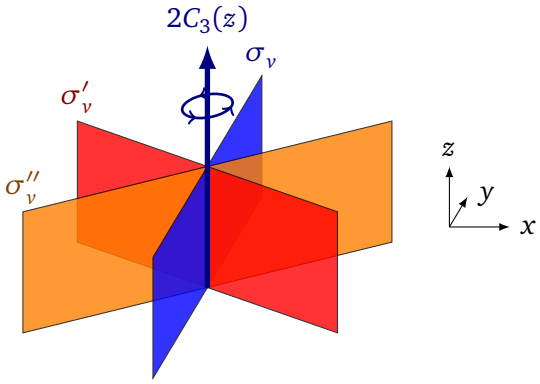

(c) Rotation axes and reflection planes of the point group C_{3v}.

Figure 5.3: Bi_2Te_3 crystal structure adapted from [43] and point group C_{3v}. x-axis goes from Γ to K point.

Table 5.1: Character tables of the threefold rotation groups in a plane: The Bi_2Te_3 surface is described by the point group C_{3v}. If we add two terms to a Hamiltonian which belong to A_1 and A_2 respectively the resulting term will not be C_{3v} invariant anymore since the terms transform differently under the three σ_v's (Highlighted with red in the table). The point group symmetry is broken to a C_3 symmetry.

(a) Character table of C_{3v}

I.R.	E	$2C_3$	$3\sigma_v$	Linear, Rotations	Higher functions
A_1	$+1$	$+1$	$+1$	z	$x^2+y^2, z^2, z^3, y(3x^2-y^2)$
A_2	$+1$	$+1$	-1	R_z	$x(x^2-3y^2)$
E	$+2$	-1	0	$(x,y), (R_x,R_y)$	$(x^2-y^2,xy), (xz,yz)$

(b) Character table of C_3 ($\epsilon = e^{2\pi i/3}$)

I.R.	E	C_3	C_3^2	Linear, Rotations	Higher functions
A	$+1$	$+1$	$+1$	z, R_z	$x^2+y^2, z^2, z^3, x(x^2-3y^2), y(3x^2-y^2)$
E	$+1$	ϵ	ϵ^*	$x+iy, R_x+iRy$	$(x^2-y^2,xy), (yz,xz)$
E	$+1$	ϵ^*	ϵ	$x-iy, R_x-iRy$	$(x^2-y^2,xy), (yz,xz)$

Note that the point group operators (which are matrices) act on the spin operators (which are matrices) from both sides. Compared to that the point group operators acts only from the left on the momentum vectors. We see that the transformation rules of the spin momentum ladder operators and the $k_\pm$ momenta under rotations are the same. The reason for this behavior is that they belong both to the two-dimensional representation of the group C_{3v}. To be more explicit we write down the matrix representations of C_3 and σ_v in k-space

$$\widehat{D}_k(C_3) = \frac{1}{2}\begin{pmatrix} -1 & -\sqrt{3} \\ \sqrt{3} & -1 \end{pmatrix}, \quad \widehat{D}_k(\sigma_v) = \begin{pmatrix} -1 & 0 \\ 0 & 1 \end{pmatrix}. \tag{5.6}$$

In σ-space the rotations are generated by σ_z leading to $\widehat{D}_\sigma(C_3) = e^{-i\pi\sigma_z/3}$. Space inversion is equivalent to a 180° around the x-axis followed by a reflection at the yz-plane. Since spins are invariant under space inversion we get $\widehat{D}_\sigma(\sigma_v) = e^{i\pi\sigma_x/2} = i\sigma_x$.

Now let's get back shortly to the Hamiltonian. We see immediately why the form of the Hamiltonian is completely fixed by the point group C_{3v}. If we compare the following two Hamiltonians

$$\widehat{\mathcal{H}}_{\text{Helicity}}(\boldsymbol{k}) = \underbrace{\frac{\boldsymbol{k}^2}{2m}}_{A_1} + v\underbrace{\left(k_x\sigma_x + k_y\sigma_y\right)}_{A_2}, \tag{5.7}$$

$$\widehat{\mathcal{H}}_{\text{Rashba}}(\boldsymbol{k}) = \underbrace{\frac{\boldsymbol{k}^2}{2m}}_{A_1} + v\underbrace{\left(k_x\sigma_y - k_y\sigma_x\right)}_{A_1} \tag{5.8}$$

we see that the Hamiltonian with the helicity spin orbit coupling term $\widehat{\mathcal{H}}_{\text{Helicity}}$ breaks the point group C_{3v} because of the addition of two different one-dimensional point group representations.

5.2 Spin density waves

We want to investigate the possibility of the formation of spin density wave phases for the surface states of Bi_2Te_3. To stay close with the experiment we use the measured value [37] for the Fermi

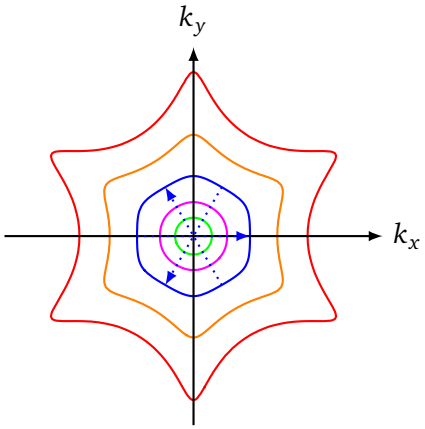

Figure 5.4: Snowflake structure of Fermi surface for different chemical potentials μ. For $\mu = 0.725E^*$ a nearly perfect hexagon forms. We show three incommensurate wave vectors. The k_x-axis goes from Γ to K point.

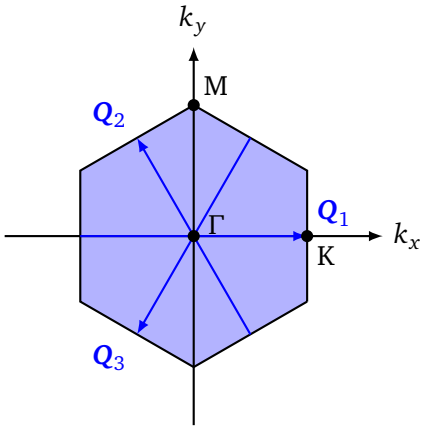

Figure 5.5: Fermi surface in perfect nesting with the three incommensurate wave vectors $\boldsymbol{Q}_{1,2,3}$ and high symmetry points Γ, M and K. The k_x-axis goes from Γ to K point.

velocity $v_0 = 2.55\,\text{eV Å}$. Fitting yields a value of $\Lambda = 250\,\text{eV Å}^3$ [40]. Using Λ and v_0 one can define a characteristic length scale $a = \sqrt{\Lambda/v_0}$ and a characteristic energy scale $E^* = v_0/a = \sqrt{v_0^3/\Lambda}$ in which the warping occurs. A sweep of the chemical potential μ in Eq. (5.3) the Fermi surface is circular for $\mu \lesssim 0.55E^*$, becomes more hexagonal for larger and finally bends inwards forming a snowflake like structure for $\mu \gtrsim 0.9E^*$. The Fermi surface for different values of μ is shown in Fig. 5.4. We study the situation where the Fermi surface forms an almost perfect hexagon, which leads to nearly perfect nesting. In our fit we found the hexagon at $\mu = 0.725E^*$. This means that there are incommensurate wave vectors connecting both sides of the Fermi surface. Perfect nesting can lead to the formation of spin density wave phases. The particle hole terms and the order parameters in the Hamiltonian carry then a certain momentum transfers. The momentum transfer in the perfect nesting case will be $\boldsymbol{Q}_{1,2,3}$ assuming that the system enters such a described spin density wave phase.

We find three nesting vectors $\boldsymbol{Q}_{1,2,3}$ which connect two sides of the Fermi surface as shown in Fig. 5.5. The wave vectors are rotated onto each other using a C_3 or C_3^{-1} operation. For our analysis we include the three incommensurate wave vectors $\boldsymbol{Q}_{1,2,3}$ in the spinor $\hat{\chi}_{\boldsymbol{k}}$ which becomes 24-dimensional

$$\hat{\psi}_{\boldsymbol{k}}^\dagger = \begin{pmatrix} c_{\boldsymbol{k}\uparrow}^\dagger & c_{\boldsymbol{k}\downarrow}^\dagger \end{pmatrix}, \tag{5.9}$$

$$\hat{\Psi}_{\boldsymbol{k}}^\dagger = \begin{pmatrix} \hat{\psi}_{\boldsymbol{k}+\boldsymbol{Q}_1/2}^\dagger & \hat{\psi}_{\boldsymbol{k}-\boldsymbol{Q}_1/2}^\dagger & \hat{\psi}_{\boldsymbol{k}+\boldsymbol{Q}_2/2}^\dagger & \hat{\psi}_{\boldsymbol{k}-\boldsymbol{Q}_2/2}^\dagger & \hat{\psi}_{\boldsymbol{k}+\boldsymbol{Q}_3/2}^\dagger & \hat{\psi}_{\boldsymbol{k}-\boldsymbol{Q}_3/2}^\dagger \end{pmatrix}, \tag{5.10}$$

$$\hat{\chi}_{\boldsymbol{k}}^\dagger = \begin{pmatrix} \hat{\Psi}_{\boldsymbol{k}}^\dagger & \mathcal{K}\hat{\Psi}_{\boldsymbol{k}}^\intercal \end{pmatrix} \tag{5.11}$$

$$= \begin{pmatrix} \hat{\psi}_{\boldsymbol{k}+\boldsymbol{Q}_1/2}^\dagger & \hat{\psi}_{\boldsymbol{k}-\boldsymbol{Q}_1/2}^\dagger & \hat{\psi}_{\boldsymbol{k}+\boldsymbol{Q}_2/2}^\dagger & \hat{\psi}_{\boldsymbol{k}-\boldsymbol{Q}_2/2}^\dagger & \hat{\psi}_{\boldsymbol{k}+\boldsymbol{Q}_3/2}^\dagger & \hat{\psi}_{\boldsymbol{k}-\boldsymbol{Q}_3/2}^\dagger \\ \hat{\psi}_{-(\boldsymbol{k}+\boldsymbol{Q}_1/2)}^\intercal & \hat{\psi}_{-(\boldsymbol{k}-\boldsymbol{Q}_1/2)}^\intercal & \hat{\psi}_{-(\boldsymbol{k}+\boldsymbol{Q}_2/2)}^\intercal & \hat{\psi}_{-(\boldsymbol{k}-\boldsymbol{Q}_2/2)}^\intercal & \hat{\psi}_{-(\boldsymbol{k}+\boldsymbol{Q}_3/2)}^\intercal & \hat{\psi}_{-(\boldsymbol{k}-\boldsymbol{Q}_3/2)}^\intercal \end{pmatrix} \tag{5.12}$$

where $\hat{\psi}_{\boldsymbol{k}}$ is the spinor in spin space σ and $\hat{\Psi}_{\boldsymbol{k}}$ is the spinor in $\lambda \otimes \rho \otimes \sigma$ space. The Pauli matrices $\{\mathbb{1}_\sigma, \sigma_x, \sigma_y, \sigma_z\}$ and $\{\mathbb{1}_\tau, \tau_x, \tau_y, \tau_z\}$ act in spin and in particle-hole space respectively as usual. λ_i with $i = 1, \ldots, 8$ denote the SU(3) generators (Gell-Mann matrices) acting on the nesting vectors and $\{\mathbb{1}_\rho, \rho_x, \rho_y, \rho_z\}$ are the Pauli matrices coupling operators of different momentum. The total spinor $\hat{\chi}_{\boldsymbol{k}}$ in Eq. (5.11) combines again particle and hole terms in Nambu space as usual to add the possibility for superconductivity. The complex conjugation $\mathcal{K}$ acts on the momenta $\boldsymbol{k}$ and $\boldsymbol{Q}_{1,2,3}$. Using the new

spinor we rewrite the Hamiltonian Eq. (5.3) and obtain

$$\mathcal{H} = \frac{1}{2}\sum_{\boldsymbol{k}} \hat{\chi}^\dagger_{\boldsymbol{k}} \widehat{\mathcal{H}}(\boldsymbol{k}) \hat{\chi}_{\boldsymbol{k}} \tag{5.13}$$

$$\begin{aligned}\widehat{\mathcal{H}}(\boldsymbol{k}) = \sum_{j=1}^{3} \frac{\mathbb{1}_\rho + \rho_z}{2} \Big[& E_0(\boldsymbol{k}+\boldsymbol{Q}_j/2)\tau_z \\ & + v_{\boldsymbol{k}+\boldsymbol{Q}_j/2}\left((\boldsymbol{k}+\boldsymbol{Q}_j/2)_x \tau_z\sigma_y - (\boldsymbol{k}+\boldsymbol{Q}_j/2)_y\sigma_x\right) \\ & + \frac{\Lambda}{2}\left((\boldsymbol{k}+\boldsymbol{Q}_j/2)_+^3 + (\boldsymbol{k}+\boldsymbol{Q}_j/2)_-^3\right)\sigma_z\Big] \\ + \sum_{j=1}^{3} \frac{\mathbb{1}_\rho - \rho_z}{2} \Big[& E_0(\boldsymbol{k}-\boldsymbol{Q}_j/2)\tau_z \\ & + v_{\boldsymbol{k}-\boldsymbol{Q}_j/2}\left((\boldsymbol{k}-\boldsymbol{Q}_j/2)_x \tau_z\sigma_y - (\boldsymbol{k}-\boldsymbol{Q}_j/2)_y\sigma_x\right) \\ & + \frac{\Lambda}{2}\left((\boldsymbol{k}-\boldsymbol{Q}_j/2)_+^3 + (\boldsymbol{k}-\boldsymbol{Q}_j/2)_-^3\right)\sigma_z\Big]. \end{aligned} \tag{5.14}$$

For further analysis we write down the action of inversion $\mathcal{I}$, time reversal $\mathcal{T}$ and charge conjugation $\mathcal{C}$ on the system. We have to consider the action on both the wave vectors $\boldsymbol{k}$ and the incommensurate wave vectors $\boldsymbol{Q}_{1,2,3}$ which are included for the momentum transfer. For convenience we denote $\boldsymbol{Q}$ for the three wave vectors $\boldsymbol{Q}_{1,2,3}$ and get

$$\mathcal{I}^\dagger \widehat{\mathcal{H}}(\boldsymbol{k},\boldsymbol{Q})\mathcal{I} = \widehat{\mathcal{H}}(-\boldsymbol{k},-\boldsymbol{Q}) = -\tau_x \widehat{\mathcal{H}}^\intercal(\boldsymbol{k},\boldsymbol{Q})\tau_x\,, \tag{5.15}$$

$$\mathcal{T}^\dagger \widehat{\mathcal{H}}(\boldsymbol{k},\boldsymbol{Q})\mathcal{T} = \sigma_y \widehat{\mathcal{H}}^*(-\boldsymbol{k},-\boldsymbol{Q})\sigma_y = -\tau_x\sigma_y \widehat{\mathcal{H}}(\boldsymbol{k},\boldsymbol{Q})\tau_x\sigma_y\,, \tag{5.16}$$

$$\mathcal{C}^\dagger \widehat{\mathcal{H}}(\boldsymbol{k},\boldsymbol{Q})\mathcal{C} = \tau_x \widehat{\mathcal{H}}(\boldsymbol{k},\boldsymbol{Q})\tau_x = -\widehat{\mathcal{H}}^\intercal(-\boldsymbol{k},-\boldsymbol{Q})\,. \tag{5.17}$$

Since we included the three incommensurate wave vectors $\boldsymbol{Q}_{1,2,3}$ in the spinor the group elements $\mathcal{G}$ of the point group C_{3v} acts in matrix space as follows

$$\mathcal{G}^\dagger \widehat{\mathcal{H}}(\boldsymbol{k},\boldsymbol{Q})\mathcal{G} \;= \widehat{D}^\dagger_{\tau\sigma}(\mathcal{G})\widehat{\mathcal{H}}(\mathcal{G}\boldsymbol{k},\mathcal{G}\boldsymbol{Q})\widehat{D}_{\tau\sigma}(\mathcal{G}) = \widehat{D}^\dagger(\mathcal{G})\widehat{\mathcal{H}}(\mathcal{G}\boldsymbol{k},\boldsymbol{Q})\widehat{D}(\mathcal{G})\,. \tag{5.18}$$

Essentially there are two equivalent ways the group acts on the wave vectors $\boldsymbol{Q}_{1,2,3}$ given by

$$\widehat{\mathcal{H}}(\boldsymbol{k},\mathcal{G}\boldsymbol{Q}) = \widehat{D}^\dagger_{\lambda\rho}(\mathcal{G})\widehat{\mathcal{H}}(\boldsymbol{k},\boldsymbol{Q})\widehat{D}_{\lambda\rho}(\mathcal{G})\,. \tag{5.19}$$

In the next step we determine the matrix representations of the group elements of C_{3v} at first in $\lambda\otimes\rho$ space. The rotation C_3 rotates the wave vector $\boldsymbol{Q}_1$ to $\boldsymbol{Q}_2$ etc. Therefore we find the representation

$$\widehat{D}_\lambda(C_3) = \begin{pmatrix} 0 & 0 & 1 \\ 1 & 0 & 0 \\ 0 & 1 & 0 \end{pmatrix} = \frac{\lambda_1 - i\lambda_2}{2} + \frac{\lambda_6 - i\lambda_7}{2} + \frac{\lambda_4 + i\lambda_5}{2}\,, \tag{5.20}$$

$$\widehat{D}_\rho(C_3) = \mathbb{1}_\rho\,. \tag{5.21}$$

The reflection at the yz-plane reflects $\boldsymbol{Q}_1 \to -\boldsymbol{Q}_1$ and $\boldsymbol{Q}_{2,3} \to -\boldsymbol{Q}_{3,2}$. Thus we find for the representation

$$\widehat{D}_\lambda(\sigma_v) = \begin{pmatrix} 1 & 0 & 0 \\ 0 & 0 & 1 \\ 0 & 1 & 0 \end{pmatrix} = \frac{2\mathbb{1}_\lambda + 3\lambda_3 + \sqrt{3}\lambda_8}{6} + \lambda_6\,, \tag{5.22}$$

$$\widehat{D}_\rho(\sigma_v) = \rho_x\,. \tag{5.23}$$

Combined with the representations $\widehat{D}_\sigma(C_3) = e^{-\pi i\sigma_z/3}$ and $\widehat{D}_\sigma(\sigma_v) = i\sigma_x$ in spin space we obtain the complete representations

$$\begin{aligned}\widehat{D}(C_3) &= \mathbb{1}_\tau \frac{\widehat{D}_{\lambda\rho\sigma}(C_3) + \widehat{D}^*_{\lambda\rho\sigma}(C_3)}{2} + \tau_z \frac{\widehat{D}_{\lambda\rho\sigma}(C_3) - \widehat{D}^*_{\lambda\rho\sigma}(C_3)}{2} \\ &= e^{-\pi i\tau_z\sigma_z/3}\left(\frac{\lambda_1 + i\lambda_2}{2} + \frac{\lambda_6 + i\lambda_7}{2} + \frac{\lambda_4 - i\lambda_5}{2}\right), \qquad (5.24)\\ \widehat{D}(\sigma_v) &= \mathbb{1}_\tau \frac{\widehat{D}_{\lambda\rho\sigma}(\sigma_v) + \widehat{D}^*_{\lambda\rho\sigma}(\sigma_v)}{2} + \tau_z \frac{\widehat{D}_{\lambda\rho\sigma}(\sigma_v) - \widehat{D}^*_{\lambda\rho\sigma}(\sigma_v)}{2} \\ &= i\tau_z\left(\frac{2\mathbb{1}_\lambda + 3\lambda_3 + \sqrt{3}\lambda_8}{6} + \lambda_6\right)\rho_x\sigma_x\,. \qquad (5.25)\end{aligned}$$

Due to the strong Fermi surface nesting it is likely that density waves can occur. Since the states at $\boldsymbol{k}$ and $-\boldsymbol{k}$ have opposite spin a charge density wave is disfavored. Thus we want to focus on SDWs and classify all the possible SDW order parameters in our formalism. The spin density wave order parameters are odd under time reversal

$$\mathcal{T}^\dagger\widehat{\mathcal{H}}(\boldsymbol{k},\boldsymbol{Q})\mathcal{T} = -\widehat{\mathcal{H}}(\boldsymbol{k},\boldsymbol{Q}) \implies \tau_x\sigma_y\widehat{\mathcal{H}}(\boldsymbol{k},\boldsymbol{Q})\tau_x\sigma_y = \widehat{\mathcal{H}}(\boldsymbol{k},\boldsymbol{Q}) \qquad (5.26)$$

We further assume that the order parameters are not modulated with $\boldsymbol{k}$ thus they can be written as follows

$$M(\boldsymbol{k},\boldsymbol{Q}) = f(\boldsymbol{k})M(\boldsymbol{Q}) = M(\boldsymbol{Q}) \qquad (5.27)$$

where $f(\boldsymbol{k}) = 1$ is assumed to be constant. Formally this means that the SDW order parameter is invariant under inversion of the $\boldsymbol{k}$ vector

$$\mathcal{I}^\dagger_{\boldsymbol{k}}\widehat{\mathcal{H}}(\boldsymbol{k},\boldsymbol{Q})\mathcal{I}_{\boldsymbol{k}} = -\tau_x\rho_x\widehat{\mathcal{H}}^*(\boldsymbol{k},\boldsymbol{Q})\tau_x\rho_x = \widehat{\mathcal{H}}(\boldsymbol{k},\boldsymbol{Q})\,. \qquad (5.28)$$

Using these constraints we search at first the SU(8) for possible order parameters which we list in Table 5.2a. Furthermore we classify the SU(3) generators which span the λ space and find the representations of C_{3v} that they belong to respectively (See Table 5.2b). For the sake of completeness and clarity we show the involved matrices

$$\lambda_1 + \lambda_4 + \lambda_6 = \begin{pmatrix}0&1&1\\1&0&1\\1&1&0\end{pmatrix}, \qquad \lambda_2 - \lambda_5 + \lambda_7 = \begin{pmatrix}0&-i&i\\i&0&-i\\-i&i&0\end{pmatrix}, \qquad (5.29)$$

$$\lambda_3 - \sqrt{3}\lambda_8 = \begin{pmatrix}0&0&0\\0&-2&0\\0&0&2\end{pmatrix}, \qquad \sqrt{3}\lambda_3 + \lambda_8 = \frac{1}{\sqrt{3}}\begin{pmatrix}4&0&0\\0&-2&0\\0&0&-2\end{pmatrix}, \qquad (5.30)$$

$$-\sqrt{3}\lambda_1 + \sqrt{3}\lambda_4 = \sqrt{3}\begin{pmatrix}0&-1&1\\-1&0&0\\1&0&0\end{pmatrix}, \quad \lambda_1 + \lambda_4 - 2\lambda_6 = \begin{pmatrix}0&1&1\\1&0&-2\\1&-2&0\end{pmatrix}, \qquad (5.31)$$

$$\lambda_2 - \lambda_5 + 2\lambda_7 = \begin{pmatrix}0&-i&i\\i&0&-2i\\-i&2i&0\end{pmatrix}, \sqrt{3}\lambda_2 + \sqrt{3}\lambda_5 = \sqrt{3}\begin{pmatrix}0&-i&-i\\i&0&0\\i&0&0\end{pmatrix}. \qquad (5.32)$$

The λ matrices and the SU(8) generators can be combined to form one-dimensional A_1 or A_2 representations. Because of the constraints it is only possible to combine real E representations and real A_1 representations in λ space with the generators in $\tau\otimes\rho\otimes\sigma$ space. We obtain the generators in Table 5.2c. Depending on the form of the parameter we distinguish Ising-, Rashba- and helicity-like terms. Ising-like terms describe spin density waves were the spin is modulated only in z-direction. The

Rashba- and helicity-like terms are products of two two-dimensional representations, one being (σ_x, σ_y) in spin space and one being (λ_x, λ_y) in λ space which takes the place of momentum. The (λ_x, λ_y) representation transforms exactly like (k_x, k_y). A Rashba-like term has the form

$$\lambda_x \rho_{x,y} \sigma_y - \tau_z \lambda_y \rho_{x,y} \sigma_x \tag{5.33}$$

while a helicity-like term has the form

$$\tau_z \lambda_x \rho_{x,y} \sigma_x + \lambda_y \rho_{x,y} \sigma_y \tag{5.34}$$

where λ_x and λ_y are the components of the two-dimensional representations in λ space, e.g.

$$\left(\lambda_x, \lambda_y\right) = \left(\lambda_3 - \sqrt{3}\lambda_8, \sqrt{3}\lambda_3 + \lambda_8\right). \tag{5.35}$$

The Rashba- and helicity-like terms are defined in λ space. This implies that the magnetization in coordinate $\boldsymbol{r}$-space should not necessarily have a Rashba- or helicity-like form. Other combinations of $\lambda_{x,y}$ and $\sigma_{x,y}$ are not possible without breaking the C_{3v} point group symmetry. However we find order parameters belonging to the representations A_1 and A_2 of the point group. Addition of A_2 order parameters to the Hamiltonian will necessarily lead to a reduction of the symmetry of the Hamiltonian to C_3 as discussed before in Section 4.2. This can also be seen when we consider the spin orientations. The reflection σ_v along the yz-plane inverts the x- and z-components of the spins (See Eq. (5.5)). This means that for the A_1 representations the y- and z-component of the spin should be inverted. For the A_2 representations the x-component of the spin should be inverted.

To see this we find the magnetization in coordinate $\boldsymbol{r}$-space by Fourier transformation (from Bloch to Wannier states) for each SDW order parameter. For the Ising-like SDW order parameter $\tau_z \rho_x \sigma_z$ we obtain for the spin in z-direction

$$\begin{aligned}\sum_{j=1}^{3} c^\dagger_{\boldsymbol{k}+\boldsymbol{Q}_j/2} c_{\boldsymbol{k}-\boldsymbol{Q}_j/2} + \text{H.c.} &\sim \int d\boldsymbol{r} \int d\boldsymbol{r}' \sum_{j=1}^{3} e^{-i(\boldsymbol{k}+\boldsymbol{Q}_j/2)\cdot\boldsymbol{r}} e^{i(\boldsymbol{k}-\boldsymbol{Q}_j/2)\cdot\boldsymbol{r}'} c^\dagger_{\boldsymbol{r}} c_{\boldsymbol{r}'} + \text{H.c.} \\ &\sim \int d\boldsymbol{r} \sum_{j=1}^{3} e^{-i\boldsymbol{Q}_j\cdot\boldsymbol{r}} c^\dagger_{\boldsymbol{r}} c_{\boldsymbol{r}} + \text{H.c.} \sim \int d\boldsymbol{r} \sum_{j=1}^{3} \cos\left(\boldsymbol{Q}_j \cdot \boldsymbol{r}\right) c^\dagger_{\boldsymbol{r}} c_{\boldsymbol{r}}\end{aligned} \tag{5.36}$$

which has to be counted 2 times because of diagonal τ space. This leads to a modulation of the σ_z-component with $\sum_{j=1}^{3} \cos\left(\boldsymbol{Q}_j \cdot \boldsymbol{r}\right)$ in coordinate $\boldsymbol{r}$-space. We perform a similar computation for all SDW order parameters that we found and plot the magnetizations in Figs. 5.6 to 5.17. We see the expected inversions in the x-, y- and z-component of the spin by mirroring along the yz-plane using the σ_v operation depending on the 1D representation of the SDW order parameter.

The next step is to calculate non-interacting susceptibilities for these order parameters given the Hamiltonian Eq. (5.14). This will be performed in the next section.

Table 5.2: Classification of the spin density wave order parameters

(a) Spin density wave order parameters in the SU(8) with their irreducible representation (I.R.) under the point group C_{3v}

I.R.	Generator
A_1	$\tau_z\rho_y\sigma_z$
A_2	$\tau_z\rho_x\sigma_z$
E	$(\tau_z\rho_x\sigma_x, \rho_x\sigma_y)$
E	$(\tau_z\rho_y\sigma_x, \rho_y\sigma_y)$

(b) SU(3) generators with their irreducible representation (I.R.) under the point group C_{3v}

I.R.	Generator
A_1	$\mathbb{1}_\lambda$
A_1	$\lambda_1+\lambda_4+\lambda_6$
A_2	$\lambda_2-\lambda_5+\lambda_7$
E	$(\lambda_3-\sqrt{3}\lambda_8, \sqrt{3}\lambda_3+\lambda_8)$
E	$(-\sqrt{3}\lambda_1+\sqrt{3}\lambda_4, \lambda_1+\lambda_4-2\lambda_6)$
E	$(\lambda_2-\lambda_5-2\lambda_7, \sqrt{3}\lambda_2+\sqrt{3}\lambda_5)$

(c) Combined spin density wave generators building Ising-, Rashba- and helicity-like terms.

Nr.	I.R.	Generator	Type
1	A_1	$\tau_z\rho_y\sigma_z$	Ising-like
2	A_1	$\tau_z(\lambda_1+\lambda_4+\lambda_6)\rho_y\sigma_z$	Ising-like
3	A_1	$(\lambda_3-\sqrt{3}\lambda_8)\rho_x\sigma_y-\tau_z(\sqrt{3}\lambda_3+\lambda_8)\rho_x\sigma_x$	Rashba-like
4	A_1	$(-\sqrt{3}\lambda_1+\sqrt{3}\lambda_4)\rho_x\sigma_y-\tau_z(\lambda_1+\lambda_4-2\lambda_6)\rho_x\sigma_x$	Rashba-like
5	A_1	$\tau_z(\lambda_3-\sqrt{3}\lambda_8)\rho_y\sigma_x+(\sqrt{3}\lambda_3+\lambda_8)\rho_y\sigma_y$	Helicity-like
6	A_1	$\tau_z(-\sqrt{3}\lambda_1+\sqrt{3}\lambda_4)\rho_y\sigma_x+(\lambda_1+\lambda_4-2\lambda_6)\rho_y\sigma_y$	Helicity-like
7	A_2	$\tau_z\rho_x\sigma_z$	Ising-like
8	A_2	$\tau_z(\lambda_1+\lambda_4+\lambda_6)\rho_x\sigma_z$	Ising-like
9	A_2	$(\lambda_3-\sqrt{3}\lambda_8)\rho_y\sigma_y-\tau_z(\sqrt{3}\lambda_3+\lambda_8)\rho_y\sigma_x$	Rashba-like
10	A_2	$(-\sqrt{3}\lambda_1+\sqrt{3}\lambda_4)\rho_y\sigma_y-\tau_z(\lambda_1+\lambda_4-2\lambda_6)\rho_y\sigma_x$	Rashba-like
11	A_2	$\tau_z(\lambda_3-\sqrt{3}\lambda_8)\rho_x\sigma_x+(\sqrt{3}\lambda_3+\lambda_8)\rho_x\sigma_y$	Helicity-like
12	A_2	$\tau_z(-\sqrt{3}\lambda_1+\sqrt{3}\lambda_4)\rho_x\sigma_x+(\lambda_1+\lambda_4-2\lambda_6)\rho_x\sigma_y$	Helicity-like

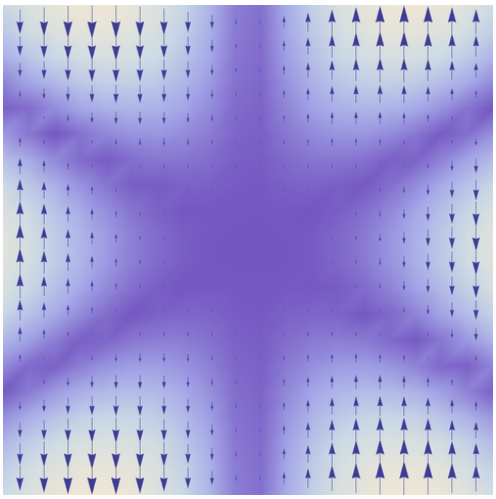

Figure 5.6: Magnetization in z-direction for Ising-like A_1 SDW order parameter 1 of the form $\tau_z\rho_y\sigma_z$. σ_v inverts z-component.

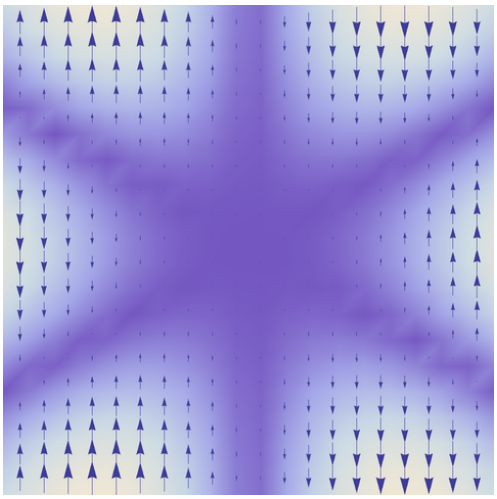

Figure 5.7: Magnetization in z-direction for Ising-like A_1 SDW order parameter 2 of the form $\tau_z(\lambda_1+\lambda_4+\lambda_6)\rho_y\sigma_z$. σ_v inverts z-component.

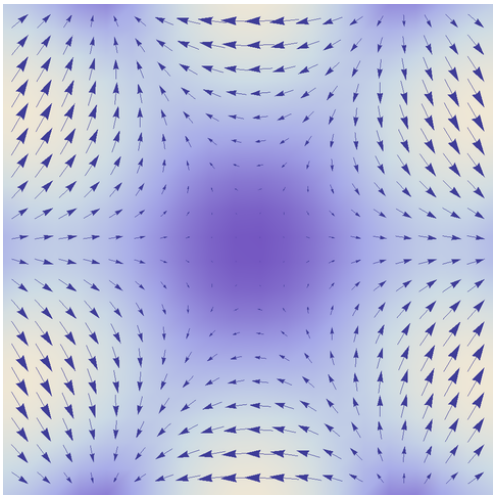

Figure 5.8: Magnetization for Rashba-like A_1 SDW order parameter 3 of the form $(\lambda_3-\sqrt{3}\lambda_8)\rho_x\sigma_y-\tau_z(\sqrt{3}\lambda_3+\lambda_8)\rho_x\sigma_x$. σ_v inverts y-component.

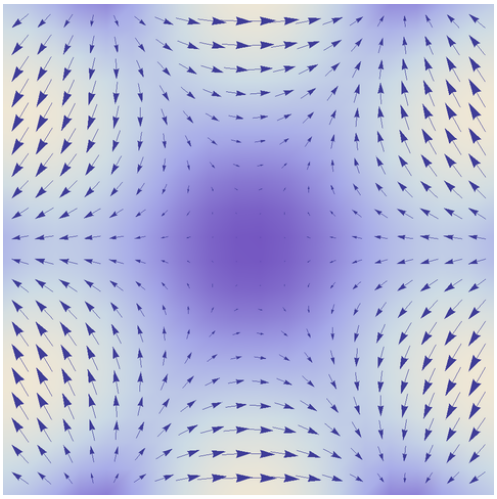

Figure 5.9: Magnetization for Rashba-like A_1 SDW order parameter 4 of the form $(-\sqrt{3}\lambda_1+\sqrt{3}\lambda_4)\rho_x\sigma_y-\tau_z(\lambda_1+\lambda_4-2\lambda_6)\rho_x\sigma_x$. σ_v inverts y-component.

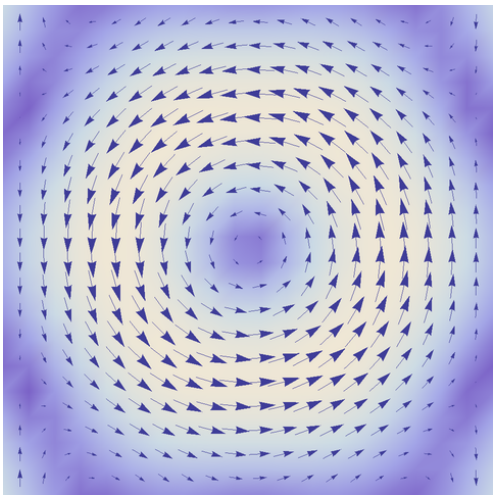

Figure 5.10: Magnetization for helicity-like A_1 SDW order parameter 5 of the form $\tau_z(\lambda_3-\sqrt{3}\lambda_8)\rho_y\sigma_x+(\sqrt{3}\lambda_3+\lambda_8)\rho_y\sigma_y$. σ_v inverts y-component.

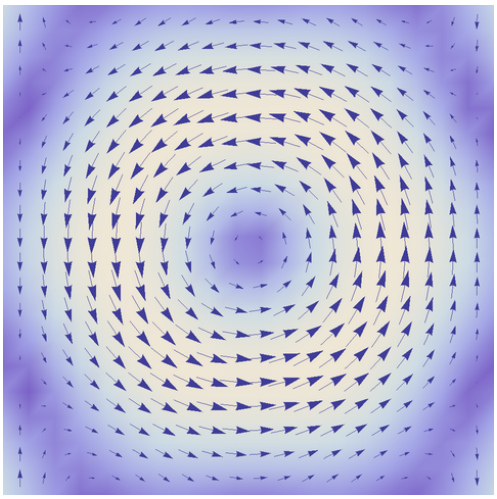

Figure 5.11: Magnetization for helicity-like A_1 SDW order parameter 6 of the form $\tau_z(-\sqrt{3}\lambda_1+\sqrt{3}\lambda_4)\rho_y\sigma_x+(\lambda_1+\lambda_4-2\lambda_6)\rho_y\sigma_y$. σ_v inverts y-component.

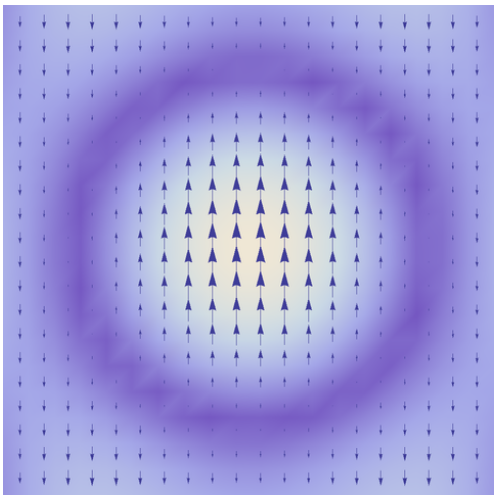

Figure 5.12: Magnetization in z-direction for Ising-like A_2 SDW order parameter 7 of the form $\tau_z\rho_x\sigma_z$. σ_v inverts x-component.

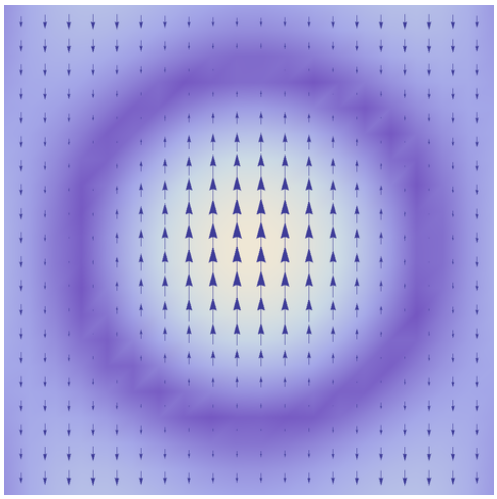

Figure 5.13: Magnetization in z-direction for Ising-like A_2 SDW order parameter 8 of the form $\tau_z(\lambda_1+\lambda_4+\lambda_6)\rho_x\sigma_z$. σ_v inverts x-component.

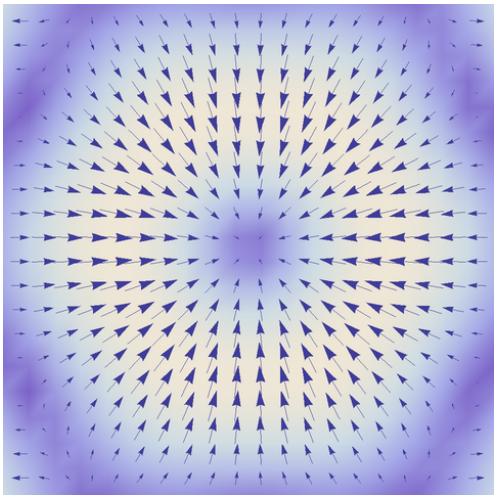

Figure 5.14: Magnetization for Rashba-like A_2 SDW order parameter 9 of the form $(\lambda_3-\sqrt{3}\lambda_8)\rho_y\sigma_y-\tau_z(\sqrt{3}\lambda_3+\lambda_8)\rho_y\sigma_x$. σ_v inverts x-component.

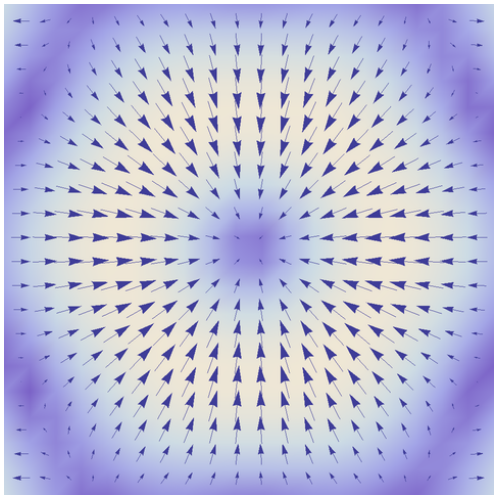

Figure 5.15: Magnetization for Rashba-like SDW order parameter 10 of the form $(-\sqrt{3}\lambda_1+\sqrt{3}\lambda_4)\rho_y\sigma_y-\tau_z(\lambda_1+\lambda_4-2\lambda_6)\rho_y\sigma_x$. σ_v inverts x-component.

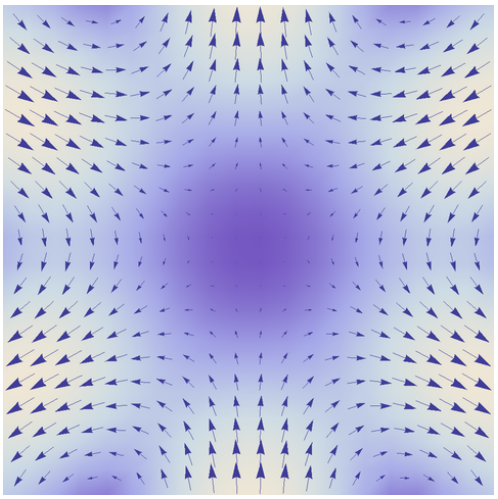

Figure 5.16: Magnetization for helicity-like A_2 SDW order parameter 11 of the form $\tau_z(\lambda_3-\sqrt{3}\lambda_8)\rho_x\sigma_x+(\sqrt{3}\lambda_3+\lambda_8)\rho_x\sigma_y$. σ_v inverts x-component.

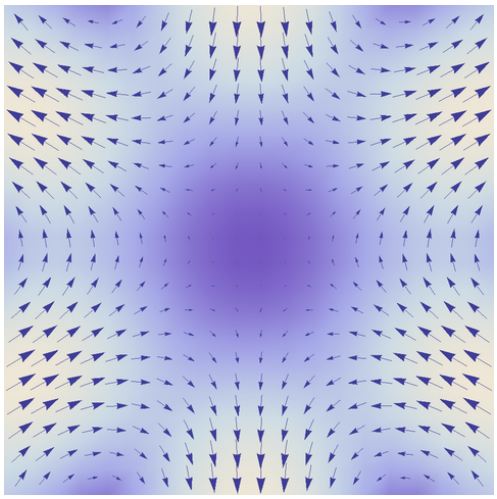

Figure 5.17: Magnetization for helicity-like A_2 SDW order parameter 12 of the form $\tau_z(-\sqrt{3}\lambda_1+\sqrt{3}\lambda_4)\rho_x\sigma_x+(\lambda_1+\lambda_4-2\lambda_6)\rho_x\sigma_y$. σ_v inverts x-component.

5.3 Spin density wave susceptibility calculations

In this section we compute susceptibilities for the SDW order parameters depending on different momentum transfers $\boldsymbol{Q}_{1,2,3}$. The spin density wave susceptibility describes the tendency of the system for the formation of density waves. The susceptibilities will peak for the favored momentum transfers. Since we choose the perfect nesting case we expect a peak for the nesting vector $\boldsymbol{Q}_1 = (2k_F, 0)$ where k_F is the Fermi momentum. Due to the C_{3v} symmetry the susceptibility should also show peaks for $\boldsymbol{Q}_2 = C_3\boldsymbol{Q}_1$ and $\boldsymbol{Q}_3 = C_3^2\boldsymbol{Q}_1$. There has been other work doing similar susceptibility computations without prior symmetry classification [44].

Our spinor and our order parameters are defined in $\tau \otimes \lambda \otimes \rho \otimes \sigma$ space. At first we define projectors on the subspaces that we use later in the calculations. In the λ space we get

$$\Pi_{\lambda=1} = 1 \oplus 0_2 \quad = \begin{pmatrix} 1 & 0 & 0 \\ 0 & 0 & 0 \\ 0 & 0 & 0 \end{pmatrix}, \tag{5.37}$$

$$\Pi_{\lambda=2} = 0 \oplus 1 \oplus 0 = \begin{pmatrix} 0 & 0 & 0 \\ 0 & 1 & 0 \\ 0 & 0 & 0 \end{pmatrix}, \tag{5.38}$$

$$\Pi_{\lambda=3} = 0_2 \oplus 1 \quad = \begin{pmatrix} 0 & 0 & 0 \\ 0 & 0 & 0 \\ 0 & 0 & 1 \end{pmatrix}. \tag{5.39}$$

For τ and ρ space we define similar projectors e.g.

$$\Pi_{\tau=+} = 1 \oplus 0 = \begin{pmatrix} 1 & 0 \\ 0 & 0 \end{pmatrix}, \quad \Pi_{\tau=-} = 0 \oplus 1 = \begin{pmatrix} 0 & 0 \\ 0 & 1 \end{pmatrix}. \tag{5.40}$$

We rewrite the Hamiltonian Eq. (5.14) in a way which is more appropriate to perform the susceptibility calculations. Since the Hamiltonian is diagonal in the τ, λ and ρ spaces we can indices to the Hamiltonian for each of the subspaces as follows

$$E^0_{\tau\lambda\rho}(\boldsymbol{k}) = E_0(\boldsymbol{k} + \rho\boldsymbol{Q}_\lambda/2)\tau \tag{5.41}$$

$$\begin{aligned} \widehat{\mathcal{H}}_{\tau\lambda\rho}(\boldsymbol{k}) &= E^0_{\tau\lambda\rho}(\boldsymbol{k}) + v_k(k_x\tau\sigma_y - k_y\sigma_x) + \frac{\Lambda}{2}\left(k_+^3 - k_-^3\right)\sigma_z \\ &= E^0_{\tau\lambda\rho}(\boldsymbol{k}) + \boldsymbol{g}_\tau(\boldsymbol{k})\cdot\boldsymbol{\sigma} \end{aligned} \tag{5.42}$$

where we introduced the vector $\boldsymbol{g}_\tau(\boldsymbol{k}) = \left(-v_k k_y, v_k\tau k_x, \Lambda\left(k_+^3 - k_-^3\right)/2\right)$ for simplicity of notation. The eigenvalues are given by

$$E_{\tau\lambda\rho\sigma}(\boldsymbol{k}) = E^0_{\tau\lambda\rho}(\boldsymbol{k}) + \sigma|\boldsymbol{g}_\tau(\boldsymbol{k})| = E_0(\boldsymbol{k} + \rho\boldsymbol{Q}_\lambda/2)\tau + \sigma|\boldsymbol{g}_\tau(\boldsymbol{k})|. \tag{5.43}$$

We determine the non-interacting Green's function $\widehat{G}^0_{\tau\lambda\rho}(\boldsymbol{k}, ik_n)$ by solving the equation

$$1 = [ik_n - \widehat{\mathcal{H}}_{\tau\lambda\rho}(\boldsymbol{k})]\widehat{G}^0_{\tau\lambda\rho}(\boldsymbol{k}, ik_n) \tag{5.44}$$

where $ik_n = (2n+1)\pi/\beta$ are fermionic Matsubara frequencies. We find

$$\widehat{G}^0_{\tau\lambda\rho}(\boldsymbol{k}, ik_n) = \frac{ik_n - E^0_{\tau\lambda\rho}(\boldsymbol{k}) + \boldsymbol{g}_\tau(\boldsymbol{k})\cdot\boldsymbol{\sigma}}{\left(ik_n - E^0_{\tau\lambda\rho}(\boldsymbol{k})\right)^2 + |\boldsymbol{g}_\tau(\boldsymbol{k})|^2}. \tag{5.45}$$

In the next step we split the Green's function into a sum using partial fractions and obtain two summands, one for each spin direction. We obtain

$$\begin{aligned}\widehat{G}^0_{\tau\lambda\rho}(\boldsymbol{k}, ik_n) &= \frac{1}{2|\boldsymbol{g}_\tau(\boldsymbol{k})|}\left[\frac{|\boldsymbol{g}_\tau(\boldsymbol{k})| + \boldsymbol{g}_\tau(\boldsymbol{k})\cdot\boldsymbol{\sigma}}{ik_n - E_{\tau\lambda\rho+}(\boldsymbol{k})} + \frac{|\boldsymbol{g}_\tau(\boldsymbol{k})| - \boldsymbol{g}_\tau(\boldsymbol{k})\cdot\boldsymbol{\sigma}}{ik_n - E_{\tau\lambda\rho-}(\boldsymbol{k})}\right] \\ &= \frac{\widehat{P}_{\tau+}(\boldsymbol{k})}{ik_n - E_{\tau\lambda\rho+}(\boldsymbol{k})} + \frac{\widehat{P}_{\tau-}(\boldsymbol{k})}{ik_n - E_{\tau\lambda\rho-}(\boldsymbol{k})}\end{aligned} \tag{5.46}$$

with the projectors

$$\widehat{P}_{\tau\sigma}(\boldsymbol{k}) = \frac{|\boldsymbol{g}_\tau(\boldsymbol{k})| + \sigma\boldsymbol{g}_\tau(\boldsymbol{k})\cdot\boldsymbol{\sigma}}{2|\boldsymbol{g}_\tau(\boldsymbol{k})|}\,. \tag{5.47}$$

By multiplication with the previously defined subspaces projectors we can extend the projectors $\widehat{P}_{\tau\sigma}(\boldsymbol{k})$ to act on the whole $\tau\otimes\lambda\otimes\rho\otimes\sigma$ space as follows

$$\widehat{P}_{\tau\lambda\rho\sigma} = \Pi_\tau \otimes \Pi_\lambda \otimes \Pi_\rho \otimes \widehat{P}_{\tau\sigma}\,. \tag{5.48}$$

We compute the susceptibility for the operators A and B by evaluating the Matsubara sum over the fermionic Matsubara frequencies ik_n and get

$$\begin{aligned}\chi^0_{AB}(\boldsymbol{q}, iq_n) &= -\frac{1}{V\beta}\int d\boldsymbol{k}\,\mathrm{Tr}\sum_{ik_n}\widehat{G}_0(\boldsymbol{k}, ik_n)\widehat{A}(\boldsymbol{k})\widehat{G}_0(\boldsymbol{k}+\boldsymbol{q}, ik_n+iq_n)\widehat{B}(\boldsymbol{k}+\boldsymbol{q}) \\ &= -\frac{1}{V\beta}\int d\boldsymbol{k}\,\mathrm{Tr}\sum_{ik_n}\sum_{\mu\nu}\frac{\widehat{P}_\mu(\boldsymbol{k})\widehat{A}(\boldsymbol{k})\widehat{P}_\nu(\boldsymbol{k}+\boldsymbol{q})\widehat{B}(\boldsymbol{k}+\boldsymbol{q})}{\left(ik_n - E_\mu(\boldsymbol{k})\right)\left(ik_n + iq_n - E_\nu(\boldsymbol{k}+\boldsymbol{q})\right)} \\ &= -\frac{1}{V}\int d\boldsymbol{k}\sum_{\mu\nu}\frac{n_F\left(E_\mu(\boldsymbol{k})\right) - n_F\left(E_\nu(\boldsymbol{k}+\boldsymbol{q})\right)}{iq_n + E_\mu(\boldsymbol{k}) - E_\nu(\boldsymbol{k}+\boldsymbol{q})}\,\mathrm{Tr}\left\{\widehat{P}_\mu(\boldsymbol{k})\widehat{A}(\boldsymbol{k})\widehat{P}_\nu(\boldsymbol{k}+\boldsymbol{q})\widehat{B}(\boldsymbol{k}+\boldsymbol{q})\right\}\end{aligned} \tag{5.49}$$

where $iq_n = 2n\pi/\beta$ is a bosonic Matsubara frequency. In our case the momentum transfer is included in the spinor. This means we set $\boldsymbol{Q}_1 = \boldsymbol{q}$ and the other wave vectors $\boldsymbol{Q}_{2,3}$ rotated by 120°. We get then

$$\chi^0_{AB}(\boldsymbol{q}, iq_n) = -\frac{1}{V}\int d\boldsymbol{k}\sum_{\mu\nu}\frac{n_F(E_\mu(\boldsymbol{k})) - n_F\left(E_\nu(\boldsymbol{k})\right)}{iq_n + E_\mu(\boldsymbol{k}) - E_\nu(\boldsymbol{k})}\,\mathrm{Tr}\left\{\widehat{P}_\mu(\boldsymbol{k})\widehat{A}(\boldsymbol{k})\widehat{P}_\nu(\boldsymbol{k})\widehat{B}(\boldsymbol{k})\right\}\,. \tag{5.50}$$

Now we add all the λ, ρ, τ and σ variables with an additional $1/2$ because of the τ double counting and obtain

$$\begin{aligned}\chi^0_{AB}(\boldsymbol{q}, iq_n) = -\frac{1}{2V}\int d\boldsymbol{k}\sum_{\tau\tau'}^{\pm}\sum_{\lambda\lambda'}^{1,2,3}\sum_{\rho\rho'}^{\pm}\sum_{\sigma\sigma'}^{\pm}&\frac{n_F\left(E_{\tau\lambda\rho\sigma}(\boldsymbol{k})\right) - n_F\left(E_{\tau'\lambda'\rho'\sigma'}(\boldsymbol{k})\right)}{iq_n + E_{\tau\lambda\rho\sigma}(\boldsymbol{k}) - E_{\tau'\lambda'\rho'\sigma'}(\boldsymbol{k})} \\ &\times\mathrm{Tr}\left\{\widehat{P}_{\tau\lambda\rho\sigma}(\boldsymbol{k})\widehat{A}(\boldsymbol{k})\widehat{P}_{\tau'\lambda'\rho'\sigma'}(\boldsymbol{k})\widehat{B}(\boldsymbol{k})\right\}\,.\end{aligned} \tag{5.51}$$

We evaluate the susceptibilities at $T = 1\,\mathrm{K}$ using Mathematica and integration in a small C program. The plots for the susceptibilities are shown in Figs. 5.18 to 5.22. For the order parameters 3, 5, 9 and 11 we find peaks at $\boldsymbol{Q}_1 = (2k_F, 0)$ where k_F is the Fermi momentum. This means that we found the favored momentum transfer which was suggested by the Fermi surface nesting. For further determination of the favored order parameter it is necessary to perform a Ginzburg-Landau theory or to solve microscopic self-consistency equations.

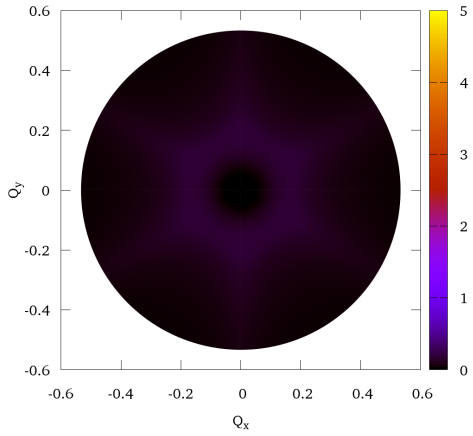

(a) Susceptibility(2D projection)

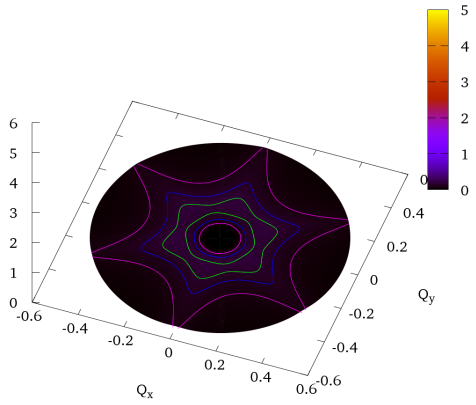

(b) Susceptibility along z-direction

Figure 5.18: $\boldsymbol{Q}_1$ dependent susceptibilities for Ising-like SDW order parameters 1 and 7 of the form $\tau_z\rho_{y,x}\sigma_z$

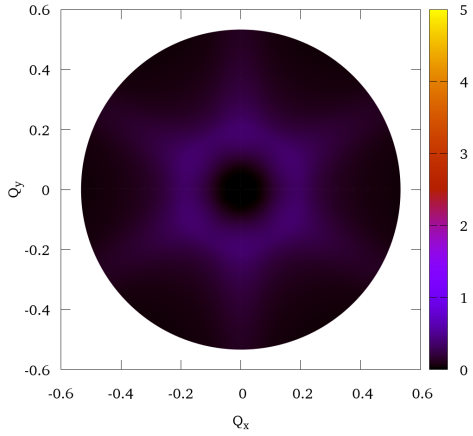

(c) Susceptibility(2D projection)

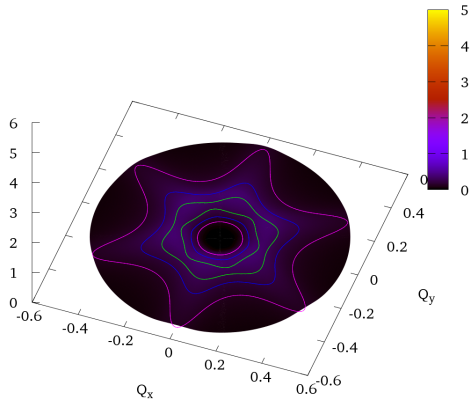

(d) Susceptibility along z-direction

Figure 5.19: $\boldsymbol{Q}_1$ dependent susceptibilities for Ising-like SDW order parameters 2 and 8 of the form $\tau_z(\lambda_1+\lambda_4+\lambda_6)\rho_{y,x}\sigma_z$

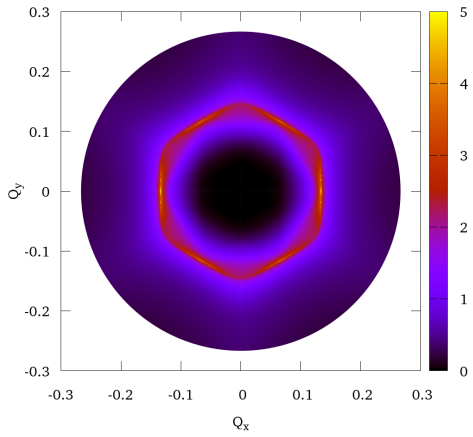

(a) Susceptibility(2D projection)

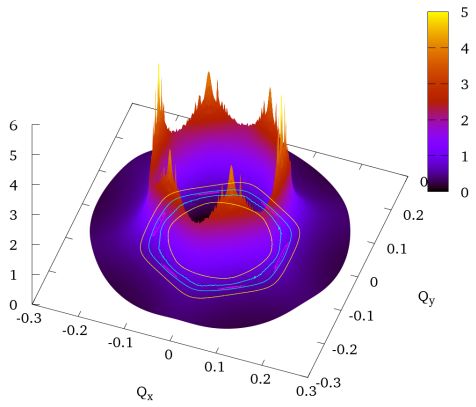

(b) Susceptibility along z-direction

Figure 5.20: $\boldsymbol{Q}_1$ dependent susceptibilities for Rashba-like SDW order parameters 3 and 9 of the form $(\lambda_3-\sqrt{3}\lambda_8)\rho_{x,y}\sigma_y-\tau_z(\sqrt{3}\lambda_3+\lambda_8)\rho_{x,y}\sigma_x$. The susceptibility peaks for $\boldsymbol{Q}_1=(2k_F,0)$, $\boldsymbol{Q}_2=C_3\boldsymbol{Q}_1$ and $\boldsymbol{Q}_3=C_3\boldsymbol{Q}_2$.

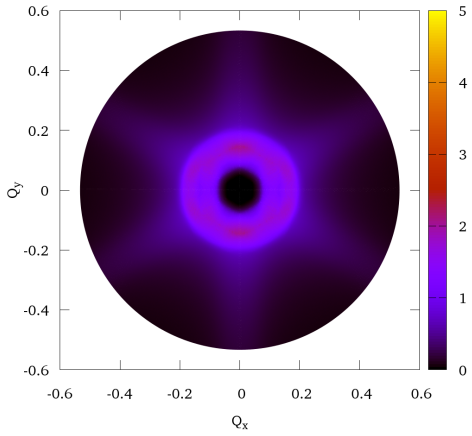

(a) Susceptibility(2D projection)

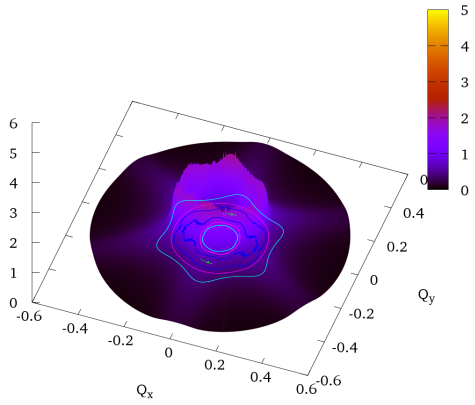

(b) Susceptibility along z-direction

Figure 5.21: $\boldsymbol{Q}_1$ dependent susceptibilities for Rashba-like SDW order parameters 4 and 10 of the form $(-\sqrt{3}\lambda_1+\sqrt{3}\lambda_4)\rho_{x,y}\sigma_y-\tau_z(\lambda_1+\lambda_4-2\lambda_6)\rho_{x,y}\sigma_x$.

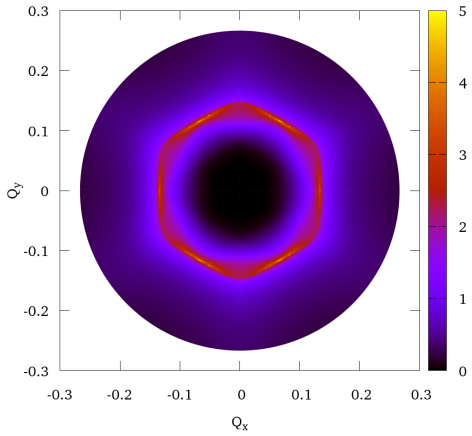

(c) Susceptibility color encodes

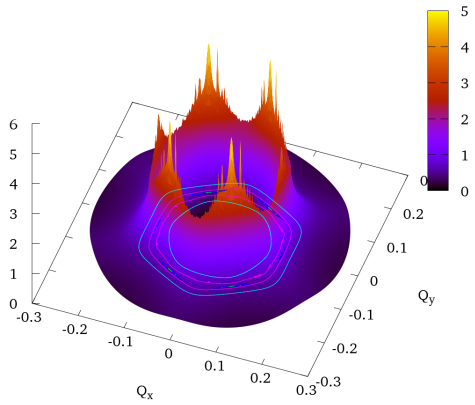

(d) Susceptibility along z-direction

Figure 5.22: $\boldsymbol{Q}_1$ dependent susceptibilities for helicity-like SDW order parameters 5 and 11 of the form $\tau_z(\lambda_3-\sqrt{3}\lambda_8)\rho_{y,x}\sigma_x+(\sqrt{3}\lambda_3+\lambda_8)\rho_{y,x}\sigma_y$. The susceptibility peaks for $\boldsymbol{Q}_1=(2k_F,0)$, $\boldsymbol{Q}_2=C_3\boldsymbol{Q}_1$ and $\boldsymbol{Q}_3=C_3\boldsymbol{Q}_2$.

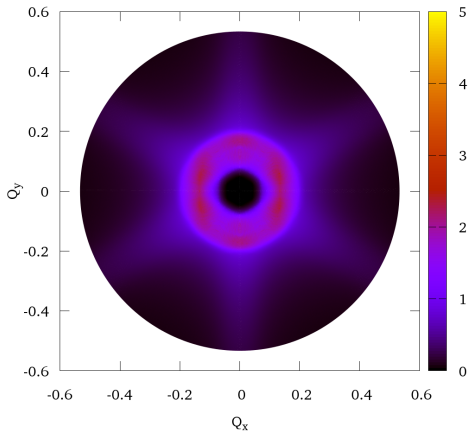

(a) Susceptibility(2D projection)

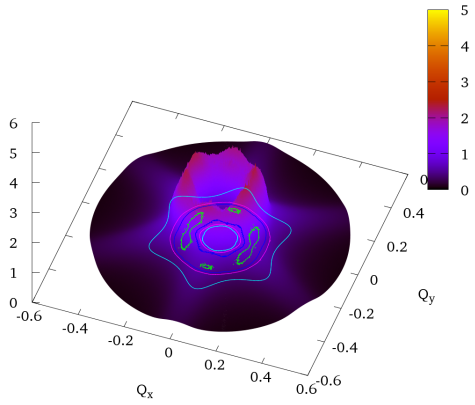

(b) Susceptibility along z-direction

Figure 5.23: $\boldsymbol{Q}_1$ dependent susceptibilities for helicity-like SDW order parameters 6 and 12 of the form $\tau_z(-\sqrt{3}\lambda_1+\sqrt{3}\lambda_4)\rho_{y,x}\sigma_x+(\lambda_1+\lambda_4-2\lambda_6)\rho_{y,x}\sigma_y$.

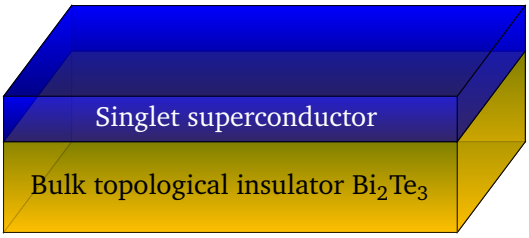

(a) Superconductor placed on top of Bi_2Te_3

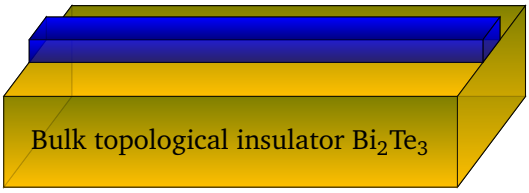

(b) Superconducting nanowire on top of bulk topological insulator

Figure 5.24: Heterostructures

5.4 Coexistence of spin density waves and superconductivity

It has been proposed that topological superconductors can be constructed by placing a s-wave superconductor on top of a 3D topological insulator as in the schematic Fig. 5.24a [42]. Similarly in our case the superconducting proximity effect will add a term to the effective surface Hamiltonian which is then given by

$$\widehat{\mathcal{H}}_{\mathrm{SDW+SC}}(\boldsymbol{k}) = \widehat{\mathcal{H}}(\boldsymbol{k}) - M_{\mathrm{SDW}} - \Delta\tau_y\sigma_y\,. \tag{5.52}$$

where $\Delta = |\Delta|e^{i\phi}$ with $\phi = 0$ is the superconducting gap parameter. The mechanism for this proximity effect needs further investigation. In this work we just assume the existence of correlations leading to the additional term in the Hamiltonian. In our case we want to investigate the coexisting spin density wave and superconductivity phases, therefore we included one spin density wave order parameter M_{SDW} in the Hamiltonian. The only symmetry of the resulting Hamiltonian $\widehat{\mathcal{H}}_{\mathrm{SDW+SC}}(\boldsymbol{k})$ is the generalized charge conjugation symmetry $\Xi = \tau_x\mathcal{K}$ which squares to one. Since $\Xi^2 = \mathbb{1}$ the system belongs to the BdG class D. Depending on the parameter M_{SDW} we might be able to block diagonalize in λ and get multiple class D systems. If we use $M_{\mathrm{SDW}} = M\left((\lambda_3 - \sqrt{3}\lambda_8)\rho_x\sigma_y - \tau_z(\sqrt{3}\lambda_3 + \lambda_8)\rho_x\sigma_x\right)$ as a spin density wave order parameter the system is block diagonal in λ space and we obtain three class D systems with eight bands each as shown in Fig. 5.25 around $\boldsymbol{k} = 0$. For a certain value of the superconducting gap Δ the three systems will be in a topologically non-trivial phase. If we tune the parameter M the three subsystems transit from topologically trivial to topologically non-trivial phase. Fig. 5.26 shows the qualitative numeric solutions for the two inner bands for each of the three subsystems at the point of the topological phase transition. The point of the topological phase transition is specified by the occurrence of gap closings. The exact phase diagram and the analytic relation between M and Δ require further investigations. In the topological phase the topological superconductor hosts Majorana modes. Specific setups like a superconducting nanowire on top of the 3D topological insulators as in Fig. 5.24b lead to Majorana bound states at the edges of the wire. Majorana bound states at the edges of nanowires can be used for braiding operations as demonstrated in [16]. Such a system could finally lead to the construction of a topological quantum computer. Due to the C_{3v} symmetry and the existence of three subsystems the topological insulator Bi_2Te_3 might offer interesting properties.

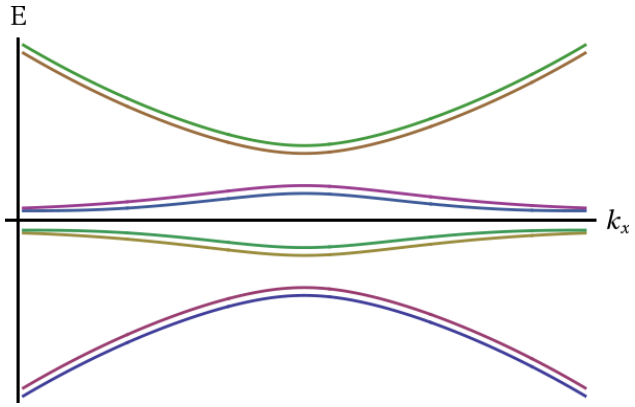

Figure 5.25: Eight bands of the three subsystems around the Γ point

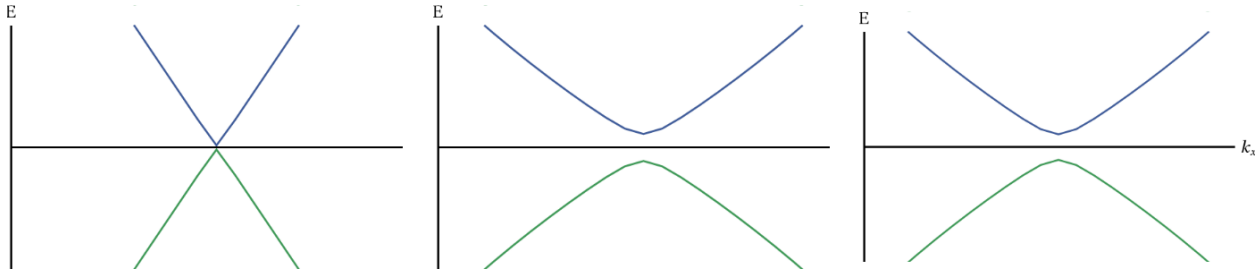

(a) For a certain M the first one subsystem transits into the topologically non-trivial phase. The gap closing marks the point of the topological phase transition.

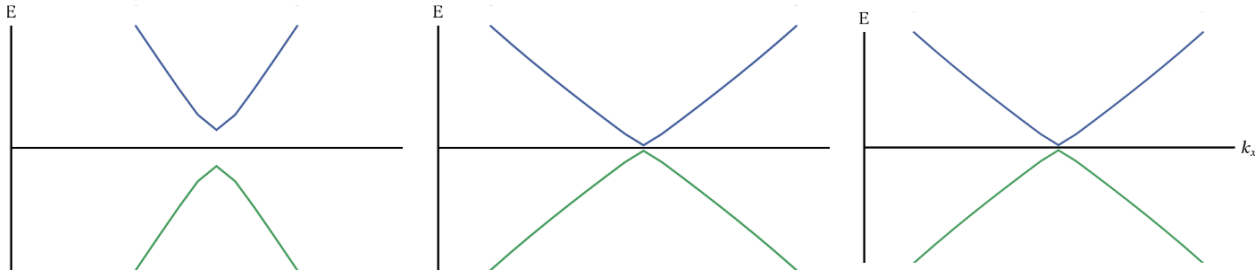

(b) For larger M the other two subsystem transit into the topologically non-trivial phase. The gap closing marks the point of the topological phase transition.

Figure 5.26: Lowest two bands around the Γ point for the three subsystems for different values of the spin density wave order parameter M

Chapter 6

Conclusions and outlook

In this chapter we shortly summarize the main results of the thesis and discuss further work.

6.1 Results

In this thesis we performed an exhaustive classification of order parameters for systems exhibiting coexistence of superconductivity and density waves with an commensurate wave vector. We focused on the point group D_{4h} for the classification. We found general results concerning the symmetry transformations inversion transformation $\mathcal{I}$, time reversal transformation $\mathcal{T}$, charge conjugation transformation $\mathcal{C}$ and point group transformations. The classification also includes an investigation of a possible symmetry breaking scheme of the point group.

Furthermore we performed an exhaustive investigation for all possible 2×2 and 4×4 Hamiltonians using the generalized symmetries: time reversal symmetry Θ, charge conjugation symmetry Ξ and chiral symmetry Π. These generalized symmetries determine the symmetry class the Hamiltonian belongs to. The symmetry class is directly connected to the topological properties of the system. It determines if a system can exhibit $\mathbb{Z}$ or $\mathbb{Z}_2$ topological invariants. For the 4×4 Hamiltonians we find four distinct cases depending on the algebraic properties of the terms occurring in the Hamiltonian. These results can be used as a basis for further investigations concerning topological systems. The results allow the construction of Hamiltonians with desired properties thus allowing the construction of models explaining phenomenological effects which were observed in experiments.

We applied our symmetry and topological analysis to two systems which exhibit density waves. In the first phase of this thesis we analyzed a topological density wave model which exhibits a rich phase diagram. The model was constructed from various density wave terms which have been proposed for different materials e.g. the cuprates. Another system we discussed were the surface modes of Bi_2Te_3. The Bi_2Te_3 surface modes show a characteristically warped Fermi surface with a C_{3v} symmetry. We investigated the possibilities for spin density waves in the perfect nesting case and performed a symmetry classification of spin density wave order parameters using the point group C_{3v}. For each of the order parameters we performed an analysis of the magnetic order and the susceptibilities. After that we studied the occurrence of Majorana modes when superconductivity is induced by proximity effects, e.g. by an s-wave superconductor which is placed on top of the 3D topological insulator Bi_2Te_3. We found that the surface modes can be in a topologically trivial and non-trivial phase. The non-trivial phase exhibits Majorana modes. This could be used to construct systems which host Majorana bound states for example at the edges of a a nanowire. The Majorana bound states can be used as building blocks for topological quantum computation. It is also important to mention that characteristic properties of Majorana systems can be used to propose setups to demonstrate the existence of Majorana states in condensed matter systems.

6.2 Further work

This thesis describes the work that we performed over the last year. Our work had different directions. Concerning the general work the symmetry classification of Hamiltonians requires further analysis and generalization to higher dimensions. Further investigations are necessary in the field of weak topological invariants which are not covered in detail by the periodic table of topological insulators.

Concerning the Bi_2Te_3 system there are multiple perspectives for further work. At first the susceptibility calculations for the spin density wave order parameters have to be performed in a random phase approximation. Using a Ginzburg-Landau theory or a microscopic self-consistent analysis we plan to explore the thermodynamic phase diagram of the system for coexisting density waves and superconductivity. This will allow us to analyze the topological phase diagram of the system also more in detail. Finally we want to continue our studies on the superconducting proximity effect and its microscopic mechanism.

Appendix A

Symmetry breaking scheme of the point group D_{4h}

In this appendix we shown the symmetry breaking of the point group D_{4h} if different representations of the group D_{4h} are added. The resulting expression belongs then to a representation of a subgroup of the D_{4h}. Such a case could occur for example in a Hamiltonian which is a sum one-dimensional representations of the symmetry group of the system. The reason for the symmetry breaking is that different representations show different behavior for a group operation. The resulting expression is then not invariant anymore under this group operation effectively breaking the symmetry to a subgroup. For example the representations A_{1g} (even) and A_{1u} (odd) behave differently under inversion $\mathcal{I}$. The resulting representation $A_1 = A_{1g} + A_{1u}$ belongs to the subgroup D_4. A more physical interesting example is a Hamiltonian with Rashba vs. helicity terms

$$\widehat{\mathcal{H}}_{\text{Rashba}}(\boldsymbol{k}) = \underbrace{\frac{\boldsymbol{k}^2}{2m}}_{A_{1g}} + v \underbrace{k_z \left(k_x \sigma_y - k_y \sigma_x\right)}_{A_{1g}}, \tag{A.1}$$

$$\widehat{\mathcal{H}}_{\text{Helicity}}(\boldsymbol{k}) = \underbrace{\frac{\boldsymbol{k}^2}{2m}}_{A_{1g}} + v \underbrace{k_z \left(k_x \sigma_x + k_y \sigma_y\right)}_{A_{2g}} \tag{A.2}$$

where the Hamiltonian with the helicity term breaks the rotation symmetries $2C_2'$ and $2C_2''$ effectively rendering the Hamiltonian only C_{4h} invariant. In contrast the Rashba Hamiltonian stays D_{4h} invariant.

The later tables show all the possible breakings of the point group D_{4h} when two, three or four different representations are added. Five different representations will always break the point group to C_2. Especially interesting is that there are cases when D_{4h} can break in two different ways. These two cases are marked with red and blue color respectively in the table. It is also important to mention that not all representations of the subgroups can be reached. Some subgroups can therefore not be reached at all. In this case the group C_s which consists only of the σ_v operation and C_i which only consists of the inversion operation $\mathcal{I}$ cannot be reached.

Table A.1: Character table of the point group D_{4h}

I.R.	E	$2C_4$	C_2	$2C_2'$	$2C_2''$	$\mathcal{I}$	$2S_4$	σ_h	$2\sigma_v$	$2\sigma_d$	Linear, Rotations	Higher functions
A_{1g}	+1	+1	+1	+1	+1	+1	+1	+1	+1	+1		x^2+y^2, z^2
A_{2g}	+1	+1	+1	−1	−1	+1	+1	+1	−1	−1	R_z	$xy(x^2-y^2)$
B_{1g}	+1	−1	+1	+1	−1	+1	−1	+1	+1	−1		x^2-y^2
B_{2g}	+1	−1	+1	−1	+1	+1	−1	+1	−1	+1		xy
E_g	+2	0	−2	0	0	+2	0	−2	0	0	(R_x, R_y)	(xz, yz)
A_{1u}	+1	+1	+1	+1	+1	−1	−1	−1	−1	−1		$xyz(x^2-y^2)$
A_{2u}	+1	+1	+1	−1	−1	−1	−1	−1	+1	+1	z	
B_{1u}	+1	−1	+1	+1	−1	−1	+1	−1	−1	+1		xyz
B_{2u}	+1	−1	+1	−1	+1	−1	+1	−1	+1	−1		$z(x^2-y^2)$
E_u	+2	0	−2	0	0	−2	0	+2	0	0	(x, y)	

Table A.2: Symmetry breaking of the point group D_{4h} if two different irreducible representations are added

D_{4h} I.R.			Subgroup		E	$2C_4$	C_2	$2C_2'$	$2C_2''$	$\mathcal{I}$	$2S_4$	σ_h	$2\sigma_v$	$2\sigma_d$
A_{1g}	+	A_{1u}	D_4	A_1	+1	+1	+1	+1	+1					
A_{2g}	+	A_{2u}		A_2	+1	+1	+1	−1	−1					
B_{1g}	+	B_{1u}		B_1	+1	−1	+1	+1	−1					
B_{2g}	+	B_{2u}		B_2	+1	−1	+1	−1	+1					
E_g	+	E_u		E	+2	0	−2	0	0					
A_{1g}	+	B_{1g}	D_{2h}	A_g	+1		+1	+1		+1		+1	+1	
A_{1u}	+	B_{1u}		A_u	+1		+1	+1		−1		−1	−1	
A_{2g}	+	B_{2g}		B_{1g}	+1		+1	−1		+1		+1	−1	
A_{2u}	+	B_{2u}		B_{1u}	+1		+1	−1		−1		−1	+1	
A_{1g}	+	B_{2g}		A_g	+1		+1		+1	+1		+1		+1
A_{1u}	+	B_{2u}		A_u	+1		+1		+1	−1		−1		−1
A_{2g}	+	B_{1g}		B_{1g}	+1		+1		−1	+1		+1		−1
A_{2u}	+	B_{1u}		B_{1u}	+1		+1		−1	−1		−1		+1
A_{1g}	+	B_{1u}	D_{2d}	A_1	+1		+1	+1			+1			+1
A_{2g}	+	B_{2u}		A_2	+1		+1	−1			+1			−1
B_{1g}	+	A_{1u}		B_1	+1		+1	+1			−1			−1
B_{2g}	+	A_{2u}		B_2	+1		+1	−1			−1			+1
A_{1g}	+	B_{2u}		A_1	+1		+1		+1		+1		+1	
A_{2g}	+	B_{1u}		A_2	+1		+1		−1		+1		−1	
B_{2g}	+	A_{1u}		B_1	+1		+1		+1		−1		−1	
B_{1g}	+	A_{2u}		B_2	+1		+1		−1		−1		+1	
E_g	+	E_u		E	+2	0	−2	0			0			
A_{1g}	+	A_{2g}	C_{4h}	A_g	+1	+1	+1			+1	+1	+1		
B_{1g}	+	B_{2g}		B_g	+1	−1	+1			+1	−1	+1		
A_{1u}	+	A_{2u}		A_u	+1	+1	+1			−1	−1	−1		
B_{1u}	+	B_{2u}		B_u	+1	−1	+1			−1	+1	−1		
A_{1g}	+	A_{2u}	C_{4v}	A_1	+1	+1	+1						+1	+1
A_{2g}	+	A_{1u}		A_2	+1	+1	+1						−1	−1
B_{1g}	+	B_{2u}		B_1	+1	−1	+1						+1	−1
B_{2g}	+	B_{1u}		B_2	+1	−1	+1						−1	+1
E_g	+	E_u		E	+2	0	−2						0	0

Table A.3: Symmetry breaking of the point group D_{4h} if three different irreducible representations are added

D_{4h} I.R.					Subgroup		E	$2C_4$	C_2	$2C_2'$	$2C_2''$	$\mathcal{I}$	$2S_4$	σ_h	$2\sigma_v$	$2\sigma_d$
A_{1g}	+	B_{2g}	+	A_{1u}	D_2	A	+1		+1		+1					
A_{1g}	+	B_{2g}	+	B_{2u}		A	+1		+1		+1					
A_{1g}	+	A_{1u}	+	B_{2u}		A	+1		+1		+1					
B_{2g}	+	A_{1u}	+	B_{2u}		A	+1		+1		+1					
A_{2g}	+	B_{1g}	+	B_{1u}		B_1	+1		+1		−1					
A_{2g}	+	A_{2u}	+	B_{1u}		B_1	+1		+1		−1					
A_{2g}	+	B_{1g}	+	A_{2u}		B_1	+1		+1		−1					
B_{1g}	+	A_{2u}	+	B_{1u}		B_1	+1		+1		−1					
A_{1g}	+	B_{1g}	+	A_{1u}		A	+1		+1	+1						
A_{1g}	+	B_{1g}	+	B_{1u}		A	+1		+1	+1						
A_{1g}	+	A_{1u}	+	B_{1u}		A	+1		+1	+1						
B_{1g}	+	A_{1u}	+	B_{1u}		A	+1		+1	+1						
A_{2g}	+	B_{2g}	+	B_{2u}		B_1	+1		+1	−1						
A_{2g}	+	B_{2g}	+	A_{2u}		B_1	+1		+1	−1						
A_{2g}	+	A_{2u}	+	B_{2u}		B_1	+1		+1	−1						
B_{2g}	+	A_{2u}	+	B_{2u}		B_1	+1		+1	−1						
A_{1g}	+	A_{1u}	+	A_{2u}	C_4	A	+1	+1	+1							
A_{2g}	+	A_{1u}	+	A_{2u}		A	+1	+1	+1							
A_{1g}	+	A_{2g}	+	A_{1u}		A	+1	+1	+1							
A_{1g}	+	A_{2g}	+	A_{2u}		A	+1	+1	+1							
B_{1g}	+	B_{1u}	+	B_{2u}		B	+1	−1	+1							
B_{2g}	+	B_{1u}	+	B_{2u}		B	+1	−1	+1							
B_{1g}	+	B_{2g}	+	B_{2u}		B	+1	−1	+1							
B_{1g}	+	B_{2g}	+	B_{1u}		B	+1	−1	+1							
A_{2g}	+	B_{1g}	+	B_{2g}	C_{2h}	A_g	+1		+1			+1		+1		
A_{1g}	+	B_{1g}	+	B_{2g}		A_g	+1		+1			+1		+1		
A_{1g}	+	A_{2g}	+	B_{2g}		A_g	+1		+1			+1		+1		
A_{1g}	+	A_{2g}	+	B_{1g}		A_g	+1		+1			+1		+1		
A_{2u}	+	B_{1u}	+	B_{2u}		A_u	+1		+1			−1		−1		
A_{1u}	+	B_{1u}	+	B_{2u}		A_u	+1		+1			−1		−1		
A_{1u}	+	A_{2u}	+	B_{1u}		A_u	+1		+1			−1		−1		
A_{1u}	+	A_{2u}	+	B_{2u}		A_u	+1		+1			−1		−1		
A_{1g}	+	B_{2g}	+	B_{1u}	C_{2v}	A_1	+1		+1							+1
A_{1g}	+	A_{2u}	+	B_{1u}		A_1	+1		+1							+1
A_{1g}	+	B_{2g}	+	A_{2u}		A_1	+1		+1							+1
B_{2g}	+	A_{2u}	+	B_{1u}		A_1	+1		+1							+1
B_{1g}	+	A_{1u}	+	B_{2u}		A_2	+1		+1							−1
A_{2g}	+	A_{1u}	+	B_{2u}		A_2	+1		+1							−1
A_{2g}	+	B_{1g}	+	A_{1u}		A_2	+1		+1							−1
A_{2g}	+	B_{1g}	+	B_{2u}		A_2	+1		+1							−1
B_{1g}	+	A_{2u}	+	B_{2u}		A_1	+1		+1						+1	
A_{1g}	+	B_{1g}	+	A_{2u}		A_1	+1		+1						+1	
A_{1g}	+	B_{1g}	+	B_{2u}		A_1	+1		+1						+1	
A_{1g}	+	A_{2u}	+	B_{2u}		A_1	+1		+1						+1	
A_{2g}	+	B_{2g}	+	B_{1u}		A_2	+1		+1						−1	
A_{2g}	+	B_{2g}	+	A_{1u}		A_2	+1		+1						−1	
A_{2g}	+	A_{1u}	+	B_{1u}		A_2	+1		+1						−1	
B_{2g}	+	A_{1u}	+	B_{1u}		A_2	+1		+1						−1	
A_{1g}	+	A_{2g}	+	B_{1u}	S_4	A	+1		+1				+1			
A_{1g}	+	A_{2g}	+	B_{2u}		A	+1		+1				+1			
A_{2g}	+	B_{1u}	+	B_{2u}		A	+1		+1				+1			
A_{1g}	+	B_{1u}	+	B_{2u}		A	+1		+1				+1			
B_{1g}	+	B_{2g}	+	A_{2u}		B	+1		+1				−1			
B_{1g}	+	B_{2g}	+	A_{1u}		B	+1		+1				−1			
B_{1g}	+	A_{1u}	+	A_{2u}		B	+1		+1				−1			
B_{2g}	+	A_{1u}	+	A_{2u}		B	+1		+1				−1			

Table A.4: Symmetry breaking of the point group D_{4h} if four different irreducible representations are added. The cases which break down to C_2 are omitted.

D_{4h} I.R.							Subgroup		E	$2C_4$	C_2	$2C_2'$	$2C_2''$	$\mathcal{I}$	$2S_4$	σ_h	$2\sigma_v$	$2\sigma_d$
A_{1g}	+	B_{2g}	+	A_{1u}	+	B_{2u}	D_2	A	+1		+1		+1					
A_{2g}	+	B_{1g}	+	A_{2u}	+	B_{1u}		B_1	+1		+1		−1					
A_{1g}	+	B_{1g}	+	A_{1u}	+	B_{1u}		A	+1		+1	+1						
A_{2g}	+	B_{2g}	+	A_{2u}	+	B_{2u}		B_1	+1		+1	−1						
A_{1g}	+	A_{2g}	+	A_{1u}	+	A_{2u}	C_4	A	+1	+1	+1							
B_{1g}	+	B_{2g}	+	B_{1u}	+	B_{2u}		B	+1	−1	+1							
A_{1g}	+	A_{2g}	+	B_{1g}	+	B_{2g}	C_{2h}	A_g	+1		+1			+1		+1		
A_{1u}	+	A_{2u}	+	B_{1u}	+	B_{2u}		A_u	+1		+1			−1		−1		
A_{1g}	+	B_{2g}	+	A_{2u}	+	B_{1u}	C_{2v}	A_1	+1		+1							+1
A_{2g}	+	B_{1g}	+	A_{1u}	+	B_{2u}		A_2	+1		+1							−1
A_{1g}	+	B_{1g}	+	A_{2u}	+	B_{2u}		A_1	+1		+1						+1	
A_{2g}	+	B_{2g}	+	A_{1u}	+	B_{1u}		A_2	+1		+1						−1	
A_{1g}	+	A_{2g}	+	B_{1u}	+	B_{2u}	S_4	A	+1		+1				+1			
B_{1g}	+	B_{2g}	+	A_{1u}	+	A_{2u}		B	+1		+1				−1			

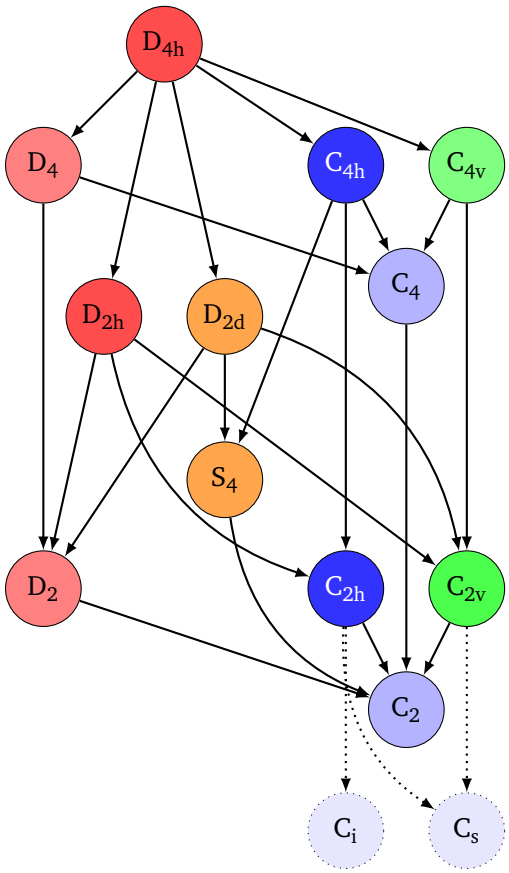

Figure A.1: All subgroups of the point group D_{4h}. The arrows correspond to a breaking of the symmetry to a subgroup. The subgroups C_s and C_i cannot be reached by the discussed symmetry breaking scheme.

Appendix B

Classification for $Q = (\pi, \pi, 0)$

We show a classification of order parameters for systems with one commensurate wave vector $\boldsymbol{Q} = (\pi, \pi, 0)$. The symmetry classification for $\mathcal{I}$, $\mathcal{T}$ and $t_{\boldsymbol{Q}}$ coincides with the classification for the system with $\boldsymbol{Q} = (\pi, \pi, \pi)$ but the basis functions differ.

Table B.1: Classifying the singlet generators which carry the A_{1g} representation

Generator	q	$\boldsymbol{p}$	$\mathcal{T}$	$\mathcal{I}$	$t_{\boldsymbol{Q}}$	I.R.	Representative basis functions
τ_z	0	$\mathbf{0}$	$+$	$+$	$+$	A_{1g}	$1, \cos k_z, \cos k_x \cos k_y, \cos 2k_x + \cos 2k_y$
$\tau_z\rho_x$	0	$\boldsymbol{Q}$	$+$			A_{2g}	$\sin k_x \sin k_y (\cos 2k_x - \cos 2k_y)$
$\tau_y\sigma_y$	$2e$	$\mathbf{0}$	$+$			B_{1g}	$\cos 2k_x - \cos 2k_y$
$\tau_x\sigma_y$	$2e$	$\mathbf{0}$	$-$			B_{2g}	$\sin k_x \sin k_y$
$\tau_y\rho_x\sigma_y$	$2e$	$\boldsymbol{Q}$	$+$				
$\tau_x\rho_x\sigma_y$	$2e$	$\boldsymbol{Q}$	$-$				
$\tau_z\rho_z$	0	$\mathbf{0}$	$+$	$+$	$-$	A_{1g}	$\cos k_x + \cos k_y$
ρ_y	0	$\boldsymbol{Q}$	$-$			A_{2g}	$\sin k_x \sin k_y (\cos k_x - \cos k_y)$
$\tau_y\rho_z\sigma_y$	$2e$	$\mathbf{0}$	$+$			B_{1g}	$\cos k_x - \cos k_y$
$\tau_x\rho_z\sigma_y$	$2e$	$\mathbf{0}$	$-$			B_{2g}	$\sin k_x \sin k_y (\cos k_x + \cos k_y)$
ρ_x	0	$\boldsymbol{Q}$	$-$	$-$	$+$	A_{1u}	$\sin k_x \sin k_y \sin k_z (\cos 2k_x - \cos 2k_y)$
						A_{2u}	$\sin k_z$
						B_{1u}	$\sin k_x \sin k_y \sin k_z$
						B_{2u}	$\sin k_z (\cos 2k_x - \cos 2k_y)$
ρ_z	0	$\mathbf{0}$	$-$	$-$	$-$	A_{1u}	$\sin k_x \sin k_y \sin k_z (\cos k_x - \cos k_y)$
$\tau_z\rho_y$	0	$\boldsymbol{Q}$	$+$			A_{2u}	$\sin k_z (\cos k_x + \cos k_y)$
$\tau_y\rho_y\sigma_y$	$2e$	$\boldsymbol{Q}$	$+$			B_{1u}	$\sin k_x \sin k_y \sin k_z (\cos k_x + \cos k_y)$
$\tau_x\rho_y\sigma_y$	$2e$	$\boldsymbol{Q}$	$-$			B_{2u}	$\sin k_z (\cos k_x - \cos k_y)$

Table B.2: Classifying the triplet generators in the z-direction which carry the A_{2g} representation

Generator	q	$\boldsymbol{p}$	$\mathcal{T}$	$\mathcal{I}$	$t_{\boldsymbol{Q}}$	Rep.	Representative basis functions
$\tau_z\tilde{\sigma}_z$	0	$\boldsymbol{0}$	$-$	$+$	$+$	A_{1g}	$\sin k_x \sin k_y(\cos 2k_x - \cos 2k_y)$
$\tau_z\rho_x\tilde{\sigma}_z$	0	$\boldsymbol{Q}$	$-$			A_{2g}	$1, \cos k_z, \cos k_x \cos k_y, \cos 2k_x + \cos 2k_y$
						B_{1g}	$\sin k_x \sin k_y$
						B_{2g}	$\cos 2k_x - \cos 2k_y$
$\tau_z\rho_z\tilde{\sigma}_z$	0	$\boldsymbol{0}$	$-$	$+$	$-$	A_{1g}	$\sin k_x \sin k_y(\cos k_x - \cos k_y)$
$\rho_y\tilde{\sigma}_z$	0	$\boldsymbol{Q}$	$+$			A_{2g}	$\cos k_x + \cos k_y$
$\tau_x\rho_y i\sigma_y\tilde{\sigma}_z$	$2e$	$\boldsymbol{Q}$	$+$			B_{1g}	$\sin k_x \sin k_y(\cos k_x + \cos k_y)$
$\tau_y\rho_y i\sigma_y\tilde{\sigma}_z$	$2e$	$\boldsymbol{Q}$	$-$			B_{2g}	$\cos k_x - \cos k_y$
$\tilde{\sigma}_z$	0	$\boldsymbol{0}$	$+$	$-$	$+$	A_{1u}	$\sin k_z$
$\rho_x\tilde{\sigma}_z$	0	$\boldsymbol{Q}$	$+$			A_{2u}	$\sin k_x \sin k_y \sin k_z(\cos k_x - \cos k_y)$
$\tau_y i\sigma_y\tilde{\sigma}_z$	$2e$	$\boldsymbol{0}$	$-$			B_{1u}	$\sin k_z(\cos 2k_x - \cos 2k_y)$
$\tau_x i\sigma_y\tilde{\sigma}_z$	$2e$	$\boldsymbol{0}$	$+$			B_{2u}	$\sin k_x \sin k_y \sin k_z$
$\tau_x\rho_x i\sigma_y\tilde{\sigma}_z$	$2e$	$\boldsymbol{Q}$	$+$				
$\tau_y\rho_x i\sigma_y\tilde{\sigma}_z$	$2e$	$\boldsymbol{Q}$	$-$				
$\rho_z\tilde{\sigma}_z$	0	$\boldsymbol{0}$	$+$	$-$	$-$	A_{1u}	$\sin k_z(\cos k_x + \cos k_y)$
$\tau_z\rho_y\tilde{\sigma}_z$	0	$\boldsymbol{Q}$	$-$			A_{2u}	$\sin k_x \sin k_y \sin k_z(\cos k_x - \cos k_y)$
$\tau_x\rho_z i\sigma_y\tilde{\sigma}_z$	$2e$	$\boldsymbol{0}$	$+$			B_{1u}	$\sin k_z(\cos k_x - \cos k_y)$
$\tau_y\rho_z i\sigma_y\tilde{\sigma}_z$	$2e$	$\boldsymbol{0}$	$-$			B_{2u}	$\sin k_x \sin k_y \sin k_z(\cos k_x + \cos k_y)$

Table B.3: Classifying the triplet generators in the x- and y-direction which carry the E_g representation

Generator	q	$\boldsymbol{p}$	$\mathcal{T}$	$\mathcal{I}$	$t_{\boldsymbol{Q}}$	I.R.	Representative basis functions
$\tau_z\tilde{\boldsymbol{\sigma}}_{xy}$	0	$\boldsymbol{0}$	$-$	$+$	$+$	A_{1g}	$\sin k_z(-\sin 2k_y, \sin 2k_x)$
$\tau_z\rho_x\tilde{\boldsymbol{\sigma}}_{xy}$	$\boldsymbol{Q}$	$-$				A_{2g}	$\sin k_z(\sin 2k_x, \sin 2k_y)$
						B_{1g}	$\sin k_z(\sin 2k_y, \sin 2k_x)$
						B_{2g}	$\sin k_z(\sin 2k_x, -\sin 2k_y)$
$\tau_z\rho_z\tilde{\boldsymbol{\sigma}}_{xy}$	0	$\boldsymbol{0}$	$-$	$+$	$-$	A_{1g}	$\sin k_z(-\sin k_y, \sin k_x)$
$\rho_y\tilde{\boldsymbol{\sigma}}_{xy}$	0	$\boldsymbol{Q}$	$+$			A_{2g}	$\sin k_z(\sin k_x, \sin k_y)$
$\tau_x\rho_y i\sigma_y\tilde{\boldsymbol{\sigma}}_{xy}$	$2e$	$\boldsymbol{Q}$	$+$			B_{1g}	$\sin k_z(\sin k_y, \sin k_x)$
$\tau_y\rho_y i\sigma_y\tilde{\boldsymbol{\sigma}}_{xy}$	$2e$	$\boldsymbol{Q}$	$-$			B_{2g}	$\sin k_z(\sin k_x, -\sin k_y)$
$\tilde{\boldsymbol{\sigma}}_{xy}$	0	$\boldsymbol{0}$	$+$	$-$	$+$	A_{1u}	$(\sin 2k_x, \sin 2k_y)$
$\rho_x\tilde{\boldsymbol{\sigma}}_{xy}$	0	$\boldsymbol{Q}$	$+$			A_{2u}	$(-\sin 2k_y, \sin 2k_x)$
$\tau_x i\sigma_y\tilde{\boldsymbol{\sigma}}_{xy}$	$2e$	$\boldsymbol{0}$	$+$			B_{1u}	$(\sin 2k_x, -\sin 2k_y)$
$\tau_y i\sigma_y\tilde{\boldsymbol{\sigma}}_{xy}$	$2e$	$\boldsymbol{0}$	$-$			B_{2u}	$(\sin 2k_y, \sin 2k_x)$
$\tau_x\rho_x i\sigma_y\tilde{\boldsymbol{\sigma}}_{xy}$	$2e$	$\boldsymbol{Q}$	$+$				
$\tau_y\rho_x i\sigma_y\tilde{\boldsymbol{\sigma}}_{xy}$	$2e$	$\boldsymbol{Q}$	$-$				
$\rho_z\tilde{\boldsymbol{\sigma}}_{xy}$	0	$\boldsymbol{0}$	$+$	$-$	$-$	A_{1u}	$(\sin k_x, \sin k_y)$
$\tau_z\rho_y\tilde{\boldsymbol{\sigma}}_{xy}$	0	$\boldsymbol{Q}$	$-$			A_{2u}	$(-\sin k_y, \sin k_x)$
$\tau_x\rho_z i\sigma_y\tilde{\boldsymbol{\sigma}}_{xy}$	$2e$	$\boldsymbol{0}$	$+$			B_{1u}	$(\sin k_x, -\sin k_y)$
$\tau_y\rho_z i\sigma_y\tilde{\boldsymbol{\sigma}}_{xy}$	$2e$	$\boldsymbol{0}$	$-$			B_{2u}	$(\sin k_y, \sin k_x)$

Bibliography

[1] A. Altland and M. R. Zirnbauer. “Nonstandard symmetry classes in mesoscopic normal-superconducting hybrid structures”. *Physical Review B* **55** (1997), 1142–1161.

[2] M. Z. Hasan and C. L. Kane. “Colloquium: Topological insulators”. *Reviews of Modern Physics* **82** (2010), 3045–3067.

[3] X.-L. Qi and S.-C. Zhang. “Topological insulators and superconductors”. *Reviews of Modern Physics* **83** (2011), 1057–1110.

[4] B. A. Bernevig, T. L. Hughes, and S.-C. Zhang. “Quantum Spin Hall Effect and Topological Phase Transition in HgTe Quantum Wells”. *Science* **314** (2006), 1757–1761.

[5] B. A. Bernevig and S.-C. Zhang. “Quantum Spin Hall Effect”. *Physical Review Letters* **96** (2006), 106802.

[6] G. Grüner. “The dynamics of charge-density waves”. *Reviews of Modern Physics* **60** (1988), 1129–1181.

[7] K. Klitzing, G. Dorda, and M. Pepper. “New Method for High-Accuracy Determination of the Fine-Structure Constant Based on Quantized Hall Resistance”. *Physical Review Letters* **45** (1980), 494–497.

[8] D. Thouless et al. “Quantized Hall Conductance in a Two-Dimensional Periodic Potential”. *Physical Review Letters* **49** (1982), 405–408.

[9] M. Kohmoto. “Topological invariant and the quantization of the Hall conductance”. *Annals of Physics* **160** (1985), 343–354.

[10] M. V. Berry. “Quantal Phase Factors Accompanying Adiabatic Changes”. English. *Proceedings of the Royal Society of London. Series A, Mathematical and Physical Sciences* **392** (1984), pp. 45–57.

[11] X. Qi et al. “Topological Superconductivity and Superfluidity”. *Physical Review Letters* **102** (2009), 187001.

[12] C. L. Kane and E. J. Mele. “$\mathbb{Z}_2$ Topological Order and the Quantum Spin Hall Effect”. *Physical Review Letters* **95** (2005), 146802.

[13] C. L. Kane and E. J. Mele. “Quantum Spin Hall Effect in Graphene”. *Physical Review Letters* **95** (2005), 226801.

[14] M. Konig et al. “Quantum Spin Hall Insulator State in HgTe Quantum Wells”. *Science* **318** (2007), 766–770.

[15] A. Y. Kitaev. “Unpaired Majorana fermions in quantum wires”. *Physics-Uspekhi* **44** (2001), 131–136.

[16] J. Alicea et al. “Non-Abelian statistics and topological quantum information processing in 1D wire networks”. *Nature Physics* **7** (2011), 412–417.

[17] E. P. Wigner and P. A. M. Dirac. “On the statistical distribution of the widths and spacings of nuclear resonance levels”. *Mathematical Proceedings of the Cambridge Philosophical Society* **47** (1951), 790.

[18] F. J. Dyson. “Statistical Theory of the Energy Levels of Complex Systems. I”. *Journal of Mathematical Physics* **3** (1962), 140.

[19] P. Kotetes. “Classification of engineered topological superconductors”. 2013.

[20] A. Kitaev. “Periodic table for topological insulators and superconductors”. *ArXiv e-prints* (2009).

[21] A. Hatcher. *Algebraic Topology*. Vol. 227. Cambridge University Press, 2002.

[22] A. Schnyder et al. “Classification of topological insulators and superconductors in three spatial dimensions”. *Physical Review B* **78** (2008), 195125.

[23] S. Ryu et al. “Topological insulators and superconductors: tenfold way and dimensional hierarchy”. *New Journal of Physics* **12** (2010), 065010.

[24] R. Markiewicz and M. Vaughn. “Classification of the Van Hove scenario as an SO(8) spectrum-generating algebra”. *Physical Review B* **57** (1998), R14052–R14055.

[25] S. Lidin. “The Discovery of Quasicrystals”. *The Nobel Prize in Chemistry 2011 - Press Release* (2011).

[26] R. Penrose. “Role of aesthetics in pure and applied research” Bulletin of the Institute of Mathematics and Its Applications”. *Bulletin of the Institute of Mathematics and Its Applications* **10** (1974), 266.

[27] N. G. de Bruijn. “Algebraic theory of Penrose’s non-periodic tilings of the plane, I, II”. *Indagationes mathematicae* **43(1)** (1981), 39–66.

[28] E. Wigner. *Gruppentheorie und ihre Anwendung auf die Quantenmechanik der Atomspektren*. Die Wissenschaft. Vieweg, 1931.

[29] F. Cotton. *Chemical applications of group theory*. A Wiley interscience publication. Wiley, 1990.

[30] M. Sigrist and K. Ueda. “Phenomenological theory of unconventional superconductivity”. *Reviews of Modern Physics* **63** (1991), 239–311.

[31] G. Grüner. “The dynamics of spin-density waves”. *Reviews of Modern Physics* **66** (1994), 1–24.

[32] S. Tewari et al. “Time-Reversal Symmetry Breaking by a (d+id) Density-Wave State in Underdoped Cuprate Superconductors”. *Physical Review Letters* **100** (2008), 217004.

[33] P. Kotetes and G. Varelogiannis. “Meissner effect without superconductivity from a chiral d-density wave”. *Physical Review B* **78** (2008), 220509.

[34] C. Zhang et al. “Anomalous Nernst effect from a chiral d-density-wave state in underdoped cuprate superconductors”. *Physical Review B* **78** (2008), 174508.

[35] P. Kotetes and G. Varelogiannis. “Chirality Induced Tilted-Hill Giant Nernst Signal”. *Physical Review Letters* **104** (2010), 106404.

[36] C.-H. Hsu, S. Raghu, and S. Chakravarty. “Topological density wave states of nonzero angular momentum”. *Physical Review B* **84** (2011), 155111.

[37] Y. L. Chen et al. “Experimental Realization of a Three-Dimensional Topological Insulator, Bi_2Te_3 ”. *Science* **325** (2009), 178–181.

[38] J. Moore. “Topological insulators: The next generation”. *Nature Physics* **5** (2009), 378–380.

[39] S. Dresselhaus, G. Dresselhaus, and A. Jorio. “Group Theory: Application to the Physics of Condensed Matter” (2008).

[40] L. Fu. “Hexagonal Warping Effects in the Surface States of the Topological Insulator Bi_2Te_3 ”. *Physical Review Letters* **103** (2009), 266801.

[41] S. Basak et al. “Spin texture on the warped Dirac-cone surface states in topological insulators”. *Physical Review B* **84** (2011), 121401.

[42] L. Fu and C. Kane. “Superconducting Proximity Effect and Majorana Fermions at the Surface of a Topological Insulator”. *Physical Review Letters* **100** (2008), 096407.

[43] H. Zhang et al. “Topological insulators in Bi_2Se_3, Bi_2Te_3 and Sb_2Te_3 with a single Dirac cone on the surface”. *Nature Physics* **5** (2009), 438–442.

[44] Y. Baum and A. Stern. “Density-waves instability and a skyrmion lattice on the surface of strong topological insulators”. *Physical Review B* **86** (2012), 195116.